A Global Hybrid Tropical Cyclone Risk Model based upon Statistical and Coupled Climate Models

David A. Carozza[1], Mathieu Boudreault[1], Manuel Grenier[2], and Louis-Philippe Caron[3]

[1]Université du Québec à Montréal
[2]The Co-operators General Insurance Company
[3]Ouranos, Canada

May 25, 2023

Abstract

Tropical cyclones (TCs) are among the most destructive natural hazards and yet, quantifying their financial impacts remains a significant methodological challenge. It is therefore of high societal value to synthetically simulate TC tracks and winds to assess potential impacts along with their probability distributions for e.g., land use planning and financial risk management. A common approach to generate TC tracks is to apply storm detection methodologies to climate model output, but such an approach is sensitive to the method and parameterization used and tends to underestimate intense TCs. We present a global TC model that melds statistical modeling, to capture historical risk features, with a climate model large ensemble, to generate large samples of physically-coherent TC seasons. Integrating statistical and physical methods, the model is probabilistic and consistent with the physics of how TCs develop. The model includes frequency and location of cyclogenesis, full trajectories with maximum sustained winds and the entire wind structure along each track for the six typical cyclogenesis basins from IBTrACS. Being an important driver of TCs globally, we also integrate ENSO effects in key components of the model. The global TC model thus belongs to a recent strand of literature that combines probabilistic and physical approaches to TC track generation. As an application of the model, we show global risk maps for direct and indirect hits expressed in terms of return periods. The global TC model can be of interest to climate and environmental scientists, economists and financial risk managers.

A Global Hybrid Tropical Cyclone Risk Model based upon Statistical and Coupled Climate Models

David A. Carozza[1], Mathieu Boudreault[1], Manuel Grenier[1,2], Louis-Philippe Caron[3]

[1]Department of Mathematics, Université du Québec à Montréal, Montréal, QC, Canada
[2]Climatic Hazards and Advanced Risk Modelling, The Co-operators General Insurance Company, Québec, QC, Canada
[3]Ouranos, Montréal, Canada

Key Points:

- We present a global tropical cyclone (TC) risk model built upon a climate model large ensemble that can be used for risk analysis.
- We integrate ENSO into our model since it is a strong driver of storm annual frequency, cyclogenesis, trajectories, and intensity.
- We present global risk maps consistent with statistical features of TC components and coherent with a global climate model.

Corresponding author: Mathieu Boudreault, `boudreault.mathieu@uqam.ca`

Abstract

Tropical cyclones (TCs) are among the most destructive natural hazards and yet, quantifying their financial impacts remains a significant methodological challenge. It is therefore of high societal value to synthetically simulate TC tracks and winds to assess potential impacts along with their probability distributions for e.g., land use planning and financial risk management. A common approach to generate TC tracks is to apply storm detection methodologies to climate model output, but such an approach is sensitive to the method and parameterization used and tends to underestimate intense TCs. We present a global TC model that melds statistical modeling, to capture historical risk features, with a climate model large ensemble, to generate large samples of physically-coherent TC seasons. Integrating statistical and physical methods, the model is probabilistic and consistent with the physics of how TCs develop. The model includes frequency and location of cyclogenesis, full trajectories with maximum sustained winds and the entire wind structure along each track for the six typical cyclogenesis basins from IBTrACS. Being an important driver of TCs globally, we also integrate ENSO effects in key components of the model. The global TC model thus belongs to a recent strand of literature that combines probabilistic and physical approaches to TC track generation. As an application of the model, we show global risk maps for direct and indirect hits expressed in terms of return periods. The global TC model can be of interest to climate and environmental scientists, economists and financial risk managers.

Plain Language Summary

Tropical cyclones (TCs) are among the most destructive natural hazards and yet, quantifying their financial impacts remains a difficult task. Being able to randomly simulate TCs and their features (such as wind speed) with mathematical models is therefore critical to build scenarios (and their corresponding probability) for land use planning and financial risk management. A common approach is to simulate TCs by tracking them directly in climate model outputs but this often underestimates the frequency of intense TCs while being computationally costly overall to generate a large number of events. For these reasons, many authors have looked into alternative approaches that replicate key physical features of TCs but rather using statistical models that are much less computationally demanding. This paper therefore presents a global TC model that leverages the strengths of both statistical and climate models to simulate a large number of TCs whose features are consistent with the physics and observations. As an important global phenomenon that affects TCs globally, we also integrate in our model the effects of El Niño. The paper focuses on the methodology and validation of each model component and concludes with global risk maps for direct and indirect hits.

1 Introduction

Tropical cyclones (TCs) consistently rank as one of the most significant climate extremes (Easterling et al., 2000), both in terms of casualties and economic losses (CRED, 2021; UNDRR, 2020). Coastal communities, local and regional stakeholders, and the insurance and reinsurance industry have first-hand experience of the adverse effects of tropical cyclones. However, modelling the impacts of TCs remains an important challenge for risk management (UNEP, 2019; Fiedler et al., 2021). Natural patterns of interannual climate variability, such as the El Niño-Southern Oscillation (ENSO), modulate TC features such as annual frequency, cyclogenesis, intensity, and duration over basins worldwide (Lin et al., 2020). The short observational records, the rarity of storms, and significant global variability in vulnerability and exposure contribute to large and complex uncertainties in global risk analyses. Moreover, climate change has the potential to perturb atmospheric and oceanic features that drive tropical cyclone activity (Knutson et al., 2020). In fact, a consensus is growing towards an increased likelihood of more intense and rainy storms, as well as an increased risk of flooding due to sea level rise (Seneviratne et al., 2021).

Climate impacts are commonly studied through the lens of general circulation models (GCMs) (Warszawski et al., 2013). However, when using climate model output, the frequency of tropical storms is sensitive to the method used to detect storm tracks (Roberts et al., 2020), and intensities are typically weaker than observed, with very intense storms being difficult to reproduce (Knutson et al., 2020). Although these issues improve with increasing model resolution (Caron et al., 2011; Strachan et al., 2013; Kreussler et al., 2021), climate models still have biases in their cyclogenesis locations, which, when combined with biases in the steering flows, make it difficult to reproduce observed landfalling statistics and thus render them unsuitable for risk modeling (Roberts et al., 2020). As such, purely physical approaches are not currently used in risk modeling applications, which require an accurate representation of observed tropical cyclone risk, and the ability to replicate the impact of extreme events, the latter necessitating a large number of simulations.

Risk modeling of tropical cyclone activity strives to provide an accurate representation of the potential damage associated with TCs over a given period of time. This can range from one year for underwriting in the (re)insurance industry, to years and decades for land use planning, and strategic policy- and decision-making. To maintain fidelity to historical observations, in particular for challenging features such as extreme winds and landfall rates, statistical models of storm frequency, cyclogenesis location, trajectory, intensity (maximum sustained winds and/or pressure), and size, are typically combined to represent the risk-driving components (Lee et al., 2018; Bloemendaal et al., 2020). This approach expands upon the historical record by generating a large number of tropical cyclone events over multiple years. Beginning with Vickery et al. (2000), studies have included environmental information from observational or reanalysis products as predictor variables to better represent the spatiotemporal variability of tropical cyclone components. Atmospheric reanalysis products in particular are increasingly used to build statistical and prognostic models (Emanuel, 2017; Lee et al., 2018; Bloemendaal et al., 2020).

TC risk models have long been developed by the catastrophe modelling industry, but a few of these models have appeared recently in the scientific literature. An ambitious intercomparison project of such TC models has emerged lately in Meiler et al. (2022). The authors analyzed the MIT (Emanuel et al., 2006, 2008), CHAZ (Lee et al., 2018), and STORM (Bloemendaal et al., 2020) models coupled with CLIMADA (Aznar-Siguan & Bresch, 2019) with the goal to simulate and compare economic damage due to winds under the present climate. The intercomparison found large variability between the participating models, and highlighted differences of approximately an order of magnitude in dollar-value impacts for low probability storms (1 in 10 years and rarer) and storms in basins with low annual frequency. We can also find applications of MIT, CHAZ and STORM models with CMIP5/6 climate models under both present and future climates in Emanuel (2013); Lee et al. (2020); Bloemendaal et al. (2022).

Here, we present a global TC wind risk model with statistical-dynamical components that is used in conjunction with a climate model large ensemble to generate large samples of TC seasons. Built using both statistical and physical methods, the model is probabilistic, consistent with the physics of tropical cyclones, and therefore highly flexible in nature. ENSO, which has a strong influence on TC activity in multiple basins, is used to define several model components and link statistical approaches to the environmental variables provided by a climate model (Bell et al., 2014). We connect the statistical and climate-driven aspects of our model by building statistically-generated trajectories and then calculating the intensity by means of Emanuel (2017). This approach couples TC model behaviour to the climate model's environment, while remaining faithful to the features of observed tracks. We also apply a post-processing methodology to

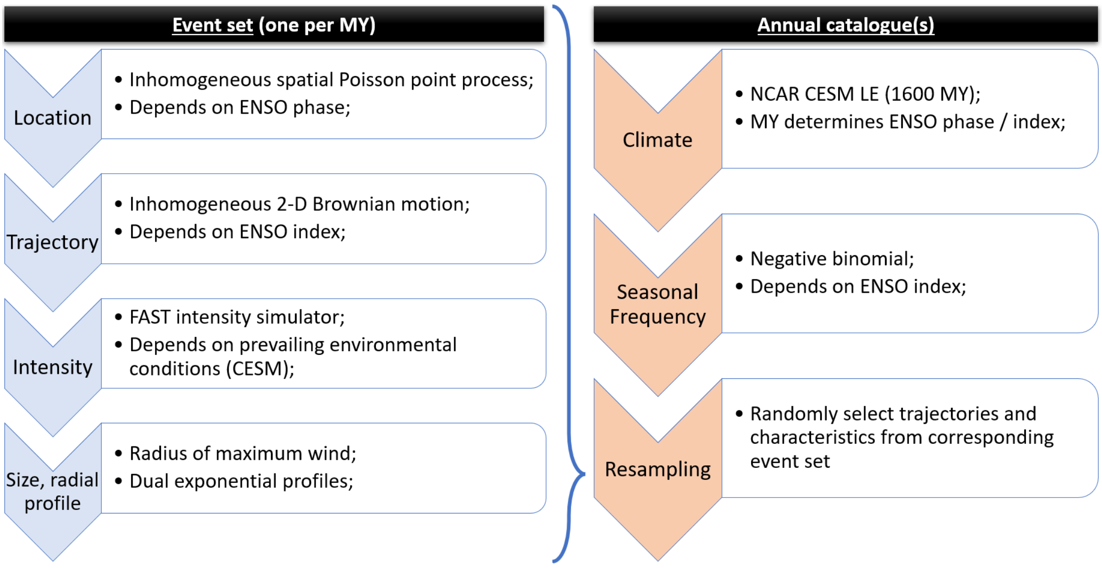

Figure 1: Global tropical cyclone model schematic detailing the components of the (1) the event set generation (left-hand side) and (2) the catalog generation (right-hand side).

the resulting storm intensity values to correct biases induced by the climate model. Finally, we calibrate the Willoughby et al. (2006) wind structure model for each cyclogenesis basin, thus providing a complete tropical cyclone wind model consistent with the present climate.

The output from our TC model consists of two components: 1) the event sets, and 2) the annual catalogs. Each event set is a fixed set of trajectories, with one set for every member and year of the climate model large ensemble. Annual catalogs are obtained by randomly sampling the trajectories from the event sets in accordance with the annual frequency of TCs in any given basin. Our overall model is in line with those analysed in Meiler et al. (2022) (MIT, CHAZ and STORM) and we will therefore borrow their nomenclature to compare each of our model's components with the latter. The model components and key steps are summarized in Figure 1.

The paper is structured as follows. Section 2 describes each model component, including statistical fits and simulations steps, leading to the generation of event sets (as shown on the left-hand side of Figure 1). Section 3 presents the annual frequency component and algorithm to generate annual catalogs (as shown on the right-hand side of Figure 1). We provide results and assess the quality of the global TC model in Section 4. Finally, we present risk maps expressed in terms of return periods in Section 5, and summarize key findings and conclude the paper in Section 6.

2 Event sets

This section focuses on the methodological steps leading to the construction of one event set per member and year (member-year or MY) of the climate model large ensemble. The underlying GCM is first presented in Section 2.1. Then, we present the modelling assumptions and fitting steps for each of the cyclogenesis (Section 2.2), trajectory (Section 2.3), intensity (Section 2.4), and size and radial profile (Section 2.5) components. We conclude this section with the simulation algorithm (Section 2.6) and the post-processing steps (Section 2.7) that reduce biases in the event sets. Whereas this section solely focuses on model features, calibration and simulation, we present in Section 4 model validation and evaluation results for the components or combination thereof.

2.1 Climate forcing

The global TC model is forced by the climate model output from the NCAR Community Earth System Model Large Ensemble (NCAR CESM-LE) (Kay et al., 2015) (K2015 from here on). As such, for a given MY (1600 or 40 members of 40 years in total taking model years between 1981 and 2020), we use the simulated atmospheric conditions to generate a specific event set and annual catalog over each basin. The climate model output therefore influences cyclogenesis location (through the corresponding ENSO phase), the trajectory (using the corresponding ENSO index) and wind speed (using the output of the CESM to feed the FAST model from Emanuel (2017), see Section 2.4). As a result, we are not trying to detect tropical cyclones from a GCM but are instead using the output from the NCAR CESM-LE to identify environments favorable to TC development and simulate how a TC would evolve and propagate in this environment.

This approach of forcing a climate model into a set of statistical models is similar to the original CHAZ model (Lee et al., 2018) which was forced with the ERA5 reanalysis, and Lee et al. (2020) which used CMIP5 models. The methodology is however significantly different from the STORM model which is fully stochastic and has no explicit forcing from climate models, and from the MIT model which is mostly physically driven.

2.2 Cyclogenesis location

Cyclogenesis location is defined as the first point of each trajectory as provided in the IBTrACS 4.0 database (Knapp et al., 2010, 2018). We consider all trajectories from the 1981 season to the present (IBTrACS dataset accessed June 27, 2021) with a lifetime maximum intensity (LMI) of at least tropical storm intensity (18 ms^{-1}). We follow the basin definitions from IBTrACS; that is, we analyze cyclogenesis locations for the North Atlantic (NA), Eastern North Pacific (EP, which includes the Central Pacific region), Western North Pacific (WP), North Indian (NI), South Pacific (SP) and South Indian (SI). The South Atlantic (SA) basin is therefore excluded.

We assume cyclogenesis is influenced by ENSO and use the ENSO phase (El Niño, Neutral and La Niña) as a driver of cyclogenesis location. We employ the Japan Meteorological Agency Sea Surface Temperature Anomaly index (ENSO JMA SSTA) because it performs well in selecting known ENSO phases. The index is defined in terms of the monthly average sea surface temperature anomaly over the Niño 3 region (4°N to 4°S, 150°W to 90°W). The anomaly index must be more (less) than 0.5°C (-0.5°C) over 6 consecutive 5-month periods to identify an El Niño (La Niña) (Bove et al., 1998).

Cyclogenesis locations are modeled using an inhomogeneous spatial Poisson point process. The spatial rate of cyclogenesis events is first calibrated to IBTrACS (longitude and latitude coordinates) for each phase and basin. It is computed as the generation rate of storms over a 2D (latitude-longitude) grid representing the basin, and is smoothed using a Gaussian kernel with a large bandwidth to allow for the potential formation of cyclones in rarer regions (standard deviation used as bandwidth of 5). Figure 2 (in Section 4) shows the generation rate for the North Atlantic and West Pacific for each ENSO phase (a similar plot is provided for each basin in the Supporting Information).

To simulate cyclogenesis locations, we first determine the ENSO phases in the CESM-LE. We follow the methodology of Bove et al. (1998), using sea surface temperature output from the CESM-LE to calculate the monthly ENSO JMA SSTA index and determine the ENSO phase for each MY. We apply the composite approach of Bell et al. (2014), which associates tropical cyclone seasons in the Northern Hemisphere (May-November) to the following ENSO event, and Southern Hemisphere seasons (October-May) to the ongoing ENSO event. Given the ENSO phase, we sample from an inhomogeneous spatial Poisson point process whose generation rate is that which was calibrated empirically.

Cyclogenesis in the original MIT model is based upon a random seeding approach which randomly draws locations in each cyclogenesis basin. To improve acceptance rates of cyclones, the CHAZ model therefore integrates the Tropical Cyclone Genesis Index (TCGI). The STORM cyclogenesis component is entirely empirical, randomly sampling in each grid cell according to observed monthly cyclogenesis rates. Our cyclogenesis component is therefore a hybrid between CHAZ and STORM whose cyclogenesis rate is spatially smoothed based upon observations for each ENSO phase and simulated locations are continuous in space, rather than fixed at the center of grid cells.

2.3 Trajectory

Storm trajectories are defined in terms of their zonal (easterly or westerly) and meridional (northerly or southerly) components for each trajectory segment. The trajectory model is built upon an inhomogeneous two-dimensional (2-D) Brownian motion. This approach generalizes trajectory models based on Markov chains on a 2-D grid (Emanuel et al., 2006; Nederhoff et al., 2021) while providing a stochastic representation of the beta and advection model (MIT, CHAZ). The underlying Brownian motion needs to be inhomogeneous to capture the Coriolis effect and steering winds, while being influenced by ENSO. We therefore model meridional and zonal displacements (or equivalently the angle and speed) of tropical cyclones using correlated normal distributions whose means and standard deviations are different per latitudinal band and ENSO index.

Fitting of the trajectory component is based upon IBTrACS using the same underlying tracks as in Section 2.2. The dataset represents storm movement over time steps of 6 hours. To capture the latitude-dependent structural features of tropical cyclone trajectories, displacements are first divided into latitudinal bands of at least 2 degrees, such that there are at least 30 data points (30 6-hour segments in IBTrACS) in each band. For each latitudinal band, we run linear regression models for both the meridional and zonal displacements whose sole predictor variable is the observed monthly ENSO JMA SSTA index (Bove et al., 1998). Standard deviations and correlations are then obtained from the residuals of the regressions. The overall approach is therefore rooted in James and Mason (2005) and similar to STORM, but instead we use smaller latitudinal bins, integrate ENSO in the regression equations and include correlations in the innovations to replicate the speed and angle structure.

To simulate a full trajectory, we first compute the ENSO index taken from the chosen MY of the NCAR CESM-LE and randomly sample cyclogenesis location knowing the ENSO phase and basin. Based on the corresponding latitudinal band and ENSO index, we sample meridional and zonal displacements from the corresponding bivariate normal distribution. This therefore provides a new location for the storm 6 hours later, and based on the latter, we sample new meridional and zonal displacements, and so on.

2.4 Intensity

The intensity model is based on the FAST (Emanuel, 2017) tropical cyclone wind simulator, which was designed to simulate large samples of tropical cyclone events. The model is defined by a set of 2 coupled nonlinear ordinary differential equations with surface circular wind speed and inner core moisture as prognostic variables. The two equations describe their evolution in terms of ocean interaction, ventilation, dissipative heating, and the pressure dependence of the surface saturation mixing ratio. These processes are not constructed from first principles but founded on empirical developments (Schade & Emanuel, 1999; Emanuel & Zhang, 2017) with the CHIPS ocean-atmosphere tropical cyclone model (Emanuel et al., 2004). FAST runs at speeds comparable to statistical models and has a performance comparable to the CHIPS model (Emanuel, 2017) which was used in the MIT model.

FAST requires potential intensity, vertical wind shear, storm translation speed, mixed layer depth, sub-mixed layer thermal stratification, and ocean bathymetry as input variables to represent tropical cyclone wind speed evolution. The atmospheric and oceanic input quantities determine the surface circular wind speed, whereas the bathymetry is used to represent interaction with the coast and landfall. Here, we use the output from each MY of the NCAR CESM-LE to compute maximum sustained wind speed along each simulated trajectory (the previous two steps). Table 1 shows the NCAR-CESM1 variables from the CESM-LE experiment used to calculate these forcing quantities.

Component	Variable	Reference
Vertical wind shear		
	Zonal wind (U, 250 hPa and 850 hPa)	K2015
	Meridional wind (V, 250 hPa and 850 hPa)	K2015
Potential Intensity		
	Atmospheric temperature (T)	K2015
	Sea surface temperature (T)	K2015
	Specific humidity (Q)	K2015
	Surface pressure (PS)	K2015
Mixed Layer Depth		
	Ocean temperature (TEMP)	K2015
Sub-Mixed Layer Thermal Stratification		
	Ocean temperature (TEMP)	K2015
Bathymetry		
	ETOPO1 Global Relief Model	Amante and Eakins (2009); NGDC (2009)

Table 1: Datasets used for tropical cyclone intensity component.

We follow Bister and Emanuel (2002) to calculate monthly maps of potential intensity. Mixed layer depth is taken to be the depth at which temperature is 1°C less than the sea surface temperature (Wagner, 1996; Kara et al., 2000) and sub-mixed layer thermal stratification is calculated from Emanuel (2015) by taking the vertical temperature gradient between the mixed layer depth and 100 meters below it. We use the ETOPO1 Global Relief Model (Amante & Eakins, 2009; NGDC, 2009) to represent bathymetry on a 1 arc-minute ($\sim$1.8 km) grid. This allows us to model the TC interaction with the coast and landfall at sufficiently high resolution, instead of using the CESM-LE bathymetry which is at a nominal resolution of $\sim$100 km. When the center of a tropical cyclone is located over the ocean based on the ETOPO1 grid but is over land based on the lower-resolution CESM grid, the oceanic CESM quantities (mixed layer depth and sub-mixed layer thermal stratification) are not defined. In this case, we calculate tropical cyclone intensity by using the most recent values of mixed layer depth and sub-mixed layer thermal stratification.

Time series of vertical shear, potential intensity, mixed layer depth, and sub-mixed layer thermal stratification are determined from their monthly grids depending on the location of the center of the storm and the day of year. For vertical shear and potential intensity, we apply a multilinear interpolation in space and time. Mixed layer depth and sub-mixed layer thermal stratification for each point of the storm track take the monthly mean value of the grid point of the storm center, since they change little from day to day

(Emanuel, 2017). For bathymetry, we also apply a multilinear interpolation in space to determine the bathymetry at the storm center.

Storm translation speed is calculated from the displacement components of the simulated trajectory. We follow Demaria and Kaplan (1994) to compute the zonal (U) and meridional (V) components of winds at 850 and 250 hPa and the magnitude of the vertical wind shear.

To run the FAST model, we interpolate linearly from the 6-hour trajectory timestep to the 4-minute timestep required for FAST. Following Emanuel (2017), we add 60% of the simulated translation velocity (from the trajectory component) to the storm-relative maximum intensity to arrive at the ground-relative peak wind speed (Emanuel & Jagger, 2010). The intensity model is applied to every trajectory of the event set based on the prevailing conditions of the corresponding MY. This physics-based component is therefore deterministic in the sense that two identical trajectories will yield identical winds along their tracks, but a slightly different trajectory might be enough to yield different winds.

The models from the intercomparison project of Meiler et al. (2022) each use different approaches to represent TC intensity. The MIT wind model is based upon the aforementioned CHIPS model. The CHAZ TC intensity is built on autoregressive models (Lee et al., 2015, 2016) whose predictors are derived from environmental conditions (including e.g., potential intensity, vertical wind shear, and mid-level relative humidity). In this case, simulated intensity is obtained by forcing the autoregressive models with a reanalysis or climate model. STORM randomly generates pressure change along the track with an autoregressive model similar to James and Mason (2005). Over the ocean, an empirical wind-pressure relationship is used to deduce wind speed, whereas overland, wind decays according to Kaplan and DeMaria (1995). The relationships for the STORM intensity component are fitted with observations (IBTrACS and reanalysis).

2.5 Size and radial profile

Important progress has been made in the state of knowledge of tropical cyclone size on both the empirical (Dean et al., 2009) and theoretical (Chavas & Emanuel, 2014) fronts, but key challenges remain to improve the understanding of its environmental determinants (Kilroy et al., 2016). Considering this, we take an empirical approach to represent tropical cyclone size and radial profiles. Given empirical differences in the distributions of size and radial profile in different basins, such as storms being largest in the West Pacific and smallest in the East Pacific (Chan & Chan, 2015), we recalibrate Willoughby et al. (2006) for each basin using IBTrACS' wind radii data available since approximately 2000.

Willoughby et al. (2006) assume that the log radius of maximum sustained wind ($\log(R_{\max})$ or RMW) is a linear function of maximum sustained winds ($V_{\max}$) and latitude (φ). The latter three variables are directly available in IBTrACS, which allows a linear regression model to be fit in each basin.

The next step is the calibration of the radial profile. Willoughby et al. (2006) showed that for many tropical cyclones, there might be a different rate of decay in the radial profile, especially away from the center. The radial profile component of our global model borrows the dual-exponential functional form from Willoughby et al. (2006) (Eq. 4). But given that IBTrACS only provides wind radii at 34, 50, and 60 kt for the NE, NW, SE, SW quadrants, not all parameters could be calibrated. As such, we fixed $X_1 = 300$ and $X_2 = 30$ and defined A as

$$A = \Phi\left(\beta_0 + \beta_1 V_{\max} + \beta_2 \varphi\right) \tag{1}$$

where Φ is the cumulative normal distribution function (probit function) that transforms an input in $\mathbb{R}$ to a value within $[0, 1]$. Both exponential decaying functions are therefore used and given a weight of A (that cannot be negative or above 1 in our model) that varies according to wind speed and latitude. To find the parameters β_0, β_1 and β_2 we then minimized the squared errors between Eq. 4 of Willoughby et al. (2006) and the IBTrACS profiles. Each observation of the radial profile takes the maximum radius over the four quadrants available. This process is repeated for each basin.

Simulation of the radial wind profile at a given location begins by computing the prediction of $R_{\max}$ from the linear regression using the simulated maximum winds from the intensity component, and latitude from the location of the trajectory. We then sample one normal random variable for the entire track and add noise to $R_{\max}$. This will simulate a radius for an entire track that is consistently above or below the mean, depending on the normal variate. This is done to avoid an accordion effect where the radius constantly increases or decreases around its predicted value over the track. Then, based upon the sampled $R_{\max}$, in addition to maximum winds and latitude, we deduce the entire wind profile from the dual-exponential function.

Modeling of the radial wind profile differs significantly across the models of the intercomparison project. Whereas the entire wind profile is provided by CHIPS in the MIT model, no wind profile is included by default with CHAZ. STORM simulates the RMW by sampling from observations depending on pressure in each of three stages: at genesis, peak intensity and dissipation. To overcome the discrepancies in available wind profiles, Meiler et al. (2022) couple each model with the same parametric wind field model from Holland (2008).

2.6 Algorithm

We now describe how the components are combined to generate event sets for each MY of the CESM-LE (see the left-hand side of Figure 1). When used in conjunction with vulnerability and exposure information, each event set thus forms the basis of event loss tables (ELTs) used in catastrophe modelling (Mitchell-Wallace et al., 2017).

For each basin and each of the 1600 CESM-LE member-years, we use the model to construct a set of accepted tropical cyclone trajectories that are consistent with the environmental conditions of the year in question. We refer to each of these as event sets that are connected by the following components:

1. Climate forcing: Based on the environmental conditions in the selected MY and basin, determine the ENSO phase and index;
2. Cyclogenesis location: Based on Step 1, simulate one cyclogenesis location from the ENSO-dependent cyclogenesis generation rate;
3. Trajectory: Based on Step 1 and the simulated cyclogenesis location from Step 2, simulate the entire trajectory (meridional and zonal displacements every 6 hours);
4. Intensity: Initialize trajectory intensity at the cyclogenesis location with a wind speed of 10 ms^{-1}, and calculate the intensity every 4 minutes using the FAST model over the entire trajectory with the climate model variables for the MY in question (Step 1). Add 60% of the translation velocity to the intensity to calculate the ground-relative intensity from the storm-relative intensity (Emanuel & Jagger, 2010);
5. Acceptance/Rejection: Retain trajectory if the lifetime maximum intensity (LMI) is 18 ms^{-1} or larger. End trajectory where the storm intensity falls below 2.5 ms^{-1}. If the storm is too weak and is therefore rejected, then repeat Steps 2-5;
6. Size and wind profiles: If the trajectory has a LMI above 30 ms^{-1} (Cat1+ storm), simulate the radius of maximum wind and radial profile. We use this threshold since wind damage is generally negligible for storm with intensity below 30 ms^{-1} (Emanuel, 2011).

To yield a sufficient number of tracks in each event set for the annual catalogs of Section 3, we want for the typical event set to contain as many trajectories as were observed from 1981 to 2020. The number of accepted tracks in each event set is random, and depends on the number of cyclogenesis locations simulated (which is random and simulated from the cyclogenesis density per ENSO phase), the trajectory paths (which are random but depend on the ENSO index), and on the favorability of the environmental conditions over the trajectories (which depend on the MY of the CESM-LE). Although the number of tracks is random for a given cyclogenesis density, we can increase or decrease the number of accepted tracks and preserve the spatial structure of the cyclogenesis densities by applying a constant multiplier. We determine the baseline number of accepted tracks, using the empirical cyclogenesis densities described in Section 2.2 with a sample of 50 event sets. Using such a multiplier, we can adjust the number of accepted tracks over all the event sets to be consistent with the number of observed tracks. For the North Atlantic basin, for example, we run the steps described above for 50 ensemble members and generate 50 event sets, and find that the mean number of accepted trajectories is 315. To therefore arrive at a mean number of tracks that is consistent with the 475 observed tracks over 1981-2020, we multiply the North Atlantic cyclogenesis densities by 1.5. With this adjusted cyclogenesis density, we find that the mean number of tracks over all of the event sets is 500.

2.7 Post-processing

Once we simulate full tracks for each of the 1600 MY, we observe that the global TC model tends to either underestimate or overestimate the relative proportions of stronger or weaker storms (e.g., proportion of Cat4-5 vs Cat1-3 storms when compared to observations over 1981-2020 in Figure 9). Section 4.5 provides a detailed account of these biases. Such biases are to be expected because the FAST intensity model is physically-based and of general applicability, but was forced and validated with output from the NCEP/NCAR Reanalysis (Kalnay et al., 1996), which by construction represents observed historical weather and climate conditions. The NCAR CESM-LE, on the other hand, is an ensemble of simulations from the NCAR Community Earth System model operating at a nominal resolution of $\sim$100 km. The NCAR CESM-LE, like other climate models, carries inherent biases (Moreno-Chamarro et al., 2022), and some of these biases will impact the downscaled TC activity. We do not expect the intensity biases to originate from the cyclogenesis and trajectory components of the model because they do not rely on output from CESM-LE.

To improve simulated intensities relative to observations, we adjusted the simulated lifetime maximum intensity (LMI) distribution. We suggest scaling simulated tropical cyclone wind speeds such that the quantiles of the simulated LMI distribution (over the 1600 MY) match observed quantiles (from IBTrACS). Such a correction is computed and applied in each basin using both the overall empirical LMI distribution or the empirical LMI distribution per ENSO phase. Throughout the paper, we used both approaches, depending on whether the focus is on the overall TC behavior or that per ENSO phase. A comparison is provided in Section 4.5 (and in Figure 9).

We opted for this uniquely post-processing approach as opposed to applying a bias-correction to the NCAR CESM-LE output (pre-processing) that is used as input. Bias corrections of climate data are widely applied, though have typically been conducted for a single variable and location, and as such are one-dimensional. Our use of the NCAR CESM-LE output, however, is highly multivariate (many climate variables) and multi-dimensional (many grid cells), and one-dimensional bias corrections of each climate variable required would not preserve the spatial and temporal dependence of the variables required.

Multivariate bias correction methods are gaining use, though challenges in applicability remain (François et al., 2020). The comparison of multivariate bias correction approaches by François et al. (2020) found that the methods did not represent temporal properties and performed increasingly poorly for increasingly large spatial domains (due to the higher dimensionality of the problem). Since the relevant spatial domain for representing the development of TC intensity, the basin, is large and high dimensional (i.e., it contains a large number of grid cells), and that the temporal dependence of the forcing climate variables is key to the FAST model, we did not rely on a pre-processing approach.

3 Annual catalogs

Because it provides a fixed number of tracks per MY, the information provided by an event set is rarely enough for socioeconomic studies or for risk management applications. The purpose of the catalog is therefore to provide a plausible representation of a tropical cyclone season for a given year. For each basin, member and year of the NCAR CESM-LE, we simulate the annual frequency of tropical cyclones based upon the conditions that prevail in the climate model output for that year and randomly sample the events from the corresponding event set. Repeating this process a large number of times creates a synthetic TC dataset whose structure replicates that of IBTrACS.

This section focuses on the key methodological aspects of generating annual catalogs as depicted on the right-hand side of Figure 1 whereas Section 4 evaluates and validates the components (or combination thereof) of the global TC model.

3.1 Frequency

The annual frequency represents the number of storms whose LMI reaches at least 18 ms^{-1} in a given year and basin. It is modeled with a negative binomial random variable whose mean depends upon the ENSO index. The negative binomial distribution generalizes the Poisson distribution by allowing overdispersion; that is, the variance of the counts can be larger than its mean. The Poisson distribution is a special case of the negative binomial distribution.

For each basin, we fit a negative binomial regression with the annual JMA SSTA index (JMA$_m$) (Bove et al., 1998) as the single predictor variable. For basins in the Northern and Southern Hemisphere, we take the observed JMA$_m$ to be the August-September-October and January-February-March mean, respectively, since these months cover the seasonal activity peaks (Bell et al., 2014). Although the Southern Hemisphere TC seasons take place from November-April, from here on we use the term annual to describe TC frequency. To simulate the annual frequency, we calculate the JMA$_m$ index from the CESM-LE sea surface temperature, compute the parameters of the negative binomial distribution from the fit, and then sample from the distribution.

Cyclogenesis location and frequency are typically intertwined components in the TC models of the intercomparison project. STORM sequentially samples the number of storms from a Poisson distribution with fixed mean, then simulates the cyclogenesis location of each storm. This differs however from the MIT and CHAZ models that both rely on randomly spatially distributed TC seeds while sampling storms until a desired number is attained. Whereas TC seeds are uniformly sampled in the MIT model which could lead to a small acceptance rate, the CHAZ model relies on the TCGI which improves its rate of acceptance. In the MIT approach, we typically aim to reach a fixed number of storms, which is important for the production of ELTs, but in the CHAZ model, frequency results from the accepted number of storms which is driven by the the TCGI. But as Meiler et al. (2022) remark, post-processing CHAZ's frequency of events is still required. In our paper, we borrow the MIT approach to generate a fixed number of storms in the event set production (left-hand side of Figure 1), whereas we use a typical count distribution to generate consistent seasonal frequency (right-hand side of Figure 1).

3.2 Algorithm

To build an annual catalog, we need to follow these steps. For each MY and basin:

1. Climate forcing: Based upon the environmental conditions observed in the selected MY and basin, determine the ENSO index;
2. (Annual) Frequency: Sample the number N of tropical cyclones that reach at least 18 ms^{-1} from a negative binomial distribution whose mean is based upon the ENSO index observed in Step 1;
3. Resampling: Randomly select N trajectories from the corresponding event set.

Using e.g., $N = 625$ simulations from the negative binomial distribution per MY, we get a combined number of 1 million years of events (625 times 1600) allowing for a better understanding of extremes. One year is made of a random number of tracks with their corresponding characteristics drawn from the event sets. Applying this algorithm thus provides the basis for year loss tables (YLTs) in typical catastrophe models (Mitchell-Wallace et al., 2017).

One can also organize catalogs differently to build synthetic IBTrACS-like datasets of 40 years of length. Indeed, each year from the CESM has 40 different members with 625 replications each and therefore, we get 25,000 synthetic IBTrACS-like (40 members times 625 simulations) datasets consistent with the climate of 1981-2020.

4 Model evaluation and results

In this section, we analyze the various features of the model. The analyses provided cover all six basins but for conciseness we only include the figures for the North Atlantic and West Pacific basins. The Supporting Information, provided as an interactive HTML document, allows the reader to view the same figures for all basins.

4.1 Cyclogenesis Location

Figure 2 shows the probability of cyclogenesis for tropical cyclones (with minimum wind speed of 18 ms^{-1}) by ENSO phase (La Niña on the left, Neutral in the middle, El Niño on the right) over the North Atlantic (top row) and West Pacific basins (bottom row). The shades of color represent the spatial probability density conditional upon having cyclogenesis. The darker the color, the more likely cyclogenesis is to occur at that particular location. The bandwidth chosen in the kernel density smoothing allows cyclogenesis in realistic but unobserved areas.

Based on Figure 2 and the Supporting Information, we find that cyclogenesis is more likely to occur over the East Coast of the US during El Niño, while cyclogenesis stretches westward in the Eastern Pacific and eastward in the West Pacific. Although there are important uncertainties since there are few TCs by ENSO phase in the North Indian basin, we find that cyclogenesis is more likely along the East Coast of India, and that TCs on the West Coast of India are more likely to emerge during El Niño. Cyclogenesis moves away from Australia during El Niño in the South Pacific and South Indian basins. The model therefore simulates cyclogenesis locations in accordance with the colored densities shown in Figure 2. It is important to note however the sample size spans only 40 years (study period over 1981-2020), with a relatively limited number of years in each El Niño or La Niña events.

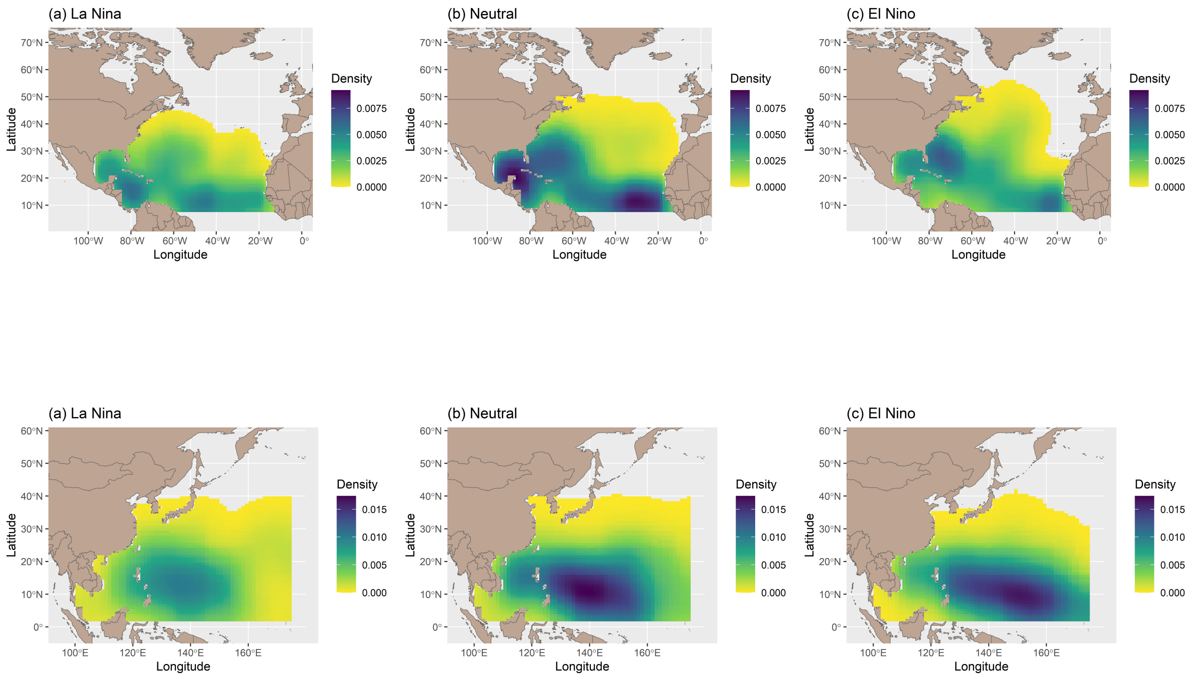

Figure 2: Probability of cyclogenesis in the North Atlantic (top) and West Pacific (bottom) per ENSO phase (Left: La Niña; Center: Neutral; Right: El Niño)

4.2 Trajectory

The zonal and meridional displacements in each latitudinal band are fitted with linear regressions, each with the ENSO index as predictor. The left-hand side of Figure 3 (Figure 4) shows the coefficients of the regressions (y-axis, km per degree C of ENSO anomaly) for each latitudinal band (x-axis, degrees, relative to the Equator) in the North Atlantic (West Pacific) basin for zonal (top row) and meridional (bottom row) displacements. The right-hand side of Figure 3 (Figure 4) shows the p-value of the ENSO predictor for each latitudinal band in the North Atlantic (West Pacific). The red horizontal lines are fixed at 10% (plain red line) and 5% (dotted red line) to determine over which latitudinal band ENSO exerts an influence.

For the North Atlantic, Figure 3 shows that during El Niño (high ENSO index) years there is a negative relationship on meridional displacements north of 23°N, indicating less northerly displacements (Figure 3c). Note that the mean meridional displacement in the North Atlantic is northerly, but during El Niño our fits show that the displacement is less northerly (not southerly) north of 23°N. Between 11 and 19°N, the relationship is instead positive, resulting in more northerly displacements during El Niño. Zonal displacements in most latitudinal bands are not statistically significant (Figure 3b), indicating a weak relationship to the ENSO index.

In the Supporting Information, we show that during El Niño years zonal and meridional displacements are less westerly and more northerly in the East Pacific between approximately 10 and 25°N. In the North Indian basin, El Niño years have less westerly

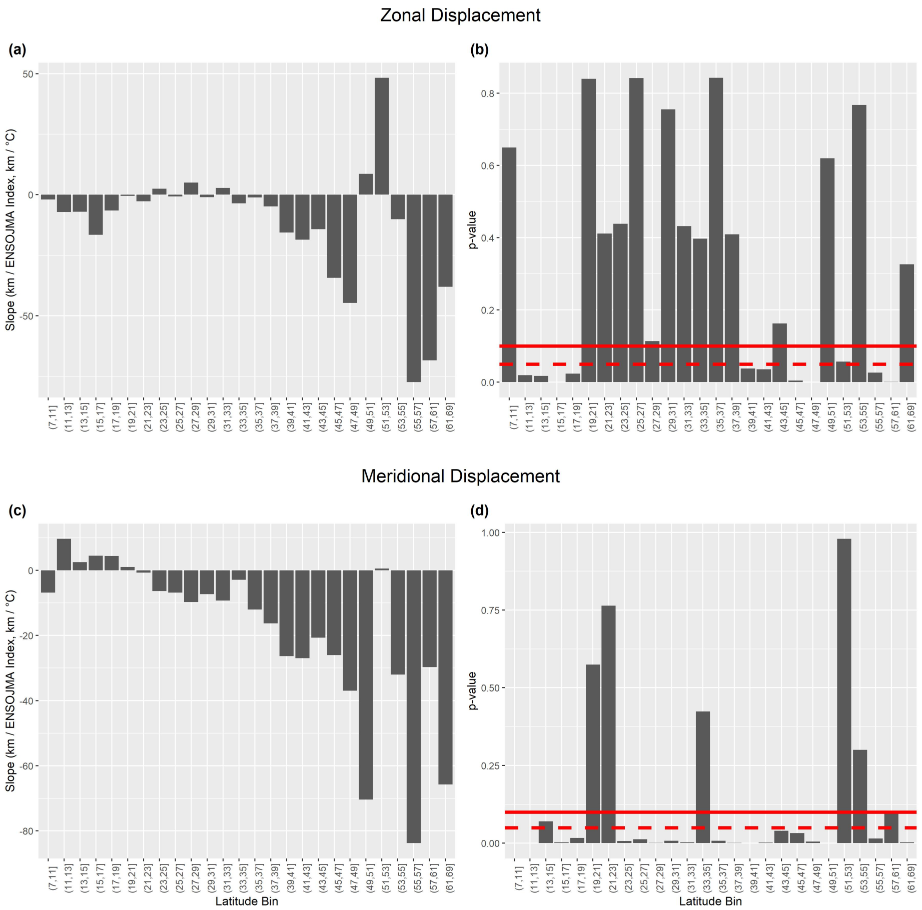

Figure 3: Summary results from statistical fits for zonal and meridional displacements in terms of the ENSO JMA index. Coefficients (left) and statistical significance (right) of the impact of ENSO on zonal (top) and meridional (below) displacements for each latitudinal band in the North Atlantic.

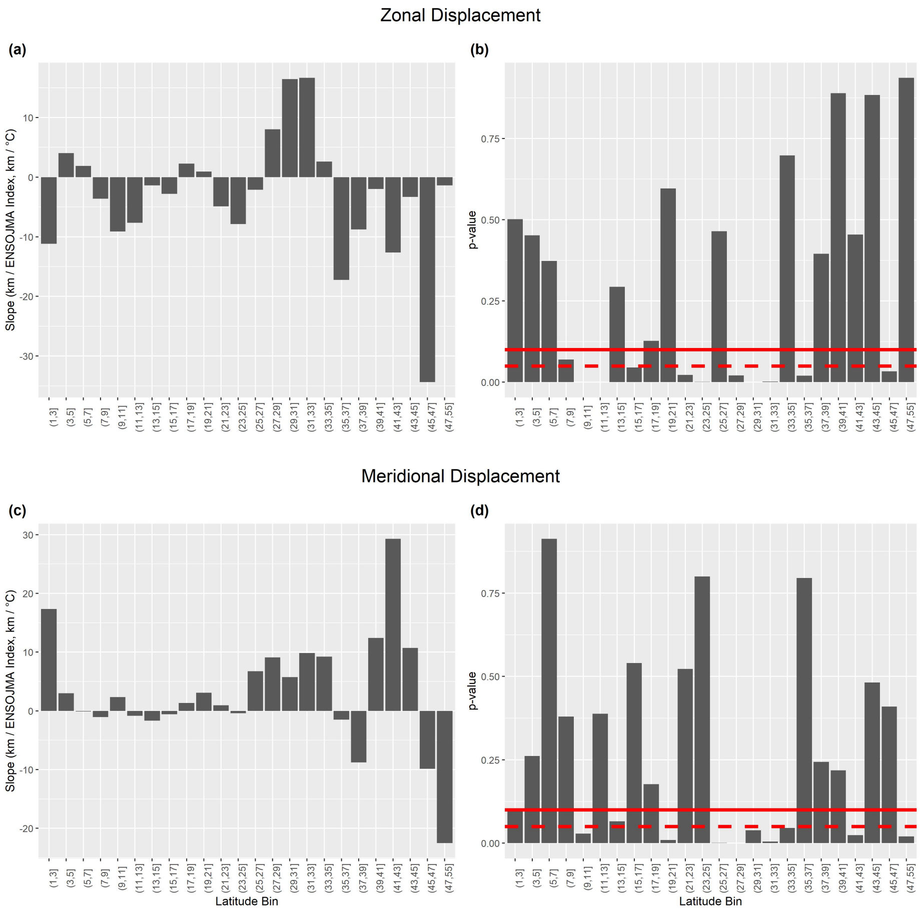

Figure 4: Summary results from statistical fits for zonal and meridional displacements in terms of the ENSO JMA index. Coefficients (left) and statistical significance (right) of the impact of ENSO on zonal (top) and meridional (below) displacements for each latitudinal band in the West Pacific.

displacement in many latitudinal bins, but the relationship between ENSO and meridional displacements appears weak. In the South Indian, there is a strong impact during El Niño rendering zonal displacements less westerly between approximately 10 and 25°S, whereas the link between ENSO and displacements in the South Pacific appears weaker.

4.3 Track densities

We compute the spatial probability density of tropical cyclone tracks, which we refer to as track densities. Such spatial densities allow us to assess the location and intensity of storms in the event sets. It corresponds to the probability that the center of the TC passes over a grid cell, given that the TC has an intensity greater than a pre-specified minimum at that grid cell. Figure 5 shows the observed and simulated track densities for TCs with near-surface winds of least 18 ms^{-1}. The top row shows the track density for model simulations with post-processing based upon the overall distribution of the LMI, the middle row shows the observed track density from IBTrACS, whereas the bottom row shows the simulated bias (red means the model overestimates track density, blue the opposite). The left and right columns display results for the North Atlantic and West Pacific, respectively.

In all basins, the track densities from the model are similar to the observed track densities, thus showing the capability of the model to simulate a realistic tropical cyclone climatology. In the North Atlantic, the model slightly overestimates track density on the East Coast of the U.S. and slightly underestimates track density in the Gulf of Mexico, Caribbean Sea and along the main development region. Over the West Pacific, the model tends to slightly overestimate track density over the Philippines, Brunei and Indonesia, and slightly underestimate track density over Japan and China. Elsewhere, the model underestimates track density on the West Coast of Mexico, on the East Coast of India and Pakistan, over Australia and Papua New Guinea.

We repeated this exercise for Cat4-5 storms in Figure 6. Given the anomalies are small relative to observations (Figure 6, bottom row), the model slightly underestimates observations over the Caribbean Sea, and overestimates observations along the East Coast of the U.S. and the Northern tip of South America. Over the West Pacific, Southern Japan, Coast of China and Northern Philippines, tracks are slightly underestimated whereas they are overestimated over Southern Philippines, Malaysia (Sarawak) and part of Indonesia. Elsewhere, the model underestimates track density on the West Coast of Mexico and overestimates in Central America, underestimates on the East Coast of India and Pakistan, over Australia and Papua New Guinea.

We end this subsection by analyzing and comparing ENSO anomalies in track densities. Figure 7 (Figure 8) shows plots of simulated and observed anomalies for the North Atlantic (West Pacific) basin. For the North Atlantic, we find a clear opposite signal between the tropics and extra-tropics, which is consistent with Goldenberg and Shapiro (1996), and note symmetrical patterns between La Niña and El Niño (particularly in the simulations). There is a positive (negative) anomaly associated with El Niño (La Niña) events along the East Coast of the U.S., and a positive (negative) anomaly associated with La Niña (El Niño) events along the Gulf of Mexico and the Caribbean seas. Although the simulated patterns mostly match observations during La Niña, the observed El Niño anomaly stretches along the East Coast, which is not the case in the simulations. The shape of the observed El Niño anomaly on the right with a red spot over land however suggests the simulations have an adequate behavior but observations may have been influenced by a few outliers.

The simulated positive anomaly over the Caribbean and negative anomaly in the extratropical North Atlantic during La Niña, and negative anomaly over the Caribbean during El Niño, are generally consistent with Baudouin et al. (2018). However, for the extratropics during El Niño, our positive anomaly is more consistent with the Modoki

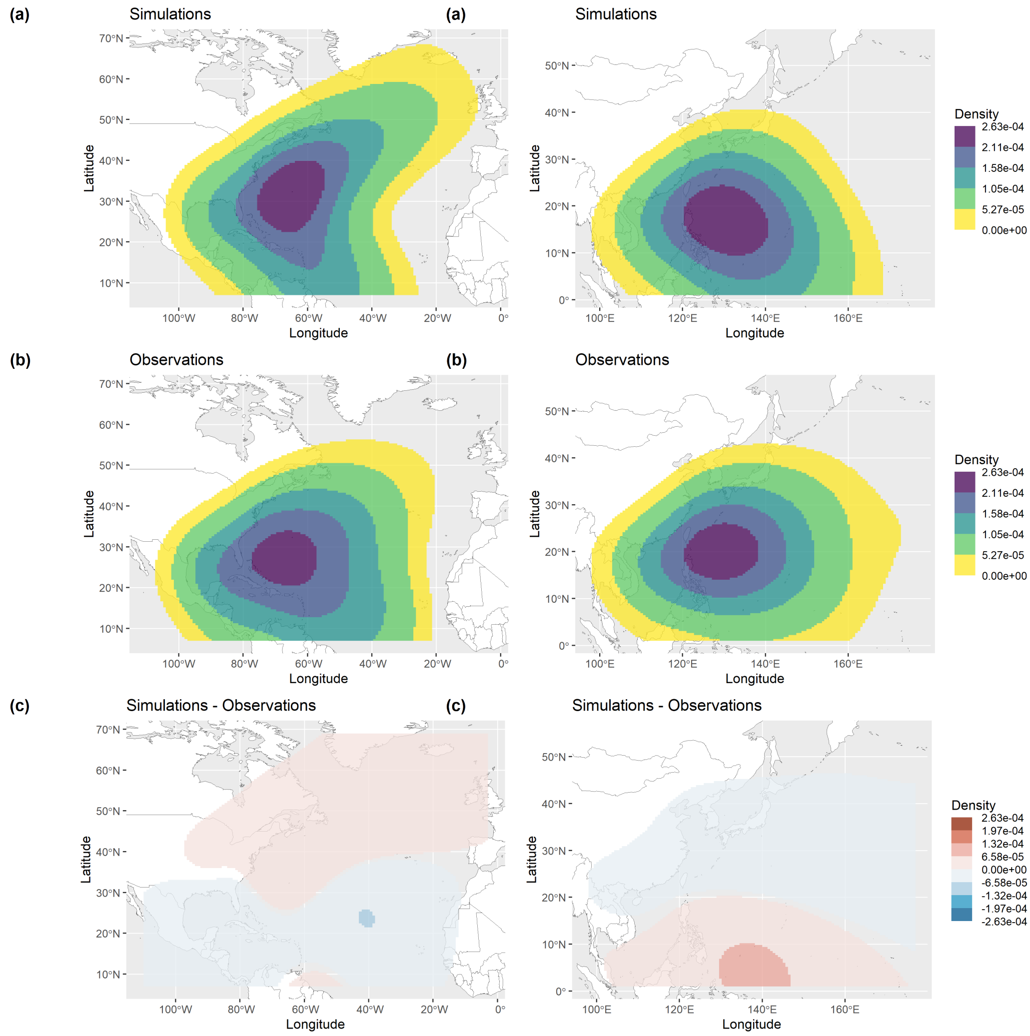

Figure 5: Track probability density over the North Atlantic (left) and West Pacific (right) for storms that reach at least 18 ms^{-1} (Tropical Storms+). Top row (a): simulations from the model; Middle row (b): observations from IBTrACS; Bottom row (c): difference between simulations and observations. The positive and negative limits of the scale for the differences (bottom row) are the same as the maximum limit for the simulations (top row) and observations (middle row). Units are probabilities and add to 1 in the panels in the top two rows.

El Niño (Central Pacific Warming) case from Baudouin et al. (2018). This is reasonable since that study used over two times more tracks from Modoki El Niño years than typical El Niño years.

Over the West Pacific (Figure 8), anomalies highlight an eastward shift during El Niño and westward shift during La Niña. This is well captured by the model. The La Niña signal appears stronger in the observations over South East Asia and the observed anomaly is negative over Japan in both phases. With forty years of data and given the natural variability within each phase, it is likely we observe positive or negative anomalies in both phases in the observations, which is unlikely in the model.

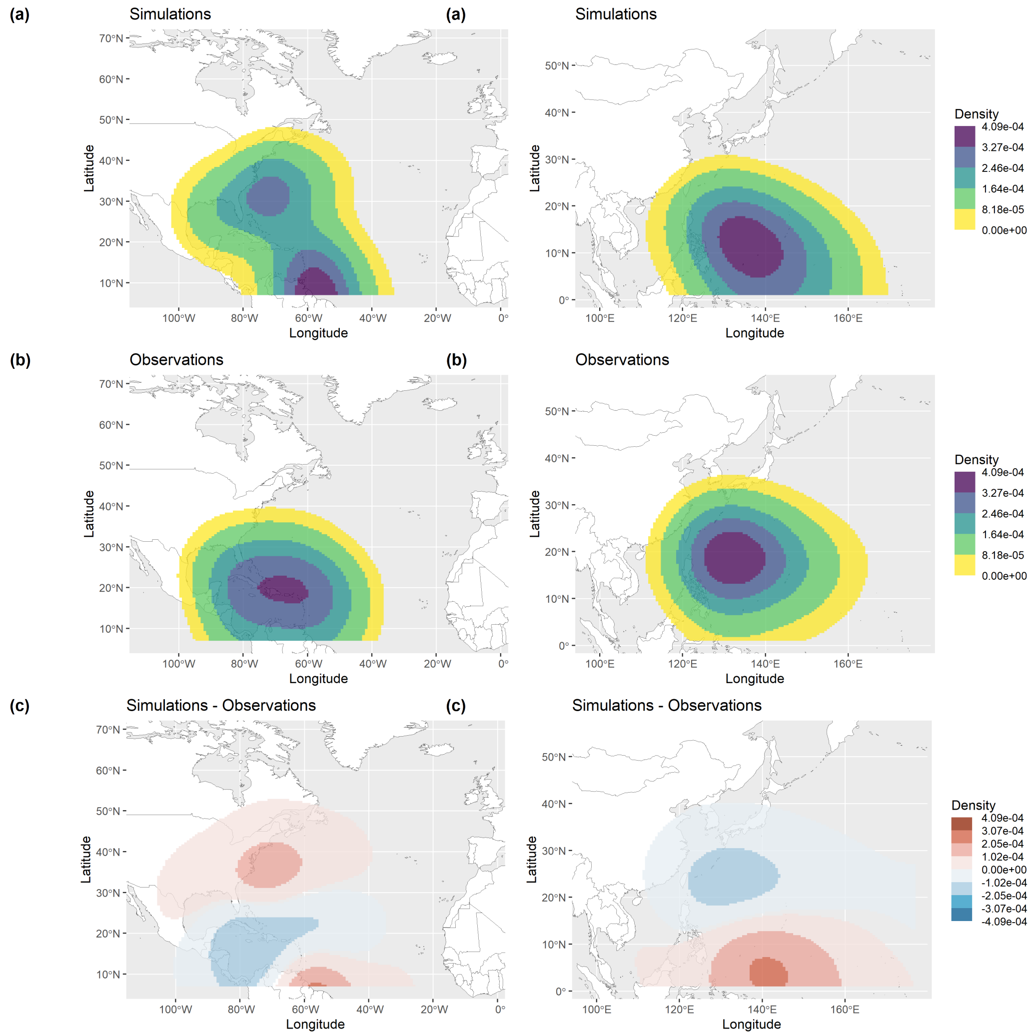

Figure 6: Track probability density over the North Atlantic (left) and West Pacific (right) for storms that reach at least 58 ms^{-1} (Cat4-5). Top row (a): simulations from the model; Middle row (b): observations from IBTrACS; Bottom row (c): difference between simulations and observations. The positive and negative limits of the scale for the differences (bottom row) are the same as the maximum limit for the simulations (top row) and observations (middle row). Units are probabilities and add to 1 in the panels in the top two rows.

Over the other four basins, we also observe approximate symmetrical spatial patterns in the ENSO anomalies. However, we find many areas where observed anomalies are positive (or negative) in both phases that are not replicated in the model: Baja California (Eastern Pacific), Pakistan and parts of India (North Indian), East Coast of Africa (South Indian), North Eastern Australia (South Pacific). The sample of El Niño and La Niña events is relatively small, and so for basins where the ENSO signal is not as dominant, such as the South Indian and East Pacific basins, the signal will be noisy.

Comparing spatial patterns of observed and simulated ENSO anomalies in track densities is a challenging exercise, heavily dependent upon the short observational record and the capacity of the CESM of simulating realistic spatial ENSO patterns. Although not shown, we also analysed the track densities using a post-processing based upon the

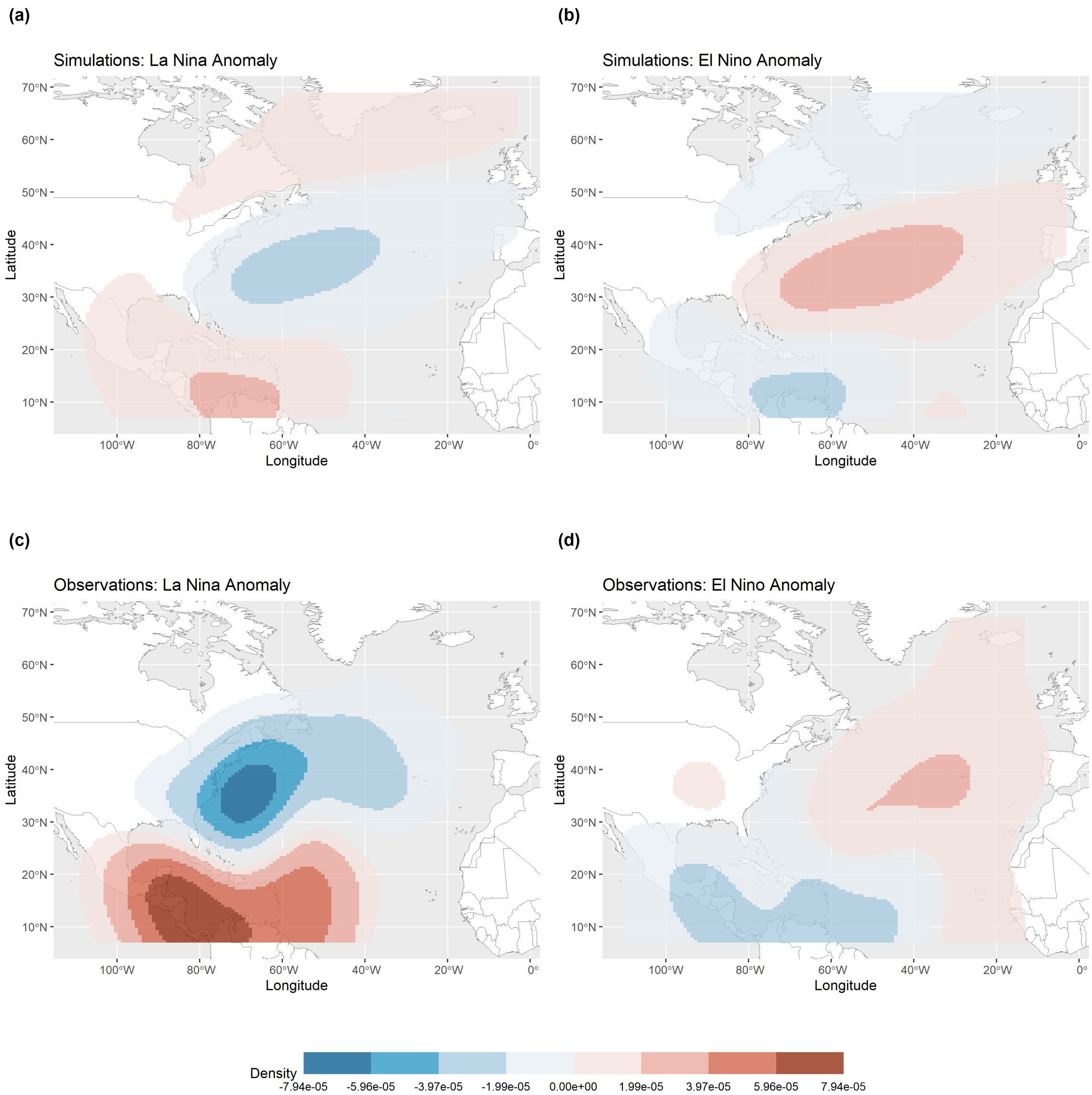

Figure 7: ENSO anomalies in track probability densities for track locations with a minimum speed of 18 ms^{-1} over the North Atlantic.

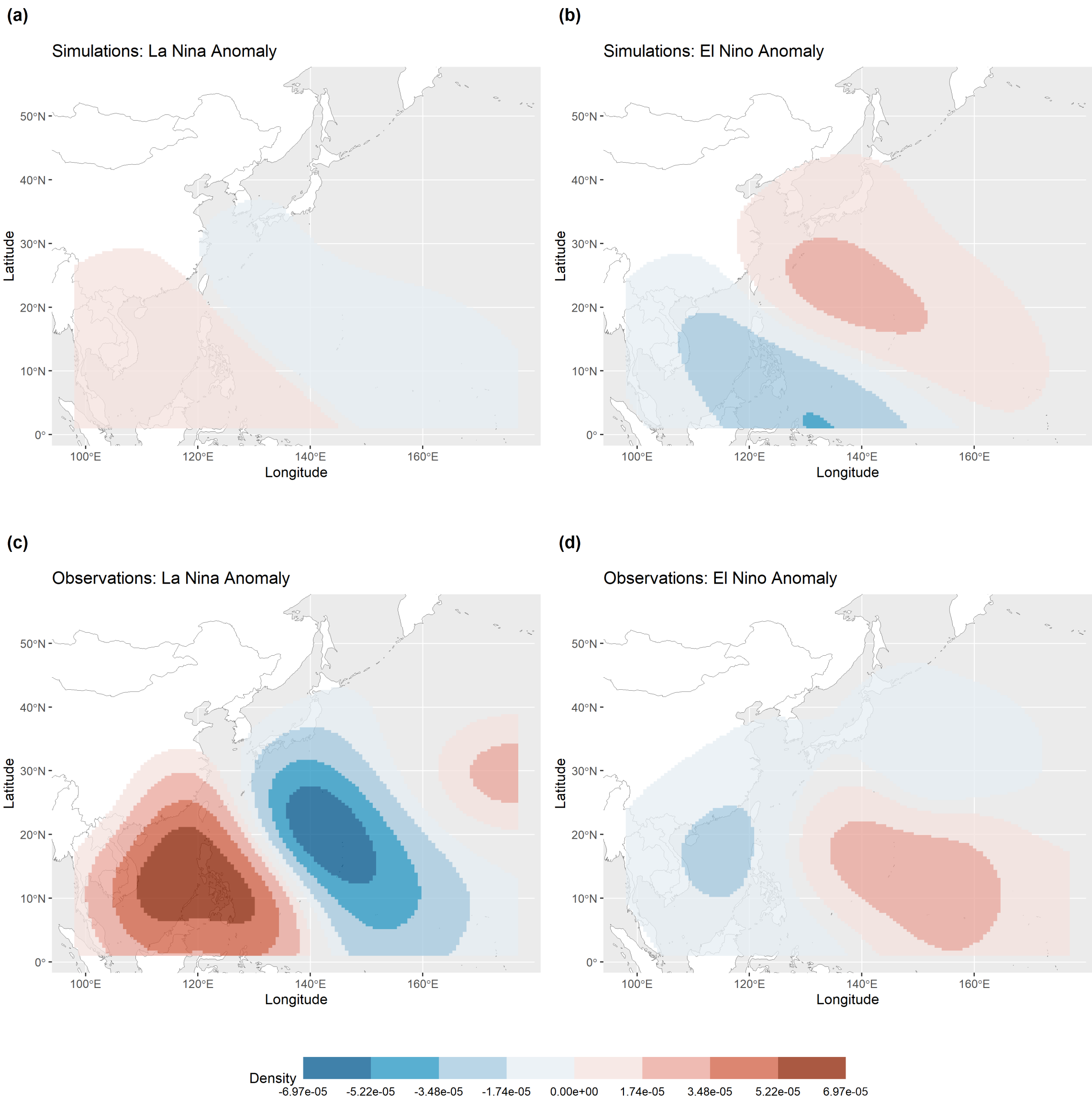

Figure 8: ENSO anomalies in track probability densities for track locations with a minimum speed of 18 ms^{-1} over the West Pacific.

Basin	Intercept	Wind speed	Latitude	sigma
SI	3.9508	-0.0135	-0.0032	0.3739
SP	3.8951	-0.0138	-0.0087	0.3944
WP	3.9155	-0.0118	0.0037	0.4125
NA	3.9358	-0.0154	0.0163	0.5452
EP	3.9731	-0.0133	0.0018	0.4511
NI	4.1406	-0.0148	-0.0077	0.4136

(a) Panel A : Radius of maximum winds

Basin	Intercept	Wind speed	Latitude	RMSE
SI	-1.2014	0.0172	0.0252	8.2167
SP	-1.3312	0.0174	0.0195	8.7479
WP	-1.1821	0.0139	-0.0143	8.7047
NA	-1.1766	0.0161	-0.0221	8.3480
EP	-0.9365	0.0180	-0.0325	8.6994
NI	-1.3083	0.0164	-0.0139	7.8734

(b) Panel B : Dual-exponential profile

Table 2: Parameter estimates of the Willoughby model in each basin. Panel A: RMW regression model. The columns Intercept, Wind speed and Latitude represent the corresponding coefficients in the regression equation whereas sigma is the residual standard deviation. Panel B: Dual-exponential profile. The columns Intercept, Wind speed and Latitude represent the corresponding parameters of the dual-exponential profile and RMSE is the root-mean-square error of the fit.

LMI distribution for each ENSO phase independently. We found that the differences between the post-processing methods are marginal because the simulated tracks remain the same. The post-processing only influences the likelihood of a track of being accepted or rejected (minimum speed of 18 ms^{-1}). In other words, the post-processing method impacts the intensity distribution (as shown in Section 4.5) but not the spatial patterns of ENSO anomalies, which is clearly driven by the CESM.

4.4 Size and radial profile

Following the methodology described in Section 2.5, we calibrated the size and radial profile components of the model. Table 2 - Panel A shows the parameter estimates for the RMW model (Eq. 7a in Willoughby et al. (2006)) and the sigma from the regressions (columns) for each basin (rows). In Panel B we provide the parameters (columns) for Equation 1 and the root mean square error for each basin (rows) .

We find that the "Wind speed" coefficient is negative and statistically significant (p-value below 0.1%) in all basins, meaning that: (1) wind speed is a significant driver of RMW, and that (2) RMW tends to decrease with stronger winds. In the North Atlantic basin, this value is consistent with Willoughby et al. (2006) Eq. 7a (-0.0155 in the latter and -0.0154 in our model). The effect of latitude is negative in the two Southern Hemisphere basins (both strongly statistically significant), and positive in the Northern Hemisphere with the exception of the North Indian (all statistically significant with the exception of the Eastern Pacific). From a physical standpoint, this means that RMW increases when tropical cyclones move away from the Equator (or approach the poles). Again, the values are comparable with Willoughby et al. (2006) Eq. 7a (0.0169 in the latter and 0.0163 in our model). The intercepts are also comparable with Willoughby et al. (2006). The residual standard deviations (sigmas) however indicate a large amount of uncertainty in the predictions. The predicted RMW can hence be multiplied by 1.5-2.5 (1-2 sigmas above or below the mean).

The calibrated wind profiles are presented in Panel B. We cannot easily compare coefficients from our model with Willoughby et al. (2006) Eq. 10c since we forced A to remain in the range $[0, 1]$. However, we see the coefficients for the wind speed are positive for all basins and those for the latitude are negative (positive) in the Northern (Southern) Hemisphere, as expected. The signs obtained in the North Atlantic are coherent with those in Willoughby et al. (2006) Eq. 10c. Moreover, the RMSE is about 8 knots for all basins, which is relatively small considering the radii provided in IBTrACS are for 34, 50, and 60 knots.

4.5 Event sets

Once all 1600 event sets are fully simulated, we have a complete set of tropical cyclone tracks with their corresponding intensity. We now aim to measure the intensity distribution; that is, the proportion of simulated tropical cyclones that reach a given Saffir-Simpson category.

Figure 9 shows the proportion of tropical cyclones that reach each Saffir-Simpson category in IBTrACS and in the simulations, without or with post-processing. The top (bottom) row corresponds to the North Atlantic (West Pacific) basin. The first column corresponds to the empirical frequency in IBTrACS, whereas the second represents the model without any post-processing of the LMI. The third and fourth columns show the simulated relative frequencies with two variants of post-processing based upon the overall basin-scale LMI distribution (3rd column) and by the LMI distribution for each ENSO phase (4th column). Exploring two variants of post-processing allows for the sensitivity of the post-processing technique to be tested and allows for users to be able to choose event sets and catalogs that are tuned to either a general year or a particular ENSO phase.

We observe that the model overestimates tropical storms but underestimates stronger storms in the North Atlantic. Applying either post-processing method significantly improves the overall intensity distribution, especially the correction method based upon the overall distribution of the LMI. In the Western Pacific, the model without post-processing behaves well but the overall post-processing method results in the best fit overall. Elsewhere, the model tends to underestimate Cat4-5 storms, but again, the bias correction based upon the overall LMI distribution does best at replicating observed intensities.

4.6 Annual catalogs

In this last subsection, we analyze the behavior of annual catalogs, which therefore include the frequency component and the resampling step. We have organized the 1 million years of events into 25,000 IBTrACS-like synthetic datasets to study the variability that naturally occurs over 40-year histories.

Each panel of Figure 10 provides an histogram of simulated proportions of storms per category as measured in each of the 25,000 synthetic datasets, whereas the vertical line provides the historical proportion observed in IBTrACS. For example, in the North Atlantic basin, approximately 25% (10%) of historical tropical cyclones have reached maximum intensity of Cat1 (Cat4). However, accounting for the natural variability, the share of Cat1 (Cat4) storms in a 40-year history could have been 13% to 38% (0% to 25%). The location of the vertical lines, derived from the observed 40-year history in IBTrACS falls within the realistic range, which is close to the statistical mode in each category. This is expected given how each component has been calibrated and given the post-processing applied. We obtain similar results in the other five basins.

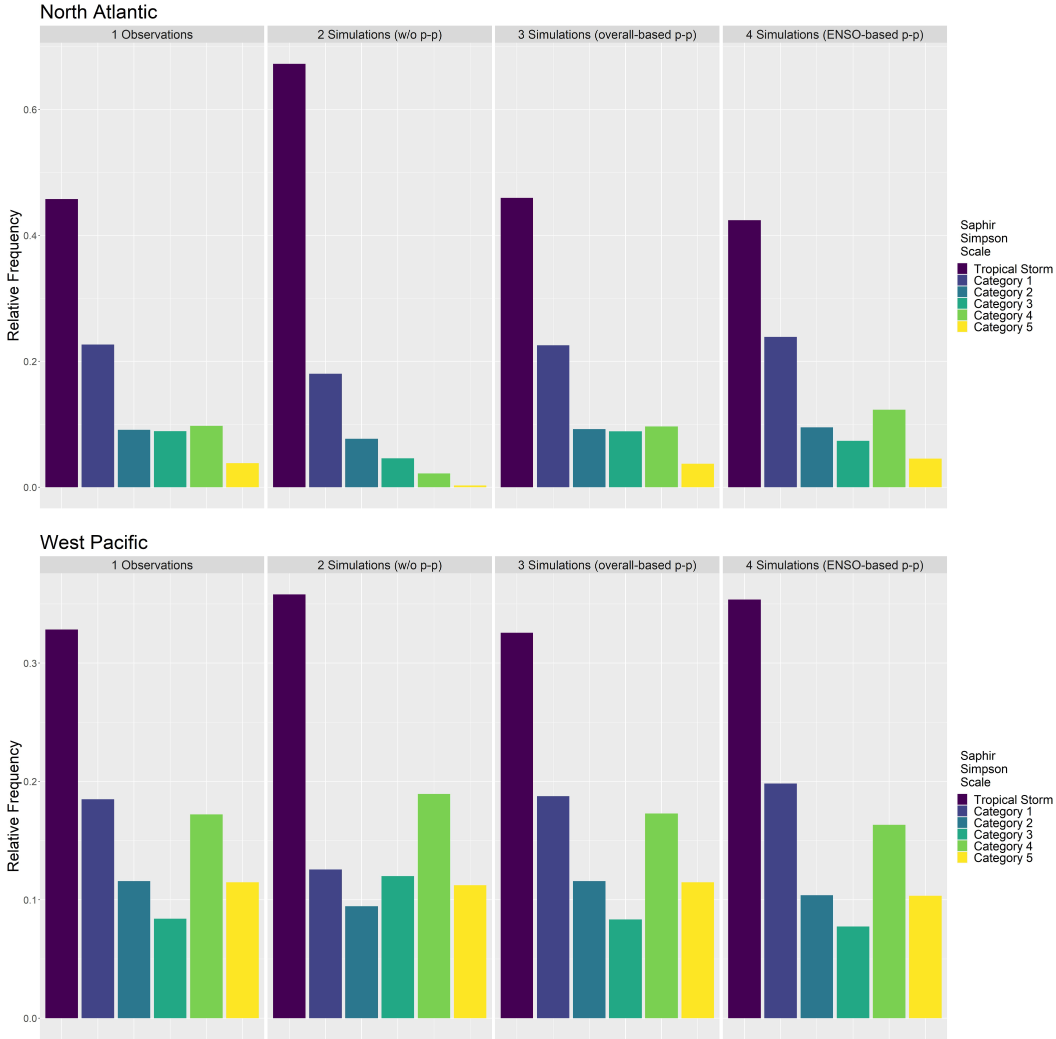

Figure 9: Simulated and observed intensity distribution in the North Atlantic (top) and West Pacific (bottom). Panel 1: Observations. Panel 2: Simulations without post-processing (p-p). Panel 3: Simulations with post-processing based upon overall distribution of LMI. Panel 4: Simulations with post-processing based upon distribution of LMI per ENSO phase.

5 Risk Maps

The annual catalogs can be used to produce landfall risk maps which are extremely useful for socioeconomic studies and financial risk management. In this section, we provide risk maps from simulations for Cat1+ and Cat4-5 tropical cyclones. As in Section 4, the maps shown cover the North Atlantic and West Pacific basins, whereas maps for all basins are provided in the Supporting Information.

For each 2-km grid cell of land, we have computed the average annual hit rate, including direct and indirect hits, from Cat1+ and Cat4-5 tropical cyclones. We have used 1 million years of events to compute return periods, as the inverse of the average annual hit rate. The left (right) panel of Figure 11 shows a risk map for the North Atlantic (West Pacific) basin for Cat1+ tropical cyclones whereas Figure 12 is similar but for Cat4-5

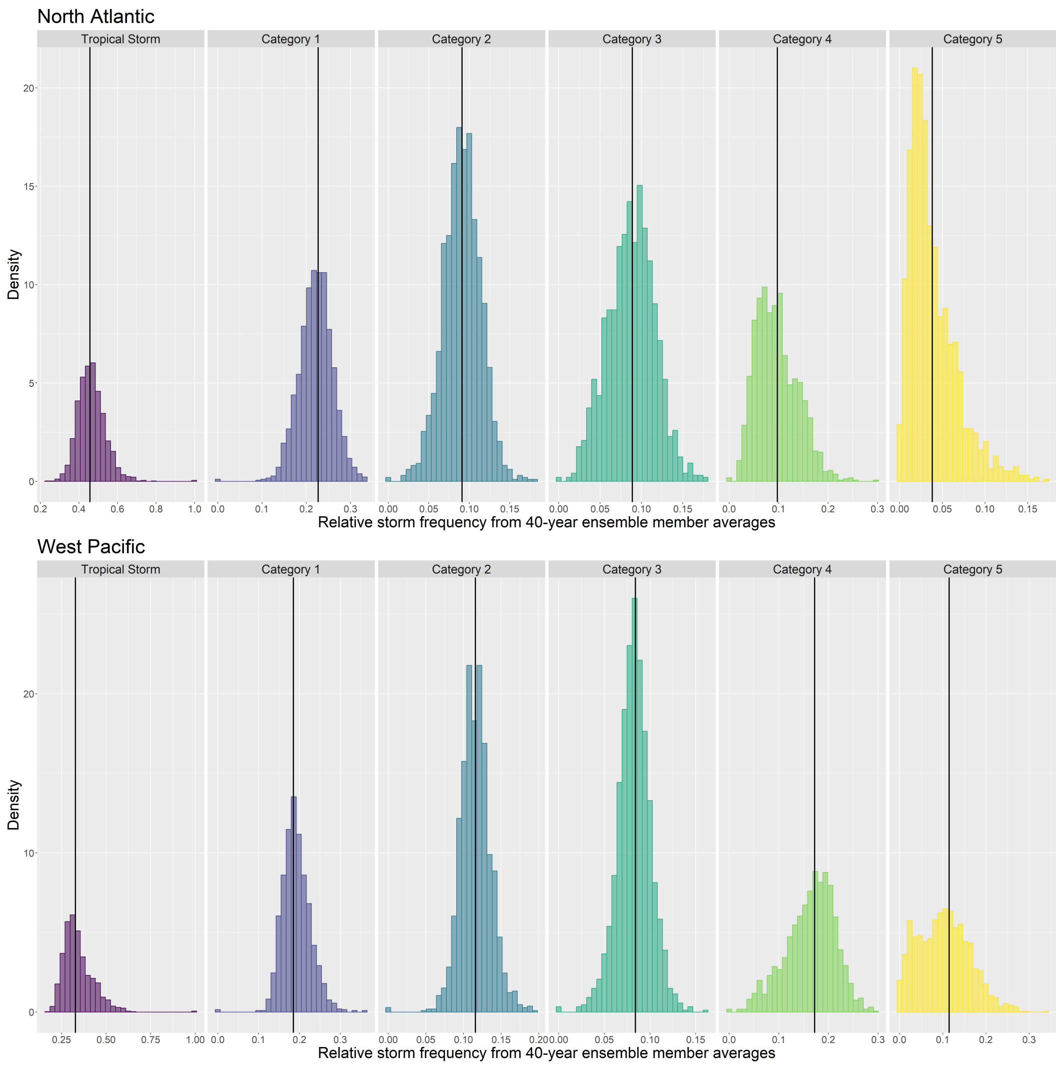

Figure 10: Relative storm frequency over 40-year ensemble members per Saffir-Simpson category (TS to Cat5) in the North Atlantic (top) and West Pacific (bottom). The vertical lines represent the observed proportions for each category (IBTrACS).

tropical cyclones. We compare Cat1+ to results from Bloemendaal et al. (2020) since that study is of comparable resolution and integrated storm size and a model for the radial wind profile.

The left panel of Figure 11 shows that the riskiest locations for landfalling Cat1+ tropical cyclones are expectedly the American and Mexican coasts of the Gulf of Mexico, the Antilles, the U.S. coasts of Virginia and North Carolina. These regions of low return period (high risk) are generally comparable to Bloemendaal et al. (2020), as are the general reduction in risk in the coastal U.S. north of Delaware. However, our rare storms (return periods of 1 in 1000 to 1 in 10000 years) of Cat1+ intensity penetrate further into the coast, and return periods are lower (more risk) in Nova Scotia and Newfoundland than shown in Bloemendaal et al. (2020). The riskiest locations for Cat4-5 hurricanes (Figure 12) in the North Atlantic are the American Coast of the Gulf of Mexico, Florida and the East Coast of the U.S.

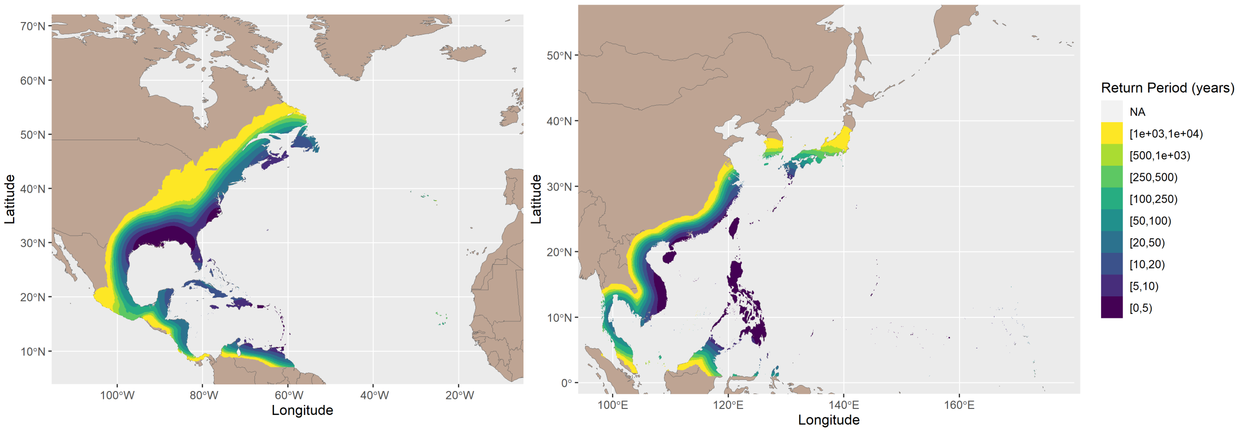

Figure 11: Average annual number of hits (expressed in return period) for Cat1+ storms over the North Atlantic (left) and West Pacific (right)

In the West Pacific, the riskiest locations for Cat1+ typhoons (right panel of Figure 11) are Southern Japan, Taiwan, East Coast of mainland China, Philippines, Vietnam and Cambodia. The high risk regions are generally consistent with Bloemendaal et al. (2020), and we produce a similar footprint of storms' entry into the coast from Vietnam to the Chinese coast to 35°N. Our model results in higher return periods (less risk) in central Japan than Bloemendaal et al. (2020), and Cat1+ storms do not reach Northern Japan, and Northeastern China via the Yellow Sea and Sea of Japan. Though, Cat1+ storms in these areas are rare Cat4-5 typhoons (right panel of Figure 12), show highest risk in the Northeastern Philippines, the Okinawa Japanese prefecture and Taiwan.

6 Discussion and Conclusion

We presented a global modelling framework to randomly generate tropical cyclones (tracks, size and radial profile) based upon the environmental conditions simulated by the CESM Large Ensemble over the present climate. This framework provides a unique and flexible approach for studying risk management of tropical cyclones by generating a large ensemble of TC trajectories that are statistically coherent with observations yet also consistent with interannual climate variability and historical climate change.

The model will be of value to climate and environmental scientists investigating interannual climate variability, event attribution, and downscaling techniques. The hit rates presented and supplemented by impact measures can be of use in socioeconomic and impact research investigating risk mitigation and trends in affected population or financial losses. The modeling framework is also of particular interest to the insurance and reinsurance industry due to its global perspective and direct link to climate models. These two aspects will allow the insurance industry to better constrain the impacts

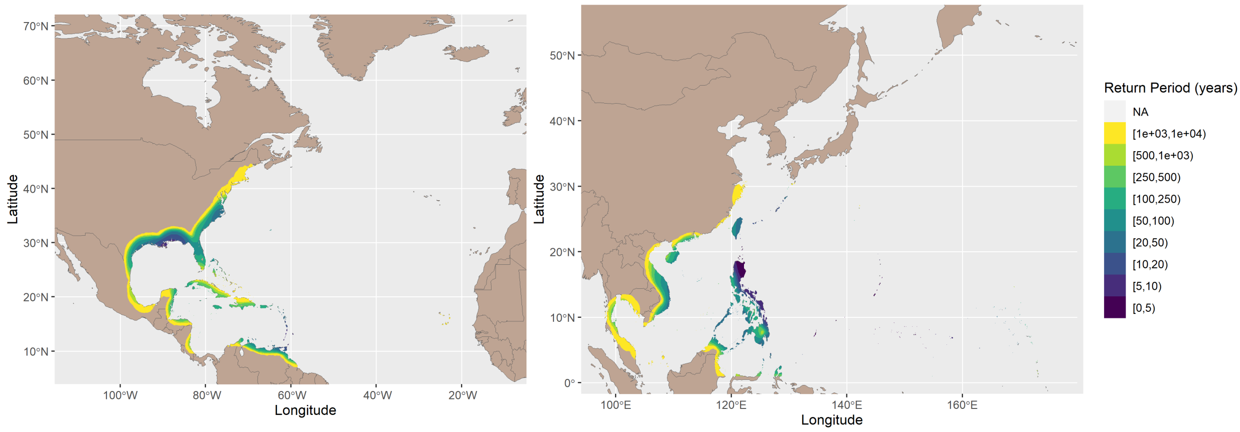

Figure 12: Average annual number of hits (expressed in return period) for Cat4 and above storms over the North Atlantic (left) and West Pacific (right)

of ENSO and other teleconnections on their global portfolios, which can in turn affect pricing, setting of reserves, and the diversification of tropical cyclone risk. The approach presented here also lays the required foundations for physical risk assessments of TC impacts under projected climate scenarios as will soon be required by regulating and accounting bodies globally (Financial Stability Board, 2017; Bank of England, 2019).

The CESM Large Ensemble has proven to be an important tool to expand the short observational record of reliable tropical cyclone measurements. As such, it can improve our understanding of the effects of ENSO on tropical cyclones, and their interactions with the seasonal frequency, cyclogenesis and track locations, wind speeds and radii. By calibrating the model and post-processing the outputs to past observations, it allows a faithful representation of key dynamics of tropical cyclones while leaving enough room to replicate the large spatial and temporal variability inherent to tropical cyclones. By directly connecting the components of tropical cyclones to the CESM Large Ensemble, the modeling framework therefore provides the appropriate foundations to assess the impacts of climate change on each of the tropical cyclone components. We leave such analysis for future research.

Data Availability Statement

The International Best Track Archive for Climate Stewardship (IBTrACS) dataset is available at: `https://www.ncei.noaa.gov/products/international-best-track-archive` (Knapp et al., 2018). The CESM Large Ensemble dataset is available at `https://www.earthsystemgrid.org/` and the authors acknowledge CESM Large Ensemble Community Project and supercomputing resources provided by NSF/CISL/Yellowstone (Kay et al., 2015). The ETOPO1 Global Relief Model was accessed at `https://www.ngdc.noaa.gov/mgg/global/relief/` (Amante & Eakins, 2009; NGDC, 2009).

The Supporting Information is available on Zenodo at `https://doi.org/10.5281/zenodo.7832839` and consists of 1) supporting figures and 2) supporting data (Carozza et al., 2023). The supporting figures are two HTML files that interactively display the figures for all basins. The supporting data contains event sets, catalogs, and an example analysis using the catalogs.

Acknowledgments

This work was supported by Mitacs through the Mitacs Accelerate program. This work was partially funded by AXA XL, the property & casualty and specialty risk division of AXA. We acknowledge the support of the Fonds de recherche du Québec – Nature et technologies (FRQNT), [funding reference number 119908]. Cette recherche a été financée par le Fonds de recherche du Québec – Nature et technologies (FRQNT), [numéro de référence 119908]. We acknowledge the support of the Natural Sciences and Engineering Research Council of Canada (NSERC), [funding reference number PDF-502939-2017]. Cette recherche a été financée par le Conseil de recherches en sciences naturelles et en génie du Canada (CRSNG), [numéro de référence PDF-502939-2017]. This work was also supported by a Marine Environmental Observation, Prediction and Response Network (MEOPAR) Postdoctoral Fellowship Award (PDF-13-2019).

The first two authors contributed equally to this work.

The authors declare that there is no conflict of interest regarding the publication of this article.

The authors would like to thank Tom Philp, Ioana Dima-West and Alec Vessey for their support and feedback in earlier stages of this work.

References

Amante, C., & Eakins, B. (2009). ETOPO1 1 arc-minute global relief model: Procedures, data sources and analysis. *NOAA Technical Memorandum NESDIS NGDC-24. National Geophysical Data Center, NOAA. [January 15, 2021].*. doi: https://doi.org/10.7289/V5C8276M

Aznar-Siguan, G., & Bresch, D. N. (2019). Climada v1: a global weather and climate risk assessment platform. *Geoscientific Model Development*, *12*(7), 3085–3097.

Bank of England. (2019). *The 2021 biennial exploratory scenario on the financial risks from climate change.* Bank of England.

Baudouin, J.-P., Caron, L.-P., & Boudreault, M. (2018, July). Impact of reanalysis boundary conditions on downscaled atlantic hurricane activity. *Climate Dynamics*, *52*(5-6), 3709–3727. Retrieved from `https://doi.org/10.1007/s00382-018-4352-7` doi: 10.1007/s00382-018-4352-7

Bell, R., Hodges, K., Vidale, P. L., Strachan, J., & Roberts, M. (2014, August). Simulation of the global ENSO–tropical cyclone teleconnection by a high-resolution coupled general circulation model. *Journal of Climate*, *27*(17), 6404–6422. Retrieved from `https://doi.org/10.1175/jcli-d-13-00559.1` doi: 10.1175/jcli-d-13-00559.1

Bister, M., & Emanuel, K. (2002). Low frequency variability of tropical cyclone potential intensity 1. interannual to interdecadal variability. *Journal of Geophysical Research*, *107*(D24). Retrieved from `https://doi.org/10.1029/2001jd000776` doi: 10.1029/2001jd000776

Bloemendaal, N., de Moel, H., Muis, S., Haigh, I. D., & C.J.H. Aerts, J. (2020, November 10). Estimation of global tropical cyclone wind speed probabilities using the storm dataset. *Scientific Data*, *7*, 1–11. doi: 10.1038/s41597-020-00720-x

Bloemendaal, N., de Moel, H., Martinez, A. B., Muis, S., Haigh, I. D., van der Wiel, K., ... others (2022). A globally consistent local-scale assessment of future tropical cyclone risk. *Science advances*, *8*(17), eabm8438.

Bloemendaal, N., Haigh, I. D., de Moel, H., Muis, S., Haarsma, R. J., & Aerts, J. C. J. H. (2020, February). Generation of a global synthetic tropical cyclone hazard dataset using STORM. *Scientific Data*, *7*(1). Retrieved from `https://doi.org/10.1038/s41597-020-0381-2` doi: 10.1038/s41597-020-0381-2

Bove, M. C., O'Brien, J. J., Eisner, J. B., Landsea, C. W., & Niu, X. (1998, November). Effect of el niño on u.s. landfalling hurricanes, revisited. *Bulletin of the American Meteorological Society*, *79*(11), 2477–2482. Retrieved from `https://doi.org/10.1175/1520-0477(1998)079<2477:eoenoo>2.0.co;2` doi: 10.1175/1520-0477(1998)079⟨2477:eoenoo⟩2.0.co;2

Caron, L.-P., Jones, C. G., & Winger, K. (2011). Impact of resolution and downscaling technique in simulating recent atlantic tropical cylone activity. *Climate dynamics*, *37*, 869–892.

Carozza, D. A., Boudreault, M., Grenier, M., & Caron, L.-P. (2023, May). *A global hybrid tropical cyclone risk model based upon statistical and coupled climate models - supporting figures and data.* Zenodo. Retrieved from `https://doi.org/10.5281/zenodo.7832839` doi: 10.5281/zenodo.7832839

Chan, K. T. F., & Chan, J. C. L. (2015). Global climatology of tropical cyclone size as inferred from quikscat data. *International Journal of Climatology*, *35*(15), 4843-4848. Retrieved from `https://rmets.onlinelibrary.wiley.com/doi/abs/10.1002/joc.4307` doi: https://doi.org/10.1002/joc.4307

Chavas, D. R., & Emanuel, K. (2014, April). Equilibrium tropical cyclone size in an idealized state of axisymmetric radiative-convective equilibrium. *Journal of the Atmospheric Sciences*, *71*(5), 1663–1680. Retrieved from `https://doi.org/10.1175/jas-d-13-0155.1` doi: 10.1175/jas-d-13-0155.1

CRED. (2021). *Disaster year in review 2020: Global trends and perspectives* (No. 62). Center for Research on the Epidemiology of Disasters. Retrieved from `https://cred.be/sites/default/files/CredCrunch62.pdf`

Dean, L., Emanuel, K., & Chavas, D. R. (2009, July). On the size distribution of atlantic tropical cyclones. *Geophysical Research Letters*, *36*(14). Retrieved from `https://doi.org/10.1029/2009gl039051` doi: 10.1029/2009gl039051

Demaria, M., & Kaplan, J. (1994, September). Sea surface temperature and the maximum intensity of atlantic tropical cyclones. *Journal of Climate*, *7*(9), 1324–1334. Retrieved from `https://doi.org/10.1175/1520-0442(1994)007<1324:sstatm>2.0.co;2` doi: 10.1175/1520-0442(1994)007⟨1324:sstatm⟩2.0.co;2

Easterling, D. R., Meehl, G. A., Parmesan, C., Changnon, S. A., Karl, T. R., & Mearns, L. O. (2000, September). Climate extremes: Observations, modeling, and impacts. *Science*, *289*(5487), 2068–2074. Retrieved from `https://doi.org/10.1126/science.289.5487.2068` doi: 10.1126/science.289.5487.2068

Emanuel, K. (2011). Global warming effects on u.s. hurricane damage. *Weather, Climate, and Society*, *3*(4), 261 - 268. Retrieved from `https://journals.ametsoc.org/view/journals/wcas/3/4/wcas-d-11-00007_1.xml` doi: https://doi.org/10.1175/WCAS-D-11-00007.1

Emanuel, K. (2013). Downscaling cmip5 climate models shows increased tropical cyclone activity over the 21st century. *Proceedings of the National Academy of Sciences*, *110*(30), 12219–12224.

Emanuel, K. (2015, October). Effect of upper-ocean evolution on projected trends in tropical cyclone activity. *Journal of Climate*, *28*(20), 8165–8170. Retrieved from https://doi.org/10.1175/jcli-d-15-0401.1 doi: 10.1175/jcli-d-15-0401.1

Emanuel, K. (2017, May). A fast intensity simulator for tropical cyclone risk analysis. *Natural Hazards*, *88*(2), 779–796. Retrieved from https://doi.org/10.1007/s11069-017-2890-7 doi: 10.1007/s11069-017-2890-7

Emanuel, K., DesAutels, C., Holloway, C., & Korty, R. (2004, April). Environmental control of tropical cyclone intensity. *Journal of the Atmospheric Sciences*, *61*(7), 843–858. Retrieved from https://doi.org/10.1175/1520-0469(2004)061<0843:ecotci>2.0.co;2 doi: 10.1175/1520-0469(2004)061⟨0843:ecotci⟩2.0.co;2

Emanuel, K., & Jagger, T. (2010, May). On estimating hurricane return periods. *Journal of Applied Meteorology and Climatology*, *49*(5), 837–844. Retrieved from https://doi.org/10.1175/2009jamc2236.1 doi: 10.1175/2009jamc2236.1

Emanuel, K., Ravela, S., Vivant, E., & Risi, C. (2006, March). A statistical deterministic approach to hurricane risk assessment. *Bulletin of the American Meteorological Society*, *87*(3), 299–314. Retrieved from https://doi.org/10.1175/bams-87-3-299 doi: 10.1175/bams-87-3-299

Emanuel, K., Sundararajan, R., & Williams, J. (2008). Hurricanes and global warming: Results from downscaling ipcc ar4 simulations. *Bulletin of the American Meteorological Society*, *89*(3), 347–368.

Emanuel, K., & Zhang, F. (2017, July). The role of inner-core moisture in tropical cyclone predictability and practical forecast skill. *Journal of the Atmospheric Sciences*, *74*(7), 2315–2324. Retrieved from https://doi.org/10.1175/jas-d-17-0008.1 doi: https://doi.org/10.1175/jas-d-17-0008.1

Fiedler, T., Pitman, A. J., Mackenzie, K., Wood, N., Jakob, C., & Perkins-Kirkpatrick, S. E. (2021, February). Business risk and the emergence of climate analytics. *Nature Climate Change*, *11*(2), 87–94. Retrieved from https://doi.org/10.1038/s41558-020-00984-6 doi: 10.1038/s41558-020-00984-6

Financial Stability Board. (2017). *Final report: Recommendations of the task force on climate-related financial disclosures.* Task Force on Climate-related Financial Disclosures.

François, B., Vrac, M., Cannon, A. J., Robin, Y., & Allard, D. (2020). Multivariate bias corrections of climate simulations: which benefits for which losses? *Earth System Dynamics*, *11*(2), 537–562. Retrieved from https://esd.copernicus.org/articles/11/537/2020/ doi: 10.5194/esd-11-537-2020

Goldenberg, S. B., & Shapiro, L. J. (1996). Physical mechanisms for the association of el niño and west african rainfall with atlantic major hurricane activity. *Journal of Climate*, *9*(6), 1169 - 1187. Retrieved from https://journals.ametsoc.org/view/journals/clim/9/6/1520-0442_1996_009_1169_pmftao_2_0_co_2.xml doi: https://doi.org/10.1175/1520-0442(1996)009⟨1169:PMFTAO⟩2.0.CO;2

Holland, G. (2008). A revised hurricane pressure–wind model. *Monthly Weather Review*, *136*(9), 3432–3445.

James, M., & Mason, L. (2005). Synthetic tropical cyclone database. *Journal of waterway, port, coastal, and ocean engineering*, *131*(4), 181–192.

Kalnay, E., Kanamitsu, M., Kistler, R., Collins, W., Deaven, D., Gandin, L., . . . Joseph, D. (1996, March). The NCEP/NCAR 40-year reanalysis project. *Bulletin of the American Meteorological Society*, *77*(3), 437–471. Retrieved from https://doi.org/10.1175/1520-0477(1996)077<0437:tnyrp>2.0.co;2 doi: 10.1175/1520-0477(1996)077⟨0437:tnyrp⟩2.0.co;2

Kaplan, J., & DeMaria, M. (1995). A simple empirical model for predicting the decay of tropical cyclone winds after landfall. *Journal of Applied Meteorology and Climatology*, *34*(11), 2499–2512.

Kara, A. B., Rochford, P. A., & Hurlburt, H. E. (2000, July). An optimal definition for ocean mixed layer depth. *Journal of Geophysical Research: Oceans*, *105*(C7), 16803–16821. Retrieved from https://doi.org/10.1029/2000jc900072 doi: 10.1029/2000jc900072

Kay, J. E., Deser, C., Phillips, A., Mai, A., Hannay, C., Strand, G., … Vertenstein, M. (2015, August). The community earth system model (CESM) large ensemble project: A community resource for studying climate change in the presence of internal climate variability. *Bulletin of the American Meteorological Society*, *96*(8), 1333–1349. Retrieved from https://doi.org/10.1175/bams-d-13-00255.1 doi: 10.1175/bams-d-13-00255.1

Kilroy, G., Smith, R. K., & Montgomery, M. T. (2016, January). Why do model tropical cyclones grow progressively in size and decay in intensity after reaching maturity? *Journal of the Atmospheric Sciences*, *73*(2), 487–503. Retrieved from https://doi.org/10.1175/jas-d-15-0157.1 doi: 10.1175/jas-d-15-0157.1

Knapp, K. R., Diamond, H. J., Kossin, J. P., Kruk, M. C., & Schreck, C. J. (2018). *International best track archive for climate, stewardship (ibtracs) project, version 4. [since 1980, all basins] [accessed june 27, 2021].* *NCEI* https://doi.org/10.25921/82ty-9e16. doi: https://doi.org/10.25921/82ty-9e16

Knapp, K. R., Kruk, M. C., Levinson, D. H., Diamond, H. J., & Neumann, C. J. (2010). The international best track archive for climate stewardship (ibtracs): Unifying tropical cyclone data. *Bulletin of the American Meteorological Society*, *91*(3), 363 - 376. doi: https://doi.org/10.1175/2009BAMS2755.1

Knutson, T., Camargo, S. J., Chan, J. C. L., Emanuel, K., Ho, C.-H., Kossin, J., … Wu, L. (2020, March). Tropical cyclones and climate change assessment: Part II: Projected response to anthropogenic warming. *Bulletin of the American Meteorological Society*, *101*(3), E303–E322. Retrieved from https://doi.org/10.1175/bams-d-18-0194.1 doi: 10.1175/bams-d-18-0194.1

Kreussler, P., Caron, L.-P., Wild, S., Loosveldt Tomas, S., Chauvin, F., Moine, M.-P., … others (2021). Tropical cyclone integrated kinetic energy in an ensemble of highresmip simulations. *Geophysical Research Letters*, *48*(5), e2020GL090963.

Lee, C.-Y., Camargo, S. J., Sobel, A. H., & Tippett, M. K. (2020). Statistical–dynamical downscaling projections of tropical cyclone activity in a warming climate: Two diverging genesis scenarios. *Journal of Climate*, *33*(11), 4815–4834.

Lee, C.-Y., Tippett, M. K., Camargo, S. J., & Sobel, A. H. (2015). Probabilistic multiple linear regression modeling for tropical cyclone intensity. *Monthly Weather Review*, *143*(3), 933–954.

Lee, C.-Y., Tippett, M. K., Sobel, A. H., & Camargo, S. J. (2016). Autoregressive modeling for tropical cyclone intensity climatology. *Journal of Climate*, *29*(21), 7815–7830.

Lee, C.-Y., Tippett, M. K., Sobel, A. H., & Camargo, S. J. (2018, January). An environmentally forced tropical cyclone hazard model. *Journal of Advances in Modeling Earth Systems*, *10*(1), 223–241. Retrieved from https://doi.org/10.1002/2017ms001186 doi: 10.1002/2017ms001186

Lin, I.-I., Camargo, S. J., Patricola, C. M., Boucharel, J., Chand, S., Klotzbach, P., … Jin, F.-F. (2020, October). *ENSO and tropical cyclones.* Wiley. Retrieved from https://doi.org/10.1002/9781119548164.ch17 doi: 10.1002/9781119548164.ch17

Meiler, S., Vogt, T., Bloemendaal, N., Ciullo, A., Lee, C.-Y., Camargo, S., … Bresch, D. (2022, March). Intercomparison of regional loss estimates from global synthetic tropical cyclone models. Retrieved from https://doi.org/10.21203/rs.3.rs-1429968/v1 doi: 10.21203/rs.3.rs-1429968/v1

Mitchell-Wallace, K., Jones, M., Hillier, J., & Foote, M. (2017). *Natural catastrophe* *risk management and modelling: A practitioner's guide.* John Wiley & Sons.

Moreno-Chamarro, E., Caron, L.-P., Loosveldt Tomas, S., Vegas-Regidor, J., Gutjahr, O., Moine, M.-P., ... Vidale, P. L. (2022). Impact of increased resolution on long-standing biases in highresmip-primavera climate models. *Geoscientific Model Development*, *15*(1), 269–289. Retrieved from `https://gmd.copernicus.org/articles/15/269/2022/` doi: 10.5194/gmd-15-269-2022

Nederhoff, K., Hoek, J., Leijnse, T., van Ormondt, M., Caires, S., & Giardino, A. (2021). Simulating synthetic tropical cyclone tracks for statistically reliable wind and pressure estimations. *Natural Hazards and Earth System Sciences*, *21*(3), 861–878. Retrieved from `https://nhess.copernicus.org/articles/21/861/2021/` doi: 10.5194/nhess-21-861-2021

NGDC. (2009). *ETOPO1 1 arc-minute global relief model. [Accessed January 15, 2021]. NCEI* `https://doi.org/10.7289/V5C8276M`.

Roberts, M. J., Camp, J., Seddon, J., Vidale, P. L., Hodges, K., Vannière, B., ... Wu, L. (2020, July). Projected future changes in tropical cyclones using the CMIP6 HighResMIP multimodel ensemble. *Geophysical Research Letters*, *47*(14). Retrieved from `https://doi.org/10.1029/2020gl088662` doi: 10.1029/2020gl088662

Schade, L. R., & Emanuel, K. (1999, February). The ocean's effect on the intensity of tropical cyclones: Results from a simple coupled atmosphere–ocean model. *Journal of the Atmospheric Sciences*, *56*(4), 642–651. Retrieved from `https://doi.org/10.1175/1520-0469(1999)056<0642:toseot>2.0.co;2` doi: https://doi.org/10.1175/1520-0469(1999)056⟨0642:toseot⟩2.0.co;2

Seneviratne, S., Zhang, X., Adnan, M., Badi, W., Dereczynski, C., Luca, A. D., ... Zhou, B. (2021). Weather and climate extreme events in a changing climate. *Climate Change 2021: The Physical Science Basis*, 1513–1766. Retrieved from `https://www.ipcc.ch/report/ar6/wg1/downloads/report/IPCC_AR6_WGI_Chapter11.pdf` doi: 10.1017/9781009157896.013

Strachan, J., Vidale, P. L., Hodges, K., Roberts, M., & Demory, M.-E. (2013). Investigating global tropical cyclone activity with a hierarchy of agcms: The role of model resolution. *Journal of Climate*, *26*(1), 133–152.

UNDRR, C. (2020). *Human cost of disasters: An overview of the last 20 years 2000-2019.* United Nations Office for Disaster Risk Reduction. Retrieved from `https://www.undrr.org/media/48008/download`

UNEP. (2019). *Insuring the climate transition: Enhancing the insurance industry's assessment of climate change futures.* United Nations Environment Programme. Retrieved from `https://www.unepfi.org/psi/wp-content/uploads/2021/01/PSI-TCFD-final-report.pdf`

Vickery, P. J., Skerlj, P. F., & Twisdale, L. A. (2000, October). Simulation of hurricane risk in the u.s. using empirical track model. *Journal of Structural Engineering*, *126*(10), 1222–1237. Retrieved from `https://doi.org/10.1061/(asce)0733-9445(2000)126:10(1222)` doi: 10.1061/(asce)0733-9445(2000)126:10(1222)

Wagner, R. G. (1996, July). Decadal-scale trends in mechanisms controlling meridional sea surface temperature gradients in the tropical atlantic. *Journal of Geophysical Research: Oceans*, *101*(C7), 16683–16694. Retrieved from `https://doi.org/10.1029/96jc01214` doi: 10.1029/96jc01214

Warszawski, L., Frieler, K., Huber, V., Piontek, F., Serdeczny, O., & Schewe, J. (2013, December). The inter-sectoral impact model intercomparison project (ISI–MIP): Project framework. *Proceedings of the National Academy of Sciences*, *111*(9), 3228–3232. Retrieved from `https://doi.org/10.1073/pnas.1312330110` doi: 10.1073/pnas.1312330110

Willoughby, H. E., Darling, R. W. R., & Rahn, M. E. (2006). Parametric representation of the primary hurricane vortex. part ii: A new family of sectionally continuous profiles. *Monthly Weather Review*, *134* (4), 1102 - 1120. Retrieved from https://journals.ametsoc.org/view/journals/mwre/134/4/mwr3106.1.xml doi: https://doi.org/10.1175/MWR3106.1

A Global Hybrid Tropical Cyclone Risk Model based upon Statistical and Coupled Climate Models

David A. Carozza[1], Mathieu Boudreault[1], Manuel Grenier[1,2], Louis-Philippe Caron[3]

[1]Department of Mathematics, Université du Québec à Montréal, Montréal, QC, Canada
[2]Climatic Hazards and Advanced Risk Modelling, The Co-operators General Insurance Company, Québec, QC, Canada
[3]Ouranos, Montréal, Canada

Key Points:

- We present a global tropical cyclone (TC) risk model built upon a climate model large ensemble that can be used for risk analysis.
- We integrate ENSO into our model since it is a strong driver of storm annual frequency, cyclogenesis, trajectories, and intensity.
- We present global risk maps consistent with statistical features of TC components and coherent with a global climate model.

Corresponding author: Mathieu Boudreault, `boudreault.mathieu@uqam.ca`

Abstract

Tropical cyclones (TCs) are among the most destructive natural hazards and yet, quantifying their financial impacts remains a significant methodological challenge. It is therefore of high societal value to synthetically simulate TC tracks and winds to assess potential impacts along with their probability distributions for e.g., land use planning and financial risk management. A common approach to generate TC tracks is to apply storm detection methodologies to climate model output, but such an approach is sensitive to the method and parameterization used and tends to underestimate intense TCs. We present a global TC model that melds statistical modeling, to capture historical risk features, with a climate model large ensemble, to generate large samples of physically-coherent TC seasons. Integrating statistical and physical methods, the model is probabilistic and consistent with the physics of how TCs develop. The model includes frequency and location of cyclogenesis, full trajectories with maximum sustained winds and the entire wind structure along each track for the six typical cyclogenesis basins from IBTrACS. Being an important driver of TCs globally, we also integrate ENSO effects in key components of the model. The global TC model thus belongs to a recent strand of literature that combines probabilistic and physical approaches to TC track generation. As an application of the model, we show global risk maps for direct and indirect hits expressed in terms of return periods. The global TC model can be of interest to climate and environmental scientists, economists and financial risk managers.

Plain Language Summary

Tropical cyclones (TCs) are among the most destructive natural hazards and yet, quantifying their financial impacts remains a difficult task. Being able to randomly simulate TCs and their features (such as wind speed) with mathematical models is therefore critical to build scenarios (and their corresponding probability) for land use planning and financial risk management. A common approach is to simulate TCs by tracking them directly in climate model outputs but this often underestimates the frequency of intense TCs while being computationally costly overall to generate a large number of events. For these reasons, many authors have looked into alternative approaches that replicate key physical features of TCs but rather using statistical models that are much less computationally demanding. This paper therefore presents a global TC model that leverages the strengths of both statistical and climate models to simulate a large number of TCs whose features are consistent with the physics and observations. As an important global phenomenon that affects TCs globally, we also integrate in our model the effects of El Niño. The paper focuses on the methodology and validation of each model component and concludes with global risk maps for direct and indirect hits.

1 Introduction

Tropical cyclones (TCs) consistently rank as one of the most significant climate extremes (Easterling et al., 2000), both in terms of casualties and economic losses (CRED, 2021; UNDRR, 2020). Coastal communities, local and regional stakeholders, and the insurance and reinsurance industry have first-hand experience of the adverse effects of tropical cyclones. However, modelling the impacts of TCs remains an important challenge for risk management (UNEP, 2019; Fiedler et al., 2021). Natural patterns of interannual climate variability, such as the El Niño-Southern Oscillation (ENSO), modulate TC features such as annual frequency, cyclogenesis, intensity, and duration over basins worldwide (Lin et al., 2020). The short observational records, the rarity of storms, and significant global variability in vulnerability and exposure contribute to large and complex uncertainties in global risk analyses. Moreover, climate change has the potential to perturb atmospheric and oceanic features that drive tropical cyclone activity (Knutson et al., 2020). In fact, a consensus is growing towards an increased likelihood of more intense and rainy storms, as well as an increased risk of flooding due to sea level rise (Seneviratne et al., 2021).

Climate impacts are commonly studied through the lens of general circulation models (GCMs) (Warszawski et al., 2013). However, when using climate model output, the frequency of tropical storms is sensitive to the method used to detect storm tracks (Roberts et al., 2020), and intensities are typically weaker than observed, with very intense storms being difficult to reproduce (Knutson et al., 2020). Although these issues improve with increasing model resolution (Caron et al., 2011; Strachan et al., 2013; Kreussler et al., 2021), climate models still have biases in their cyclogenesis locations, which, when combined with biases in the steering flows, make it difficult to reproduce observed landfalling statistics and thus render them unsuitable for risk modeling (Roberts et al., 2020). As such, purely physical approaches are not currently used in risk modeling applications, which require an accurate representation of observed tropical cyclone risk, and the ability to replicate the impact of extreme events, the latter necessitating a large number of simulations.

Risk modeling of tropical cyclone activity strives to provide an accurate representation of the potential damage associated with TCs over a given period of time. This can range from one year for underwriting in the (re)insurance industry, to years and decades for land use planning, and strategic policy- and decision-making. To maintain fidelity to historical observations, in particular for challenging features such as extreme winds and landfall rates, statistical models of storm frequency, cyclogenesis location, trajectory, intensity (maximum sustained winds and/or pressure), and size, are typically combined to represent the risk-driving components (Lee et al., 2018; Bloemendaal et al., 2020). This approach expands upon the historical record by generating a large number of tropical cyclone events over multiple years. Beginning with Vickery et al. (2000), studies have included environmental information from observational or reanalysis products as predictor variables to better represent the spatiotemporal variability of tropical cyclone components. Atmospheric reanalysis products in particular are increasingly used to build statistical and prognostic models (Emanuel, 2017; Lee et al., 2018; Bloemendaal et al., 2020).

TC risk models have long been developed by the catastrophe modelling industry, but a few of these models have appeared recently in the scientific literature. An ambitious intercomparison project of such TC models has emerged lately in Meiler et al. (2022). The authors analyzed the MIT (Emanuel et al., 2006, 2008), CHAZ (Lee et al., 2018), and STORM (Bloemendaal et al., 2020) models coupled with CLIMADA (Aznar-Siguan & Bresch, 2019) with the goal to simulate and compare economic damage due to winds under the present climate. The intercomparison found large variability between the participating models, and highlighted differences of approximately an order of magnitude in dollar-value impacts for low probability storms (1 in 10 years and rarer) and storms in basins with low annual frequency. We can also find applications of MIT, CHAZ and STORM models with CMIP5/6 climate models under both present and future climates in Emanuel (2013); Lee et al. (2020); Bloemendaal et al. (2022).

Here, we present a global TC wind risk model with statistical-dynamical components that is used in conjunction with a climate model large ensemble to generate large samples of TC seasons. Built using both statistical and physical methods, the model is probabilistic, consistent with the physics of tropical cyclones, and therefore highly flexible in nature. ENSO, which has a strong influence on TC activity in multiple basins, is used to define several model components and link statistical approaches to the environmental variables provided by a climate model (Bell et al., 2014). We connect the statistical and climate-driven aspects of our model by building statistically-generated trajectories and then calculating the intensity by means of Emanuel (2017). This approach couples TC model behaviour to the climate model's environment, while remaining faithful to the features of observed tracks. We also apply a post-processing methodology to

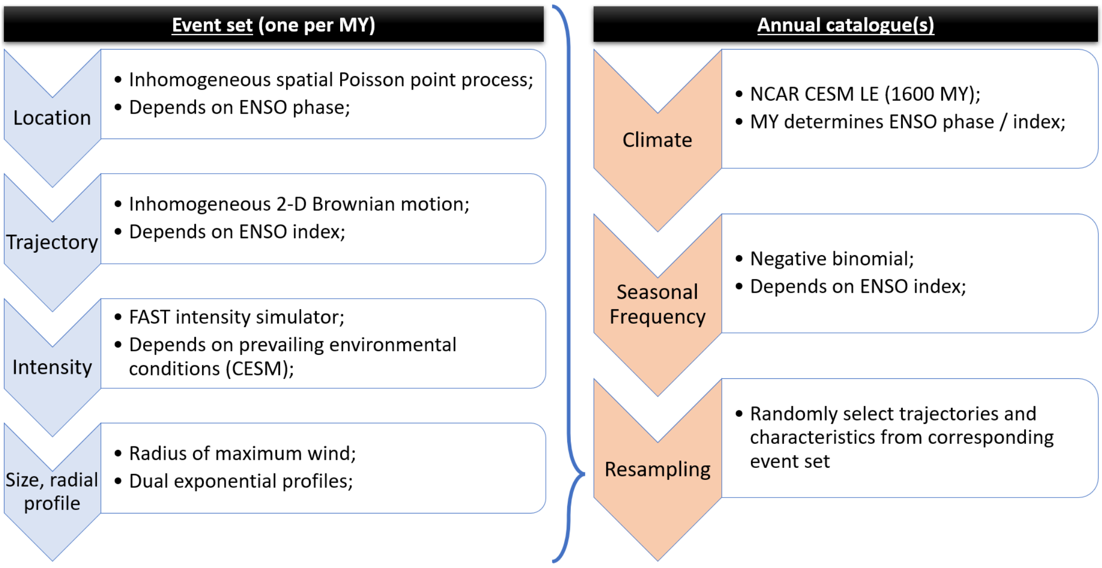

Figure 1: Global tropical cyclone model schematic detailing the components of the (1) the event set generation (left-hand side) and (2) the catalog generation (right-hand side).

the resulting storm intensity values to correct biases induced by the climate model. Finally, we calibrate the Willoughby et al. (2006) wind structure model for each cyclogenesis basin, thus providing a complete tropical cyclone wind model consistent with the present climate.

The output from our TC model consists of two components: 1) the event sets, and 2) the annual catalogs. Each event set is a fixed set of trajectories, with one set for every member and year of the climate model large ensemble. Annual catalogs are obtained by randomly sampling the trajectories from the event sets in accordance with the annual frequency of TCs in any given basin. Our overall model is in line with those analysed in Meiler et al. (2022) (MIT, CHAZ and STORM) and we will therefore borrow their nomenclature to compare each of our model's components with the latter. The model components and key steps are summarized in Figure 1.

The paper is structured as follows. Section 2 describes each model component, including statistical fits and simulations steps, leading to the generation of event sets (as shown on the left-hand side of Figure 1). Section 3 presents the annual frequency component and algorithm to generate annual catalogs (as shown on the right-hand side of Figure 1). We provide results and assess the quality of the global TC model in Section 4. Finally, we present risk maps expressed in terms of return periods in Section 5, and summarize key findings and conclude the paper in Section 6.

2 Event sets

This section focuses on the methodological steps leading to the construction of one event set per member and year (member-year or MY) of the climate model large ensemble. The underlying GCM is first presented in Section 2.1. Then, we present the modelling assumptions and fitting steps for each of the cyclogenesis (Section 2.2), trajectory (Section 2.3), intensity (Section 2.4), and size and radial profile (Section 2.5) components. We conclude this section with the simulation algorithm (Section 2.6) and the post-processing steps (Section 2.7) that reduce biases in the event sets. Whereas this section solely focuses on model features, calibration and simulation, we present in Section 4 model validation and evaluation results for the components or combination thereof.

2.1 Climate forcing

The global TC model is forced by the climate model output from the NCAR Community Earth System Model Large Ensemble (NCAR CESM-LE) (Kay et al., 2015) (K2015 from here on). As such, for a given MY (1600 or 40 members of 40 years in total taking model years between 1981 and 2020), we use the simulated atmospheric conditions to generate a specific event set and annual catalog over each basin. The climate model output therefore influences cyclogenesis location (through the corresponding ENSO phase), the trajectory (using the corresponding ENSO index) and wind speed (using the output of the CESM to feed the FAST model from Emanuel (2017), see Section 2.4). As a result, we are not trying to detect tropical cyclones from a GCM but are instead using the output from the NCAR CESM-LE to identify environments favorable to TC development and simulate how a TC would evolve and propagate in this environment.

This approach of forcing a climate model into a set of statistical models is similar to the original CHAZ model (Lee et al., 2018) which was forced with the ERA5 reanalysis, and Lee et al. (2020) which used CMIP5 models. The methodology is however significantly different from the STORM model which is fully stochastic and has no explicit forcing from climate models, and from the MIT model which is mostly physically driven.

2.2 Cyclogenesis location

Cyclogenesis location is defined as the first point of each trajectory as provided in the IBTrACS 4.0 database (Knapp et al., 2010, 2018). We consider all trajectories from the 1981 season to the present (IBTrACS dataset accessed June 27, 2021) with a lifetime maximum intensity (LMI) of at least tropical storm intensity (18 ms^{-1}). We follow the basin definitions from IBTrACS; that is, we analyze cyclogenesis locations for the North Atlantic (NA), Eastern North Pacific (EP, which includes the Central Pacific region), Western North Pacific (WP), North Indian (NI), South Pacific (SP) and South Indian (SI). The South Atlantic (SA) basin is therefore excluded.

We assume cyclogenesis is influenced by ENSO and use the ENSO phase (El Niño, Neutral and La Niña) as a driver of cyclogenesis location. We employ the Japan Meteorological Agency Sea Surface Temperature Anomaly index (ENSO JMA SSTA) because it performs well in selecting known ENSO phases. The index is defined in terms of the monthly average sea surface temperature anomaly over the Niño 3 region (4°N to 4°S, 150°W to 90°W). The anomaly index must be more (less) than 0.5°C (-0.5°C) over 6 consecutive 5-month periods to identify an El Niño (La Niña) (Bove et al., 1998).

Cyclogenesis locations are modeled using an inhomogeneous spatial Poisson point process. The spatial rate of cyclogenesis events is first calibrated to IBTrACS (longitude and latitude coordinates) for each phase and basin. It is computed as the generation rate of storms over a 2D (latitude-longitude) grid representing the basin, and is smoothed using a Gaussian kernel with a large bandwidth to allow for the potential formation of cyclones in rarer regions (standard deviation used as bandwidth of 5). Figure 2 (in Section 4) shows the generation rate for the North Atlantic and West Pacific for each ENSO phase (a similar plot is provided for each basin in the Supporting Information).

To simulate cyclogenesis locations, we first determine the ENSO phases in the CESM-LE. We follow the methodology of Bove et al. (1998), using sea surface temperature output from the CESM-LE to calculate the monthly ENSO JMA SSTA index and determine the ENSO phase for each MY. We apply the composite approach of Bell et al. (2014), which associates tropical cyclone seasons in the Northern Hemisphere (May-November) to the following ENSO event, and Southern Hemisphere seasons (October-May) to the ongoing ENSO event. Given the ENSO phase, we sample from an inhomogeneous spatial Poisson point process whose generation rate is that which was calibrated empirically.

Cyclogenesis in the original MIT model is based upon a random seeding approach which randomly draws locations in each cyclogenesis basin. To improve acceptance rates of cyclones, the CHAZ model therefore integrates the Tropical Cyclone Genesis Index (TCGI). The STORM cyclogenesis component is entirely empirical, randomly sampling in each grid cell according to observed monthly cyclogenesis rates. Our cyclogenesis component is therefore a hybrid between CHAZ and STORM whose cyclogenesis rate is spatially smoothed based upon observations for each ENSO phase and simulated locations are continuous in space, rather than fixed at the center of grid cells.

2.3 Trajectory

Storm trajectories are defined in terms of their zonal (easterly or westerly) and meridional (northerly or southerly) components for each trajectory segment. The trajectory model is built upon an inhomogeneous two-dimensional (2-D) Brownian motion. This approach generalizes trajectory models based on Markov chains on a 2-D grid (Emanuel et al., 2006; Nederhoff et al., 2021) while providing a stochastic representation of the beta and advection model (MIT, CHAZ). The underlying Brownian motion needs to be inhomogeneous to capture the Coriolis effect and steering winds, while being influenced by ENSO. We therefore model meridional and zonal displacements (or equivalently the angle and speed) of tropical cyclones using correlated normal distributions whose means and standard deviations are different per latitudinal band and ENSO index.

Fitting of the trajectory component is based upon IBTrACS using the same underlying tracks as in Section 2.2. The dataset represents storm movement over time steps of 6 hours. To capture the latitude-dependent structural features of tropical cyclone trajectories, displacements are first divided into latitudinal bands of at least 2 degrees, such that there are at least 30 data points (30 6-hour segments in IBTrACS) in each band. For each latitudinal band, we run linear regression models for both the meridional and zonal displacements whose sole predictor variable is the observed monthly ENSO JMA SSTA index (Bove et al., 1998). Standard deviations and correlations are then obtained from the residuals of the regressions. The overall approach is therefore rooted in James and Mason (2005) and similar to STORM, but instead we use smaller latitudinal bins, integrate ENSO in the regression equations and include correlations in the innovations to replicate the speed and angle structure.

To simulate a full trajectory, we first compute the ENSO index taken from the chosen MY of the NCAR CESM-LE and randomly sample cyclogenesis location knowing the ENSO phase and basin. Based on the corresponding latitudinal band and ENSO index, we sample meridional and zonal displacements from the corresponding bivariate normal distribution. This therefore provides a new location for the storm 6 hours later, and based on the latter, we sample new meridional and zonal displacements, and so on.

2.4 Intensity

The intensity model is based on the FAST (Emanuel, 2017) tropical cyclone wind simulator, which was designed to simulate large samples of tropical cyclone events. The model is defined by a set of 2 coupled nonlinear ordinary differential equations with surface circular wind speed and inner core moisture as prognostic variables. The two equations describe their evolution in terms of ocean interaction, ventilation, dissipative heating, and the pressure dependence of the surface saturation mixing ratio. These processes are not constructed from first principles but founded on empirical developments (Schade & Emanuel, 1999; Emanuel & Zhang, 2017) with the CHIPS ocean-atmosphere tropical cyclone model (Emanuel et al., 2004). FAST runs at speeds comparable to statistical models and has a performance comparable to the CHIPS model (Emanuel, 2017) which was used in the MIT model.

FAST requires potential intensity, vertical wind shear, storm translation speed, mixed layer depth, sub-mixed layer thermal stratification, and ocean bathymetry as input variables to represent tropical cyclone wind speed evolution. The atmospheric and oceanic input quantities determine the surface circular wind speed, whereas the bathymetry is used to represent interaction with the coast and landfall. Here, we use the output from each MY of the NCAR CESM-LE to compute maximum sustained wind speed along each simulated trajectory (the previous two steps). Table 1 shows the NCAR-CESM1 variables from the CESM-LE experiment used to calculate these forcing quantities.

Component	Variable	Reference
Vertical wind shear		
	Zonal wind (U, 250 hPa and 850 hPa)	K2015
	Meridional wind (V, 250 hPa and 850 hPa)	K2015
Potential Intensity		
	Atmospheric temperature (T)	K2015
	Sea surface temperature (T)	K2015
	Specific humidity (Q)	K2015
	Surface pressure (PS)	K2015
Mixed Layer Depth		
	Ocean temperature (TEMP)	K2015
Sub-Mixed Layer Thermal Stratification		
	Ocean temperature (TEMP)	K2015
Bathymetry		
	ETOPO1 Global Relief Model	Amante and Eakins (2009); NGDC (2009)

Table 1: Datasets used for tropical cyclone intensity component.

We follow Bister and Emanuel (2002) to calculate monthly maps of potential intensity. Mixed layer depth is taken to be the depth at which temperature is 1°C less than the sea surface temperature (Wagner, 1996; Kara et al., 2000) and sub-mixed layer thermal stratification is calculated from Emanuel (2015) by taking the vertical temperature gradient between the mixed layer depth and 100 meters below it. We use the ETOPO1 Global Relief Model (Amante & Eakins, 2009; NGDC, 2009) to represent bathymetry on a 1 arc-minute ($\sim$1.8 km) grid. This allows us to model the TC interaction with the coast and landfall at sufficiently high resolution, instead of using the CESM-LE bathymetry which is at a nominal resolution of $\sim$100 km. When the center of a tropical cyclone is located over the ocean based on the ETOPO1 grid but is over land based on the lower-resolution CESM grid, the oceanic CESM quantities (mixed layer depth and sub-mixed layer thermal stratification) are not defined. In this case, we calculate tropical cyclone intensity by using the most recent values of mixed layer depth and sub-mixed layer thermal stratification.

Time series of vertical shear, potential intensity, mixed layer depth, and sub-mixed layer thermal stratification are determined from their monthly grids depending on the location of the center of the storm and the day of year. For vertical shear and potential intensity, we apply a multilinear interpolation in space and time. Mixed layer depth and sub-mixed layer thermal stratification for each point of the storm track take the monthly mean value of the grid point of the storm center, since they change little from day to day

(Emanuel, 2017). For bathymetry, we also apply a multilinear interpolation in space to determine the bathymetry at the storm center.

Storm translation speed is calculated from the displacement components of the simulated trajectory. We follow Demaria and Kaplan (1994) to compute the zonal (U) and meridional (V) components of winds at 850 and 250 hPa and the magnitude of the vertical wind shear.

To run the FAST model, we interpolate linearly from the 6-hour trajectory timestep to the 4-minute timestep required for FAST. Following Emanuel (2017), we add 60% of the simulated translation velocity (from the trajectory component) to the storm-relative maximum intensity to arrive at the ground-relative peak wind speed (Emanuel & Jagger, 2010). The intensity model is applied to every trajectory of the event set based on the prevailing conditions of the corresponding MY. This physics-based component is therefore deterministic in the sense that two identical trajectories will yield identical winds along their tracks, but a slightly different trajectory might be enough to yield different winds.

The models from the intercomparison project of Meiler et al. (2022) each use different approaches to represent TC intensity. The MIT wind model is based upon the aforementioned CHIPS model. The CHAZ TC intensity is built on autoregressive models (Lee et al., 2015, 2016) whose predictors are derived from environmental conditions (including e.g., potential intensity, vertical wind shear, and mid-level relative humidity). In this case, simulated intensity is obtained by forcing the autoregressive models with a reanalysis or climate model. STORM randomly generates pressure change along the track with an autoregressive model similar to James and Mason (2005). Over the ocean, an empirical wind-pressure relationship is used to deduce wind speed, whereas overland, wind decays according to Kaplan and DeMaria (1995). The relationships for the STORM intensity component are fitted with observations (IBTrACS and reanalysis).

2.5 Size and radial profile

Important progress has been made in the state of knowledge of tropical cyclone size on both the empirical (Dean et al., 2009) and theoretical (Chavas & Emanuel, 2014) fronts, but key challenges remain to improve the understanding of its environmental determinants (Kilroy et al., 2016). Considering this, we take an empirical approach to represent tropical cyclone size and radial profiles. Given empirical differences in the distributions of size and radial profile in different basins, such as storms being largest in the West Pacific and smallest in the East Pacific (Chan & Chan, 2015), we recalibrate Willoughby et al. (2006) for each basin using IBTrACS' wind radii data available since approximately 2000.

Willoughby et al. (2006) assume that the log radius of maximum sustained wind ($\log(R_{\max})$ or RMW) is a linear function of maximum sustained winds ($V_{\max}$) and latitude (φ). The latter three variables are directly available in IBTrACS, which allows a linear regression model to be fit in each basin.

The next step is the calibration of the radial profile. Willoughby et al. (2006) showed that for many tropical cyclones, there might be a different rate of decay in the radial profile, especially away from the center. The radial profile component of our global model borrows the dual-exponential functional form from Willoughby et al. (2006) (Eq. 4). But given that IBTrACS only provides wind radii at 34, 50, and 60 kt for the NE, NW, SE, SW quadrants, not all parameters could be calibrated. As such, we fixed $X_1 = 300$ and $X_2 = 30$ and defined A as

$$A = \Phi\left(\beta_0 + \beta_1 V_{\max} + \beta_2 \varphi\right) \tag{1}$$

where Φ is the cumulative normal distribution function (probit function) that transforms an input in $\mathbb{R}$ to a value within $[0, 1]$. Both exponential decaying functions are therefore used and given a weight of A (that cannot be negative or above 1 in our model) that varies according to wind speed and latitude. To find the parameters β_0, β_1 and β_2 we then minimized the squared errors between Eq. 4 of Willoughby et al. (2006) and the IBTrACS profiles. Each observation of the radial profile takes the maximum radius over the four quadrants available. This process is repeated for each basin.

Simulation of the radial wind profile at a given location begins by computing the prediction of $R_{\max}$ from the linear regression using the simulated maximum winds from the intensity component, and latitude from the location of the trajectory. We then sample one normal random variable for the entire track and add noise to $R_{\max}$. This will simulate a radius for an entire track that is consistently above or below the mean, depending on the normal variate. This is done to avoid an accordion effect where the radius constantly increases or decreases around its predicted value over the track. Then, based upon the sampled $R_{\max}$, in addition to maximum winds and latitude, we deduce the entire wind profile from the dual-exponential function.

Modeling of the radial wind profile differs significantly across the models of the intercomparison project. Whereas the entire wind profile is provided by CHIPS in the MIT model, no wind profile is included by default with CHAZ. STORM simulates the RMW by sampling from observations depending on pressure in each of three stages: at genesis, peak intensity and dissipation. To overcome the discrepancies in available wind profiles, Meiler et al. (2022) couple each model with the same parametric wind field model from Holland (2008).

2.6 Algorithm

We now describe how the components are combined to generate event sets for each MY of the CESM-LE (see the left-hand side of Figure 1). When used in conjunction with vulnerability and exposure information, each event set thus forms the basis of event loss tables (ELTs) used in catastrophe modelling (Mitchell-Wallace et al., 2017).

For each basin and each of the 1600 CESM-LE member-years, we use the model to construct a set of accepted tropical cyclone trajectories that are consistent with the environmental conditions of the year in question. We refer to each of these as event sets that are connected by the following components:

1. Climate forcing: Based on the environmental conditions in the selected MY and basin, determine the ENSO phase and index;
2. Cyclogenesis location: Based on Step 1, simulate one cyclogenesis location from the ENSO-dependent cyclogenesis generation rate;
3. Trajectory: Based on Step 1 and the simulated cyclogenesis location from Step 2, simulate the entire trajectory (meridional and zonal displacements every 6 hours);
4. Intensity: Initialize trajectory intensity at the cyclogenesis location with a wind speed of 10 ms^{-1}, and calculate the intensity every 4 minutes using the FAST model over the entire trajectory with the climate model variables for the MY in question (Step 1). Add 60% of the translation velocity to the intensity to calculate the ground-relative intensity from the storm-relative intensity (Emanuel & Jagger, 2010);
5. Acceptance/Rejection: Retain trajectory if the lifetime maximum intensity (LMI) is 18 ms^{-1} or larger. End trajectory where the storm intensity falls below 2.5 ms^{-1}. If the storm is too weak and is therefore rejected, then repeat Steps 2-5;
6. Size and wind profiles: If the trajectory has a LMI above 30 ms^{-1} (Cat1+ storm), simulate the radius of maximum wind and radial profile. We use this threshold since wind damage is generally negligible for storm with intensity below 30 ms^{-1} (Emanuel, 2011).

To yield a sufficient number of tracks in each event set for the annual catalogs of Section 3, we want for the typical event set to contain as many trajectories as were observed from 1981 to 2020. The number of accepted tracks in each event set is random, and depends on the number of cyclogenesis locations simulated (which is random and simulated from the cyclogenesis density per ENSO phase), the trajectory paths (which are random but depend on the ENSO index), and on the favorability of the environmental conditions over the trajectories (which depend on the MY of the CESM-LE). Although the number of tracks is random for a given cyclogenesis density, we can increase or decrease the number of accepted tracks and preserve the spatial structure of the cyclogenesis densities by applying a constant multiplier. We determine the baseline number of accepted tracks, using the empirical cyclogenesis densities described in Section 2.2 with a sample of 50 event sets. Using such a multiplier, we can adjust the number of accepted tracks over all the event sets to be consistent with the number of observed tracks. For the North Atlantic basin, for example, we run the steps described above for 50 ensemble members and generate 50 event sets, and find that the mean number of accepted trajectories is 315. To therefore arrive at a mean number of tracks that is consistent with the 475 observed tracks over 1981-2020, we multiply the North Atlantic cyclogenesis densities by 1.5. With this adjusted cyclogenesis density, we find that the mean number of tracks over all of the event sets is 500.

2.7 Post-processing

Once we simulate full tracks for each of the 1600 MY, we observe that the global TC model tends to either underestimate or overestimate the relative proportions of stronger or weaker storms (e.g., proportion of Cat4-5 vs Cat1-3 storms when compared to observations over 1981-2020 in Figure 9). Section 4.5 provides a detailed account of these biases. Such biases are to be expected because the FAST intensity model is physically-based and of general applicability, but was forced and validated with output from the NCEP/NCAR Reanalysis (Kalnay et al., 1996), which by construction represents observed historical weather and climate conditions. The NCAR CESM-LE, on the other hand, is an ensemble of simulations from the NCAR Community Earth System model operating at a nominal resolution of $\sim$100 km. The NCAR CESM-LE, like other climate models, carries inherent biases (Moreno-Chamarro et al., 2022), and some of these biases will impact the downscaled TC activity. We do not expect the intensity biases to originate from the cyclogenesis and trajectory components of the model because they do not rely on output from CESM-LE.

To improve simulated intensities relative to observations, we adjusted the simulated lifetime maximum intensity (LMI) distribution. We suggest scaling simulated tropical cyclone wind speeds such that the quantiles of the simulated LMI distribution (over the 1600 MY) match observed quantiles (from IBTrACS). Such a correction is computed and applied in each basin using both the overall empirical LMI distribution or the empirical LMI distribution per ENSO phase. Throughout the paper, we used both approaches, depending on whether the focus is on the overall TC behavior or that per ENSO phase. A comparison is provided in Section 4.5 (and in Figure 9).

We opted for this uniquely post-processing approach as opposed to applying a bias-correction to the NCAR CESM-LE output (pre-processing) that is used as input. Bias corrections of climate data are widely applied, though have typically been conducted for a single variable and location, and as such are one-dimensional. Our use of the NCAR CESM-LE output, however, is highly multivariate (many climate variables) and multi-dimensional (many grid cells), and one-dimensional bias corrections of each climate variable required would not preserve the spatial and temporal dependence of the variables required.

Multivariate bias correction methods are gaining use, though challenges in applicability remain (François et al., 2020). The comparison of multivariate bias correction approaches by François et al. (2020) found that the methods did not represent temporal properties and performed increasingly poorly for increasingly large spatial domains (due to the higher dimensionality of the problem). Since the relevant spatial domain for representing the development of TC intensity, the basin, is large and high dimensional (i.e., it contains a large number of grid cells), and that the temporal dependence of the forcing climate variables is key to the FAST model, we did not rely on a pre-processing approach.

3 Annual catalogs

Because it provides a fixed number of tracks per MY, the information provided by an event set is rarely enough for socioeconomic studies or for risk management applications. The purpose of the catalog is therefore to provide a plausible representation of a tropical cyclone season for a given year. For each basin, member and year of the NCAR CESM-LE, we simulate the annual frequency of tropical cyclones based upon the conditions that prevail in the climate model output for that year and randomly sample the events from the corresponding event set. Repeating this process a large number of times creates a synthetic TC dataset whose structure replicates that of IBTrACS.

This section focuses on the key methodological aspects of generating annual catalogs as depicted on the right-hand side of Figure 1 whereas Section 4 evaluates and validates the components (or combination thereof) of the global TC model.

3.1 Frequency

The annual frequency represents the number of storms whose LMI reaches at least 18 ms^{-1} in a given year and basin. It is modeled with a negative binomial random variable whose mean depends upon the ENSO index. The negative binomial distribution generalizes the Poisson distribution by allowing overdispersion; that is, the variance of the counts can be larger than its mean. The Poisson distribution is a special case of the negative binomial distribution.

For each basin, we fit a negative binomial regression with the annual JMA SSTA index (JMA$_m$) (Bove et al., 1998) as the single predictor variable. For basins in the Northern and Southern Hemisphere, we take the observed JMA$_m$ to be the August-September-October and January-February-March mean, respectively, since these months cover the seasonal activity peaks (Bell et al., 2014). Although the Southern Hemisphere TC seasons take place from November-April, from here on we use the term annual to describe TC frequency. To simulate the annual frequency, we calculate the JMA$_m$ index from the CESM-LE sea surface temperature, compute the parameters of the negative binomial distribution from the fit, and then sample from the distribution.

Cyclogenesis location and frequency are typically intertwined components in the TC models of the intercomparison project. STORM sequentially samples the number of storms from a Poisson distribution with fixed mean, then simulates the cyclogenesis location of each storm. This differs however from the MIT and CHAZ models that both rely on randomly spatially distributed TC seeds while sampling storms until a desired number is attained. Whereas TC seeds are uniformly sampled in the MIT model which could lead to a small acceptance rate, the CHAZ model relies on the TCGI which improves its rate of acceptance. In the MIT approach, we typically aim to reach a fixed number of storms, which is important for the production of ELTs, but in the CHAZ model, frequency results from the accepted number of storms which is driven by the the TCGI. But as Meiler et al. (2022) remark, post-processing CHAZ's frequency of events is still required. In our paper, we borrow the MIT approach to generate a fixed number of storms in the event set production (left-hand side of Figure 1), whereas we use a typical count distribution to generate consistent seasonal frequency (right-hand side of Figure 1).

3.2 Algorithm

To build an annual catalog, we need to follow these steps. For each MY and basin:

1. Climate forcing: Based upon the environmental conditions observed in the selected MY and basin, determine the ENSO index;
2. (Annual) Frequency: Sample the number N of tropical cyclones that reach at least 18 ms^{-1} from a negative binomial distribution whose mean is based upon the ENSO index observed in Step 1;
3. Resampling: Randomly select N trajectories from the corresponding event set.

Using e.g., $N = 625$ simulations from the negative binomial distribution per MY, we get a combined number of 1 million years of events (625 times 1600) allowing for a better understanding of extremes. One year is made of a random number of tracks with their corresponding characteristics drawn from the event sets. Applying this algorithm thus provides the basis for year loss tables (YLTs) in typical catastrophe models (Mitchell-Wallace et al., 2017).

One can also organize catalogs differently to build synthetic IBTrACS-like datasets of 40 years of length. Indeed, each year from the CESM has 40 different members with 625 replications each and therefore, we get 25,000 synthetic IBTrACS-like (40 members times 625 simulations) datasets consistent with the climate of 1981-2020.

4 Model evaluation and results

In this section, we analyze the various features of the model. The analyses provided cover all six basins but for conciseness we only include the figures for the North Atlantic and West Pacific basins. The Supporting Information, provided as an interactive HTML document, allows the reader to view the same figures for all basins.

4.1 Cyclogenesis Location

Figure 2 shows the probability of cyclogenesis for tropical cyclones (with minimum wind speed of 18 ms^{-1}) by ENSO phase (La Niña on the left, Neutral in the middle, El Niño on the right) over the North Atlantic (top row) and West Pacific basins (bottom row). The shades of color represent the spatial probability density conditional upon having cyclogenesis. The darker the color, the more likely cyclogenesis is to occur at that particular location. The bandwidth chosen in the kernel density smoothing allows cyclogenesis in realistic but unobserved areas.

Based on Figure 2 and the Supporting Information, we find that cyclogenesis is more likely to occur over the East Coast of the US during El Niño, while cyclogenesis stretches westward in the Eastern Pacific and eastward in the West Pacific. Although there are important uncertainties since there are few TCs by ENSO phase in the North Indian basin, we find that cyclogenesis is more likely along the East Coast of India, and that TCs on the West Coast of India are more likely to emerge during El Niño. Cyclogenesis moves away from Australia during El Niño in the South Pacific and South Indian basins. The model therefore simulates cyclogenesis locations in accordance with the colored densities shown in Figure 2. It is important to note however the sample size spans only 40 years (study period over 1981-2020), with a relatively limited number of years in each El Niño or La Niña events.

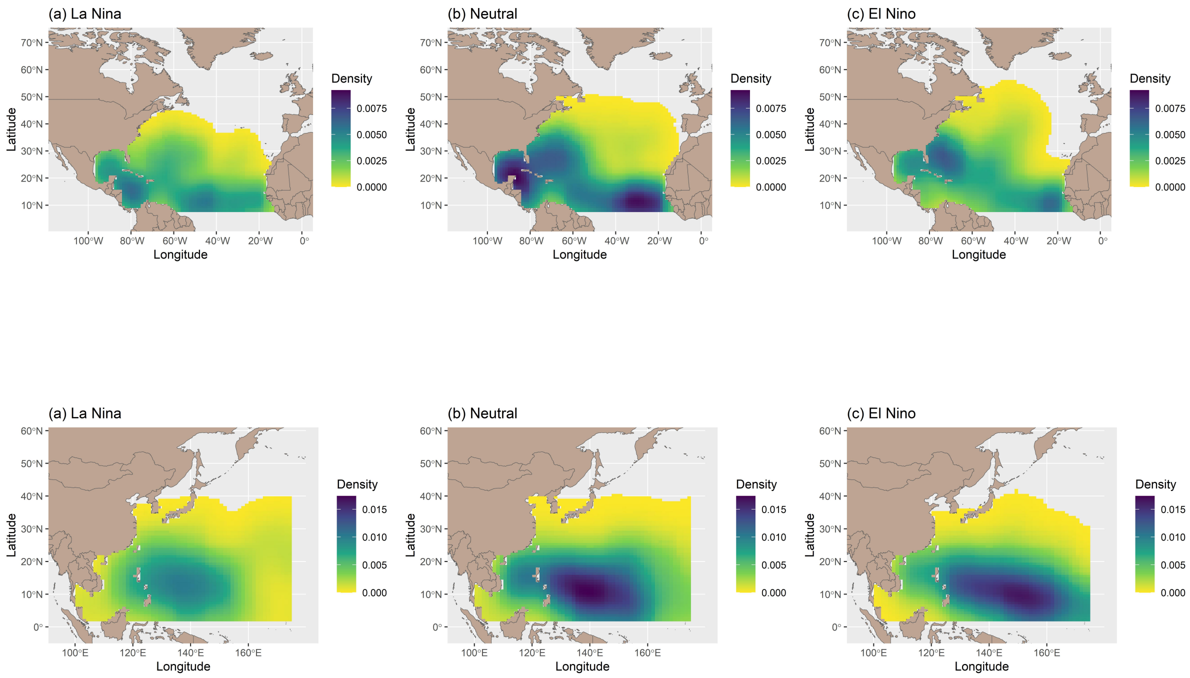

Figure 2: Probability of cyclogenesis in the North Atlantic (top) and West Pacific (bottom) per ENSO phase (Left: La Niña; Center: Neutral; Right: El Niño)

4.2 Trajectory

The zonal and meridional displacements in each latitudinal band are fitted with linear regressions, each with the ENSO index as predictor. The left-hand side of Figure 3 (Figure 4) shows the coefficients of the regressions (y-axis, km per degree C of ENSO anomaly) for each latitudinal band (x-axis, degrees, relative to the Equator) in the North Atlantic (West Pacific) basin for zonal (top row) and meridional (bottom row) displacements. The right-hand side of Figure 3 (Figure 4) shows the p-value of the ENSO predictor for each latitudinal band in the North Atlantic (West Pacific). The red horizontal lines are fixed at 10% (plain red line) and 5% (dotted red line) to determine over which latitudinal band ENSO exerts an influence.

For the North Atlantic, Figure 3 shows that during El Niño (high ENSO index) years there is a negative relationship on meridional displacements north of 23°N, indicating less northerly displacements (Figure 3c). Note that the mean meridional displacement in the North Atlantic is northerly, but during El Niño our fits show that the displacement is less northerly (not southerly) north of 23°N. Between 11 and 19°N, the relationship is instead positive, resulting in more northerly displacements during El Niño. Zonal displacements in most latitudinal bands are not statistically significant (Figure 3b), indicating a weak relationship to the ENSO index.

In the Supporting Information, we show that during El Niño years zonal and meridional displacements are less westerly and more northerly in the East Pacific between approximately 10 and 25°N. In the North Indian basin, El Niño years have less westerly

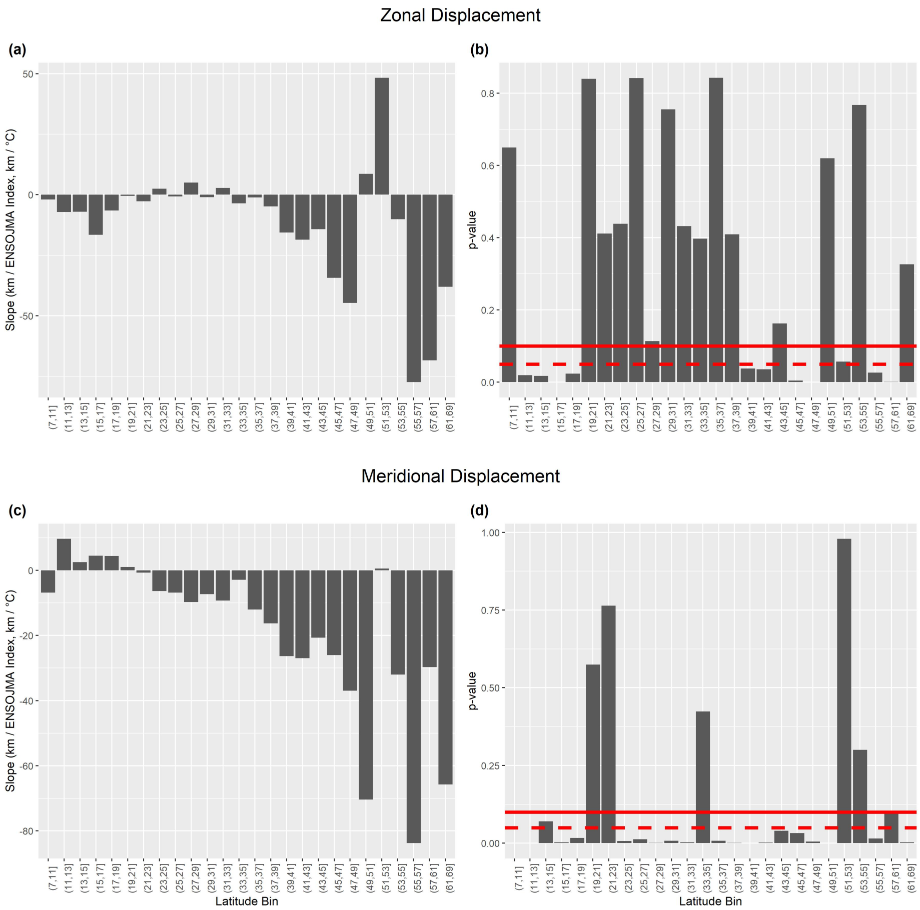

Figure 3: Summary results from statistical fits for zonal and meridional displacements in terms of the ENSO JMA index. Coefficients (left) and statistical significance (right) of the impact of ENSO on zonal (top) and meridional (below) displacements for each latitudinal band in the North Atlantic.

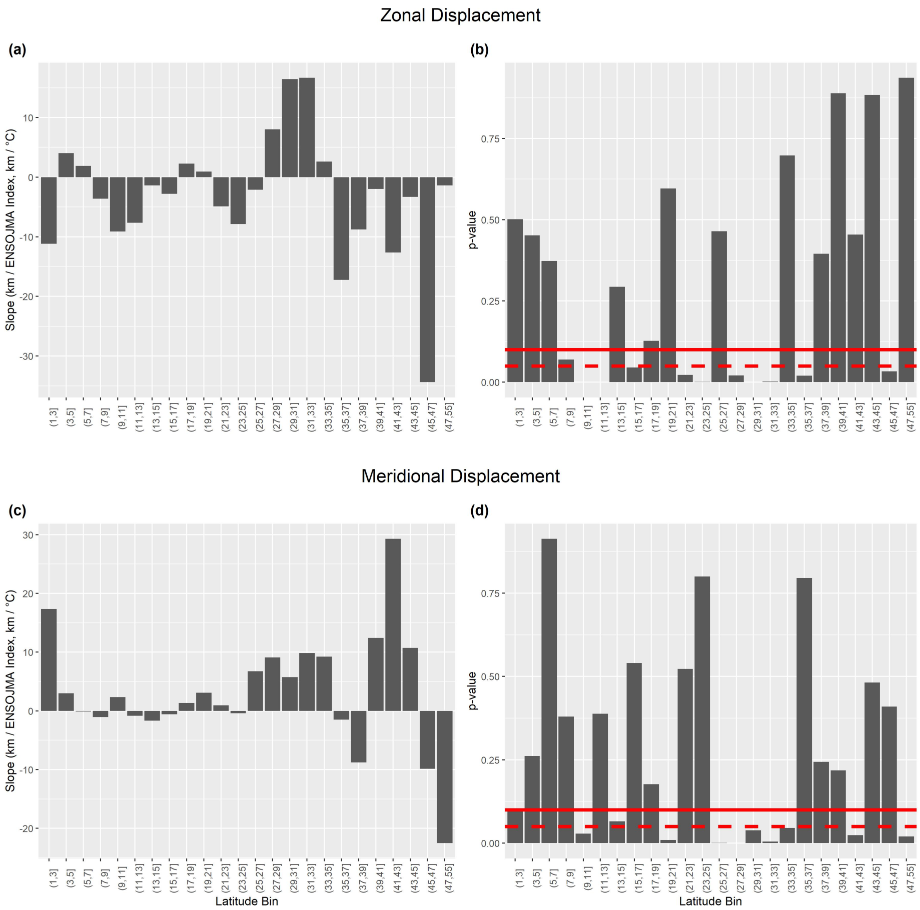

Figure 4: Summary results from statistical fits for zonal and meridional displacements in terms of the ENSO JMA index. Coefficients (left) and statistical significance (right) of the impact of ENSO on zonal (top) and meridional (below) displacements for each latitudinal band in the West Pacific.

displacement in many latitudinal bins, but the relationship between ENSO and meridional displacements appears weak. In the South Indian, there is a strong impact during El Niño rendering zonal displacements less westerly between approximately 10 and 25°S, whereas the link between ENSO and displacements in the South Pacific appears weaker.

4.3 Track densities

We compute the spatial probability density of tropical cyclone tracks, which we refer to as track densities. Such spatial densities allow us to assess the location and intensity of storms in the event sets. It corresponds to the probability that the center of the TC passes over a grid cell, given that the TC has an intensity greater than a pre-specified minimum at that grid cell. Figure 5 shows the observed and simulated track densities for TCs with near-surface winds of least 18 ms^{-1}. The top row shows the track density for model simulations with post-processing based upon the overall distribution of the LMI, the middle row shows the observed track density from IBTrACS, whereas the bottom row shows the simulated bias (red means the model overestimates track density, blue the opposite). The left and right columns display results for the North Atlantic and West Pacific, respectively.

In all basins, the track densities from the model are similar to the observed track densities, thus showing the capability of the model to simulate a realistic tropical cyclone climatology. In the North Atlantic, the model slightly overestimates track density on the East Coast of the U.S. and slightly underestimates track density in the Gulf of Mexico, Caribbean Sea and along the main development region. Over the West Pacific, the model tends to slightly overestimate track density over the Philippines, Brunei and Indonesia, and slightly underestimate track density over Japan and China. Elsewhere, the model underestimates track density on the West Coast of Mexico, on the East Coast of India and Pakistan, over Australia and Papua New Guinea.

We repeated this exercise for Cat4-5 storms in Figure 6. Given the anomalies are small relative to observations (Figure 6, bottom row), the model slightly underestimates observations over the Caribbean Sea, and overestimates observations along the East Coast of the U.S. and the Northern tip of South America. Over the West Pacific, Southern Japan, Coast of China and Northern Philippines, tracks are slightly underestimated whereas they are overestimated over Southern Philippines, Malaysia (Sarawak) and part of Indonesia. Elsewhere, the model underestimates track density on the West Coast of Mexico and overestimates in Central America, underestimates on the East Coast of India and Pakistan, over Australia and Papua New Guinea.

We end this subsection by analyzing and comparing ENSO anomalies in track densities. Figure 7 (Figure 8) shows plots of simulated and observed anomalies for the North Atlantic (West Pacific) basin. For the North Atlantic, we find a clear opposite signal between the tropics and extra-tropics, which is consistent with Goldenberg and Shapiro (1996), and note symmetrical patterns between La Niña and El Niño (particularly in the simulations). There is a positive (negative) anomaly associated with El Niño (La Niña) events along the East Coast of the U.S., and a positive (negative) anomaly associated with La Niña (El Niño) events along the Gulf of Mexico and the Caribbean seas. Although the simulated patterns mostly match observations during La Niña, the observed El Niño anomaly stretches along the East Coast, which is not the case in the simulations. The shape of the observed El Niño anomaly on the right with a red spot over land however suggests the simulations have an adequate behavior but observations may have been influenced by a few outliers.

The simulated positive anomaly over the Caribbean and negative anomaly in the extratropical North Atlantic during La Niña, and negative anomaly over the Caribbean during El Niño, are generally consistent with Baudouin et al. (2018). However, for the extratropics during El Niño, our positive anomaly is more consistent with the Modoki

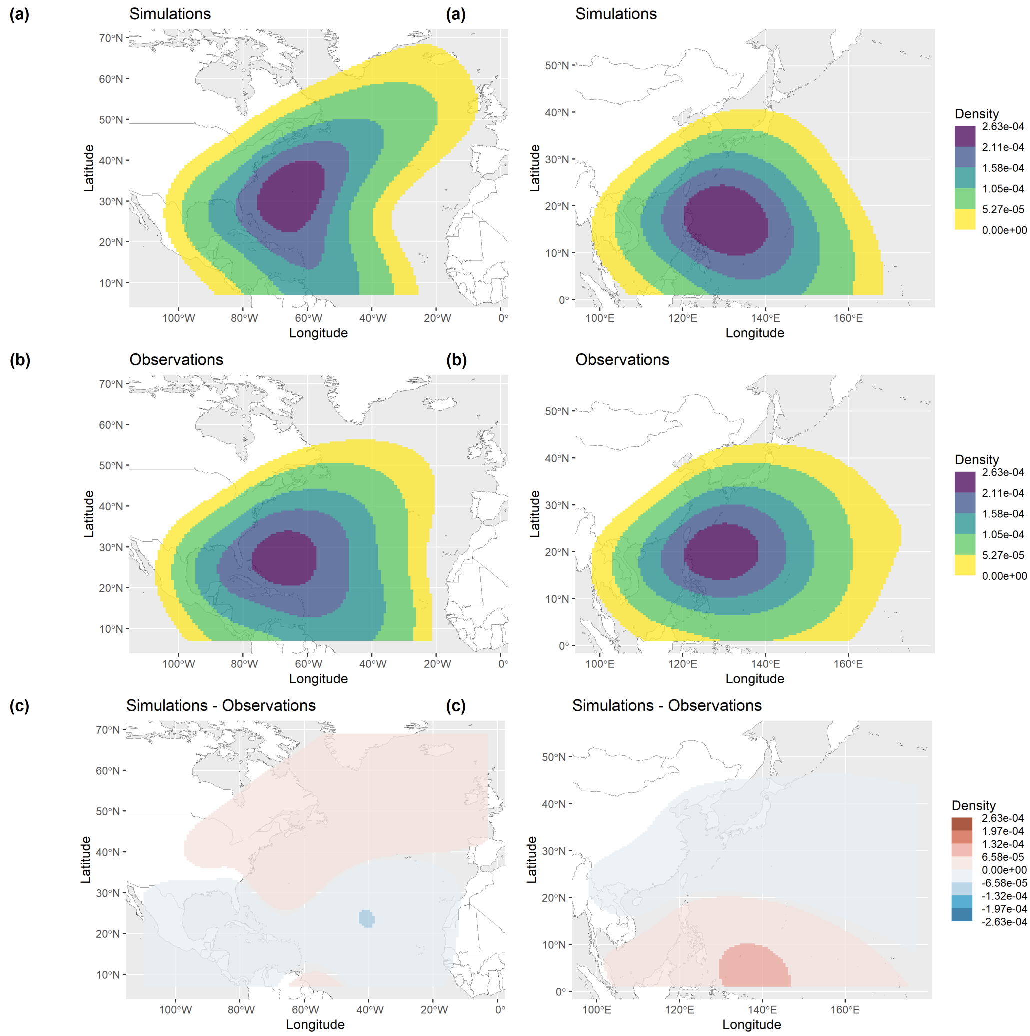

Figure 5: Track probability density over the North Atlantic (left) and West Pacific (right) for storms that reach at least 18 ms^{-1} (Tropical Storms+). Top row (a): simulations from the model; Middle row (b): observations from IBTrACS; Bottom row (c): difference between simulations and observations. The positive and negative limits of the scale for the differences (bottom row) are the same as the maximum limit for the simulations (top row) and observations (middle row). Units are probabilities and add to 1 in the panels in the top two rows.

El Niño (Central Pacific Warming) case from Baudouin et al. (2018). This is reasonable since that study used over two times more tracks from Modoki El Niño years than typical El Niño years.

Over the West Pacific (Figure 8), anomalies highlight an eastward shift during El Niño and westward shift during La Niña. This is well captured by the model. The La Niña signal appears stronger in the observations over South East Asia and the observed anomaly is negative over Japan in both phases. With forty years of data and given the natural variability within each phase, it is likely we observe positive or negative anomalies in both phases in the observations, which is unlikely in the model.

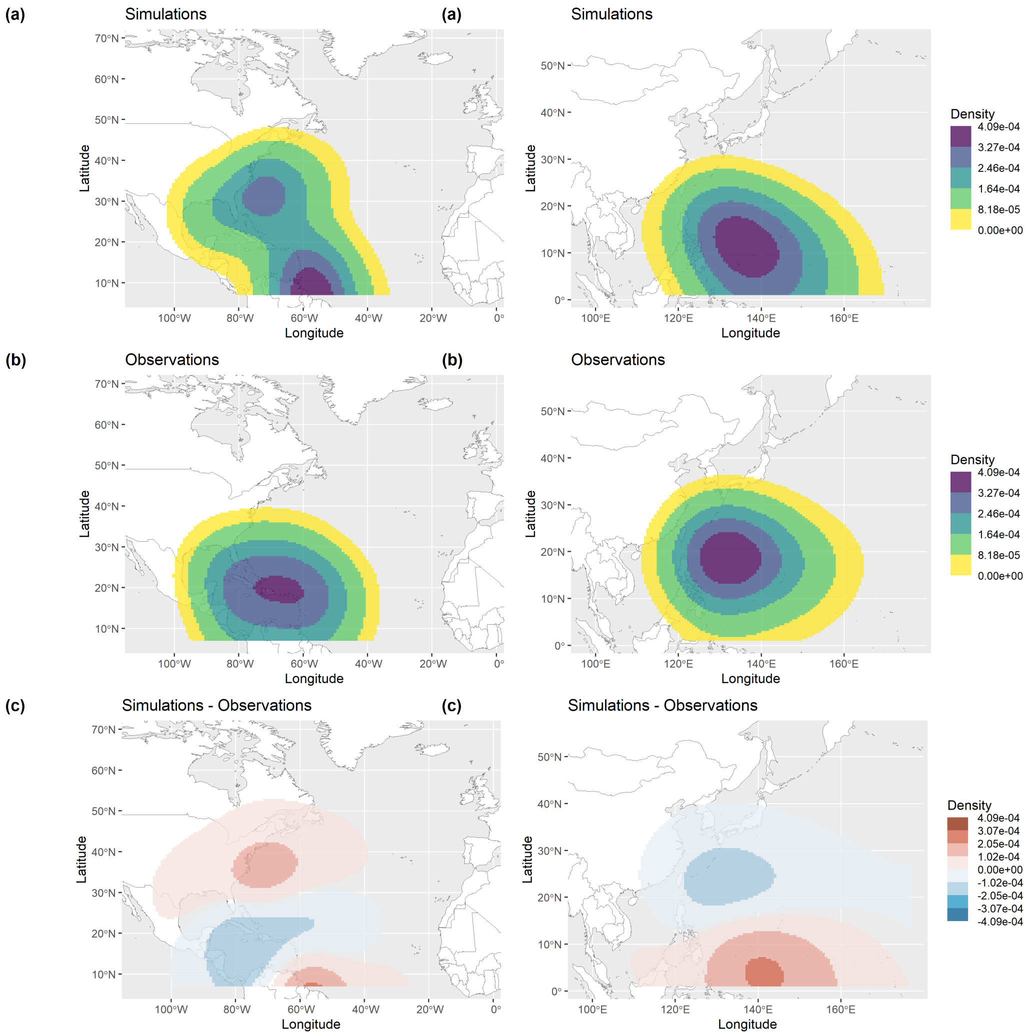

Figure 6: Track probability density over the North Atlantic (left) and West Pacific (right) for storms that reach at least 58 ms^{-1} (Cat4-5). Top row (a): simulations from the model; Middle row (b): observations from IBTrACS; Bottom row (c): difference between simulations and observations. The positive and negative limits of the scale for the differences (bottom row) are the same as the maximum limit for the simulations (top row) and observations (middle row). Units are probabilities and add to 1 in the panels in the top two rows.

Over the other four basins, we also observe approximate symmetrical spatial patterns in the ENSO anomalies. However, we find many areas where observed anomalies are positive (or negative) in both phases that are not replicated in the model: Baja California (Eastern Pacific), Pakistan and parts of India (North Indian), East Coast of Africa (South Indian), North Eastern Australia (South Pacific). The sample of El Niño and La Niña events is relatively small, and so for basins where the ENSO signal is not as dominant, such as the South Indian and East Pacific basins, the signal will be noisy.

Comparing spatial patterns of observed and simulated ENSO anomalies in track densities is a challenging exercise, heavily dependent upon the short observational record and the capacity of the CESM of simulating realistic spatial ENSO patterns. Although not shown, we also analysed the track densities using a post-processing based upon the

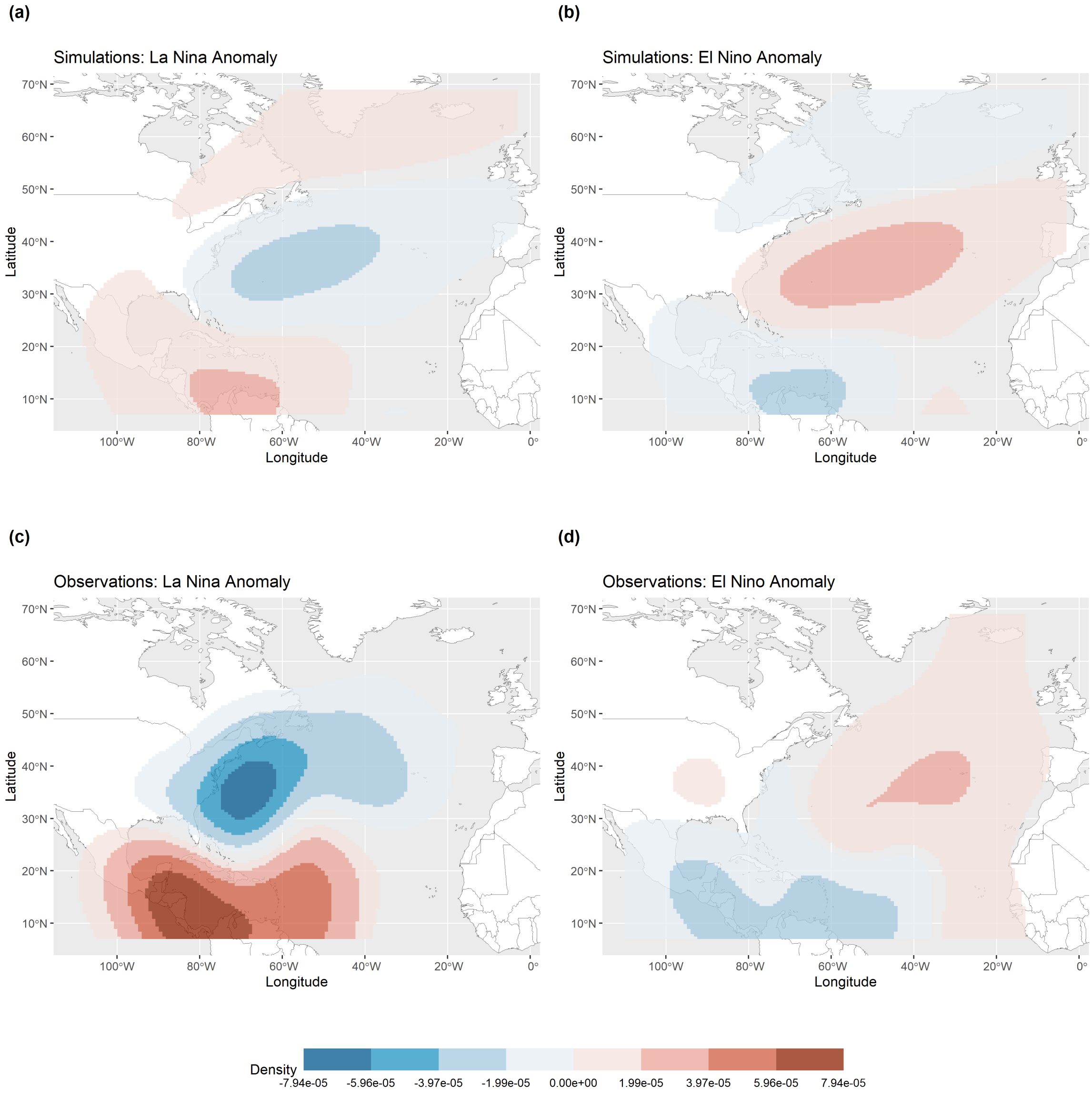

Figure 7: ENSO anomalies in track probability densities for track locations with a minimum speed of 18 ms^{-1} over the North Atlantic.

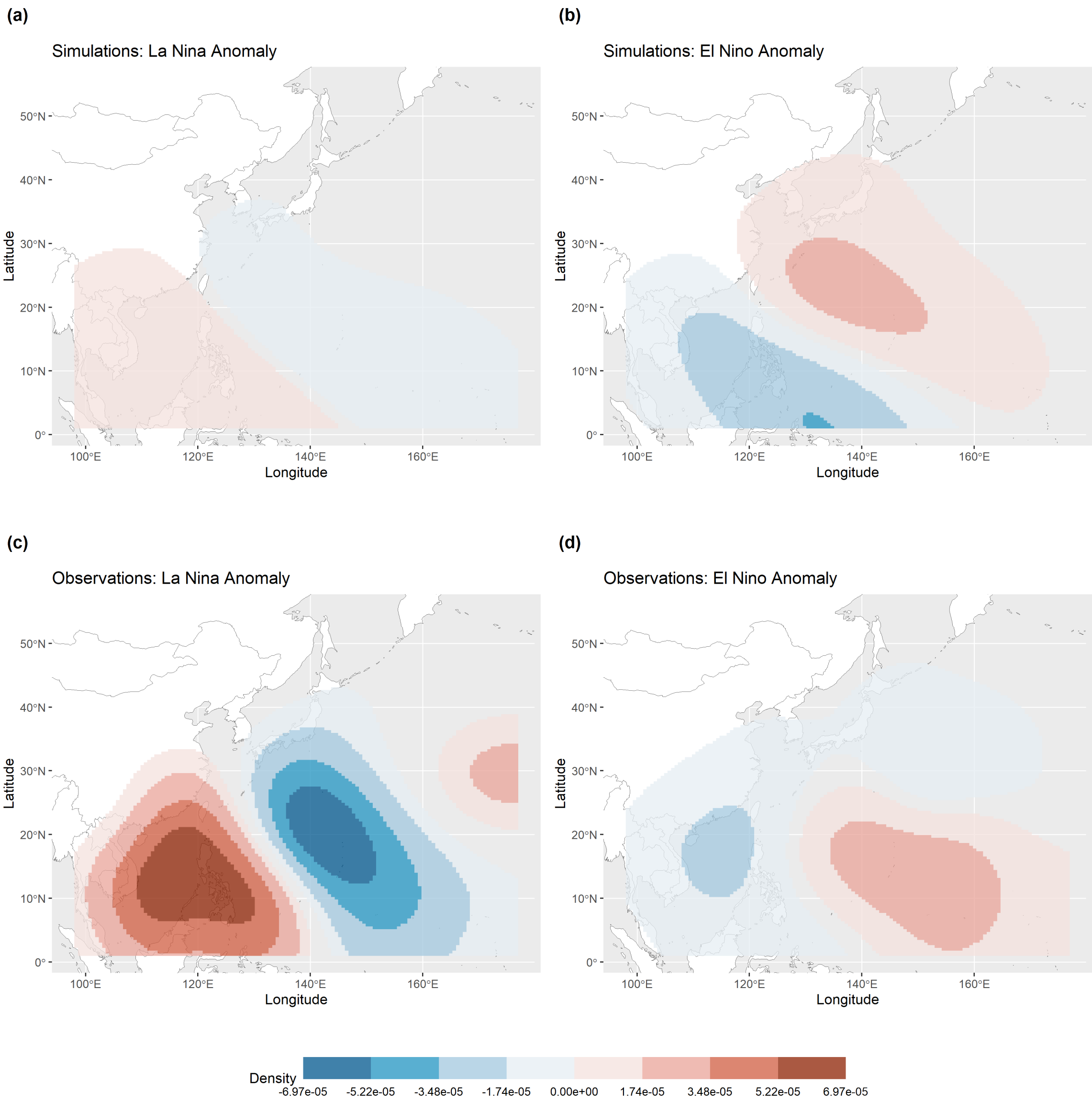

Figure 8: ENSO anomalies in track probability densities for track locations with a minimum speed of 18 ms^{-1} over the West Pacific.

Basin	Intercept	Wind speed	Latitude	sigma
SI	3.9508	-0.0135	-0.0032	0.3739
SP	3.8951	-0.0138	-0.0087	0.3944
WP	3.9155	-0.0118	0.0037	0.4125
NA	3.9358	-0.0154	0.0163	0.5452
EP	3.9731	-0.0133	0.0018	0.4511
NI	4.1406	-0.0148	-0.0077	0.4136

(a) Panel A : Radius of maximum winds

Basin	Intercept	Wind speed	Latitude	RMSE
SI	-1.2014	0.0172	0.0252	8.2167
SP	-1.3312	0.0174	0.0195	8.7479
WP	-1.1821	0.0139	-0.0143	8.7047
NA	-1.1766	0.0161	-0.0221	8.3480
EP	-0.9365	0.0180	-0.0325	8.6994
NI	-1.3083	0.0164	-0.0139	7.8734

(b) Panel B : Dual-exponential profile

Table 2: Parameter estimates of the Willoughby model in each basin. Panel A: RMW regression model. The columns Intercept, Wind speed and Latitude represent the corresponding coefficients in the regression equation whereas sigma is the residual standard deviation. Panel B: Dual-exponential profile. The columns Intercept, Wind speed and Latitude represent the corresponding parameters of the dual-exponential profile and RMSE is the root-mean-square error of the fit.

LMI distribution for each ENSO phase independently. We found that the differences between the post-processing methods are marginal because the simulated tracks remain the same. The post-processing only influences the likelihood of a track of being accepted or rejected (minimum speed of 18 ms^{-1}). In other words, the post-processing method impacts the intensity distribution (as shown in Section 4.5) but not the spatial patterns of ENSO anomalies, which is clearly driven by the CESM.

4.4 Size and radial profile

Following the methodology described in Section 2.5, we calibrated the size and radial profile components of the model. Table 2 - Panel A shows the parameter estimates for the RMW model (Eq. 7a in Willoughby et al. (2006)) and the sigma from the regressions (columns) for each basin (rows). In Panel B we provide the parameters (columns) for Equation 1 and the root mean square error for each basin (rows) .

We find that the "Wind speed" coefficient is negative and statistically significant (p-value below 0.1%) in all basins, meaning that: (1) wind speed is a significant driver of RMW, and that (2) RMW tends to decrease with stronger winds. In the North Atlantic basin, this value is consistent with Willoughby et al. (2006) Eq. 7a (-0.0155 in the latter and -0.0154 in our model). The effect of latitude is negative in the two Southern Hemisphere basins (both strongly statistically significant), and positive in the Northern Hemisphere with the exception of the North Indian (all statistically significant with the exception of the Eastern Pacific). From a physical standpoint, this means that RMW increases when tropical cyclones move away from the Equator (or approach the poles). Again, the values are comparable with Willoughby et al. (2006) Eq. 7a (0.0169 in the latter and 0.0163 in our model). The intercepts are also comparable with Willoughby et al. (2006). The residual standard deviations (sigmas) however indicate a large amount of uncertainty in the predictions. The predicted RMW can hence be multiplied by 1.5-2.5 (1-2 sigmas above or below the mean).

The calibrated wind profiles are presented in Panel B. We cannot easily compare coefficients from our model with Willoughby et al. (2006) Eq. 10c since we forced A to remain in the range $[0, 1]$. However, we see the coefficients for the wind speed are positive for all basins and those for the latitude are negative (positive) in the Northern (Southern) Hemisphere, as expected. The signs obtained in the North Atlantic are coherent with those in Willoughby et al. (2006) Eq. 10c. Moreover, the RMSE is about 8 knots for all basins, which is relatively small considering the radii provided in IBTrACS are for 34, 50, and 60 knots.

4.5 Event sets

Once all 1600 event sets are fully simulated, we have a complete set of tropical cyclone tracks with their corresponding intensity. We now aim to measure the intensity distribution; that is, the proportion of simulated tropical cyclones that reach a given Saffir-Simpson category.

Figure 9 shows the proportion of tropical cyclones that reach each Saffir-Simpson category in IBTrACS and in the simulations, without or with post-processing. The top (bottom) row corresponds to the North Atlantic (West Pacific) basin. The first column corresponds to the empirical frequency in IBTrACS, whereas the second represents the model without any post-processing of the LMI. The third and fourth columns show the simulated relative frequencies with two variants of post-processing based upon the overall basin-scale LMI distribution (3rd column) and by the LMI distribution for each ENSO phase (4th column). Exploring two variants of post-processing allows for the sensitivity of the post-processing technique to be tested and allows for users to be able to choose event sets and catalogs that are tuned to either a general year or a particular ENSO phase.

We observe that the model overestimates tropical storms but underestimates stronger storms in the North Atlantic. Applying either post-processing method significantly improves the overall intensity distribution, especially the correction method based upon the overall distribution of the LMI. In the Western Pacific, the model without post-processing behaves well but the overall post-processing method results in the best fit overall. Elsewhere, the model tends to underestimate Cat4-5 storms, but again, the bias correction based upon the overall LMI distribution does best at replicating observed intensities.

4.6 Annual catalogs

In this last subsection, we analyze the behavior of annual catalogs, which therefore include the frequency component and the resampling step. We have organized the 1 million years of events into 25,000 IBTrACS-like synthetic datasets to study the variability that naturally occurs over 40-year histories.

Each panel of Figure 10 provides an histogram of simulated proportions of storms per category as measured in each of the 25,000 synthetic datasets, whereas the vertical line provides the historical proportion observed in IBTrACS. For example, in the North Atlantic basin, approximately 25% (10%) of historical tropical cyclones have reached maximum intensity of Cat1 (Cat4). However, accounting for the natural variability, the share of Cat1 (Cat4) storms in a 40-year history could have been 13% to 38% (0% to 25%). The location of the vertical lines, derived from the observed 40-year history in IBTrACS falls within the realistic range, which is close to the statistical mode in each category. This is expected given how each component has been calibrated and given the post-processing applied. We obtain similar results in the other five basins.

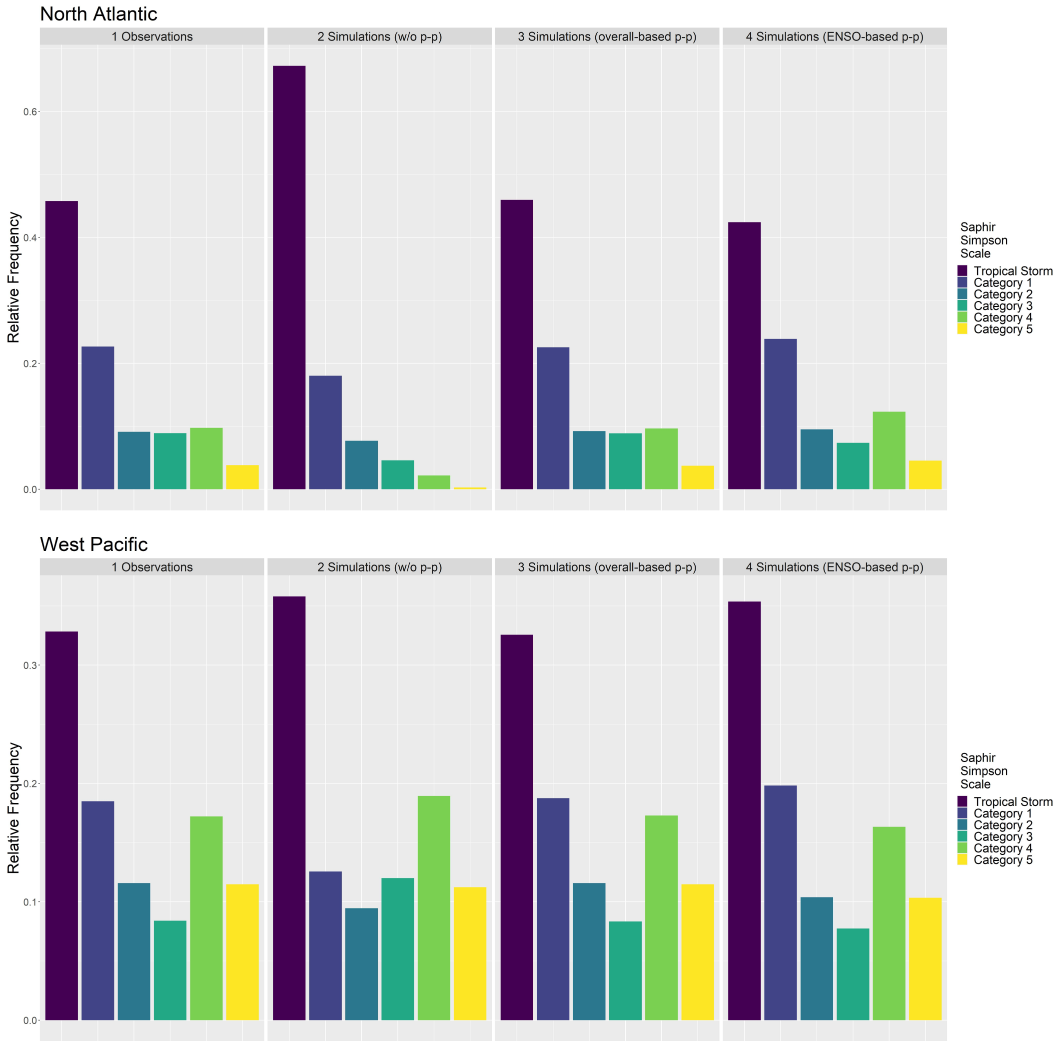

Figure 9: Simulated and observed intensity distribution in the North Atlantic (top) and West Pacific (bottom). Panel 1: Observations. Panel 2: Simulations without post-processing (p-p). Panel 3: Simulations with post-processing based upon overall distribution of LMI. Panel 4: Simulations with post-processing based upon distribution of LMI per ENSO phase.

5 Risk Maps

The annual catalogs can be used to produce landfall risk maps which are extremely useful for socioeconomic studies and financial risk management. In this section, we provide risk maps from simulations for Cat1+ and Cat4-5 tropical cyclones. As in Section 4, the maps shown cover the North Atlantic and West Pacific basins, whereas maps for all basins are provided in the Supporting Information.

For each 2-km grid cell of land, we have computed the average annual hit rate, including direct and indirect hits, from Cat1+ and Cat4-5 tropical cyclones. We have used 1 million years of events to compute return periods, as the inverse of the average annual hit rate. The left (right) panel of Figure 11 shows a risk map for the North Atlantic (West Pacific) basin for Cat1+ tropical cyclones whereas Figure 12 is similar but for Cat4-5

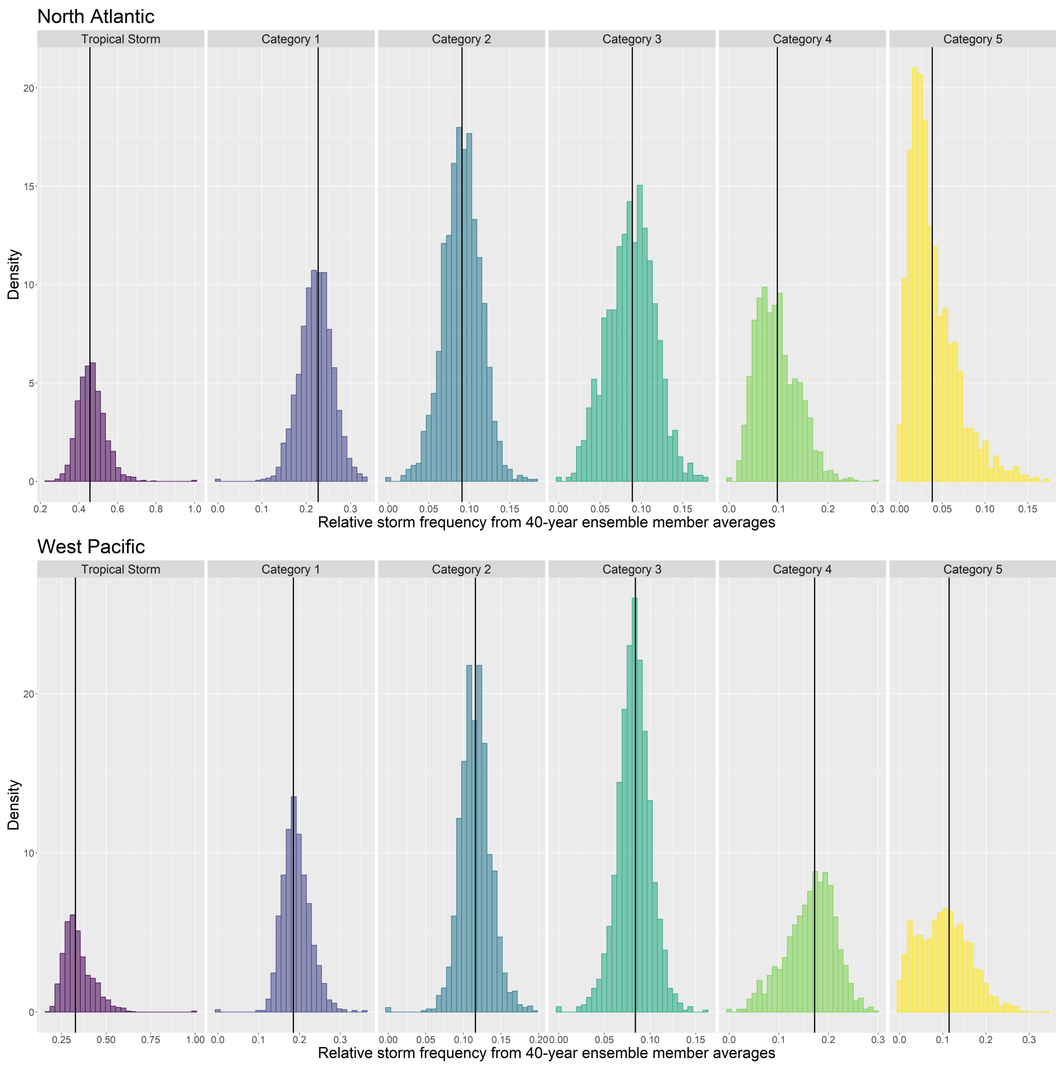

Figure 10: Relative storm frequency over 40-year ensemble members per Saffir-Simpson category (TS to Cat5) in the North Atlantic (top) and West Pacific (bottom). The vertical lines represent the observed proportions for each category (IBTrACS).

tropical cyclones. We compare Cat1+ to results from Bloemendaal et al. (2020) since that study is of comparable resolution and integrated storm size and a model for the radial wind profile.

The left panel of Figure 11 shows that the riskiest locations for landfalling Cat1+ tropical cyclones are expectedly the American and Mexican coasts of the Gulf of Mexico, the Antilles, the U.S. coasts of Virginia and North Carolina. These regions of low return period (high risk) are generally comparable to Bloemendaal et al. (2020), as are the general reduction in risk in the coastal U.S. north of Delaware. However, our rare storms (return periods of 1 in 1000 to 1 in 10000 years) of Cat1+ intensity penetrate further into the coast, and return periods are lower (more risk) in Nova Scotia and Newfoundland than shown in Bloemendaal et al. (2020). The riskiest locations for Cat4-5 hurricanes (Figure 12) in the North Atlantic are the American Coast of the Gulf of Mexico, Florida and the East Coast of the U.S.

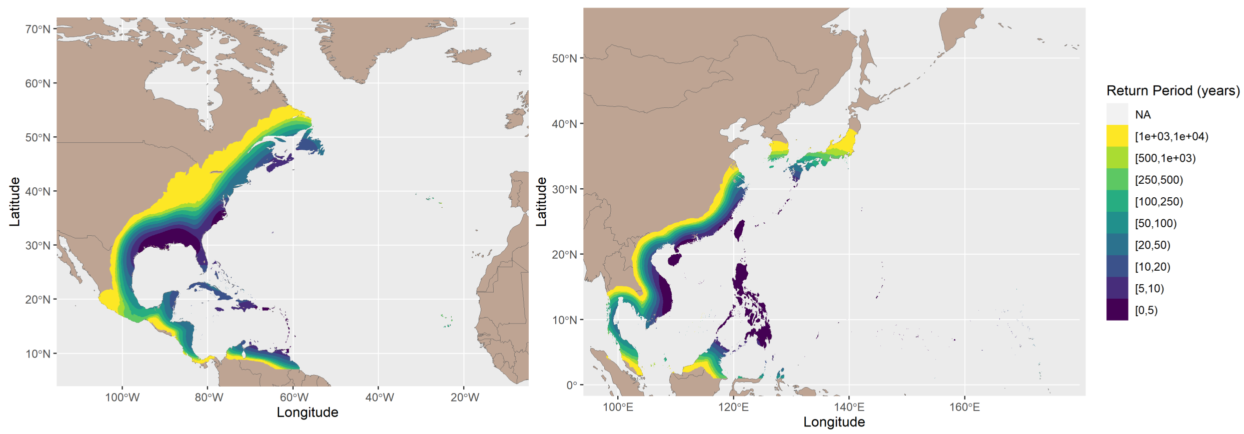

Figure 11: Average annual number of hits (expressed in return period) for Cat1+ storms over the North Atlantic (left) and West Pacific (right)

In the West Pacific, the riskiest locations for Cat1+ typhoons (right panel of Figure 11) are Southern Japan, Taiwan, East Coast of mainland China, Philippines, Vietnam and Cambodia. The high risk regions are generally consistent with Bloemendaal et al. (2020), and we produce a similar footprint of storms' entry into the coast from Vietnam to the Chinese coast to 35°N. Our model results in higher return periods (less risk) in central Japan than Bloemendaal et al. (2020), and Cat1+ storms do not reach Northern Japan, and Northeastern China via the Yellow Sea and Sea of Japan. Though, Cat1+ storms in these areas are rare Cat4-5 typhoons (right panel of Figure 12), show highest risk in the Northeastern Philippines, the Okinawa Japanese prefecture and Taiwan.

6 Discussion and Conclusion

We presented a global modelling framework to randomly generate tropical cyclones (tracks, size and radial profile) based upon the environmental conditions simulated by the CESM Large Ensemble over the present climate. This framework provides a unique and flexible approach for studying risk management of tropical cyclones by generating a large ensemble of TC trajectories that are statistically coherent with observations yet also consistent with interannual climate variability and historical climate change.

The model will be of value to climate and environmental scientists investigating interannual climate variability, event attribution, and downscaling techniques. The hit rates presented and supplemented by impact measures can be of use in socioeconomic and impact research investigating risk mitigation and trends in affected population or financial losses. The modeling framework is also of particular interest to the insurance and reinsurance industry due to its global perspective and direct link to climate models. These two aspects will allow the insurance industry to better constrain the impacts

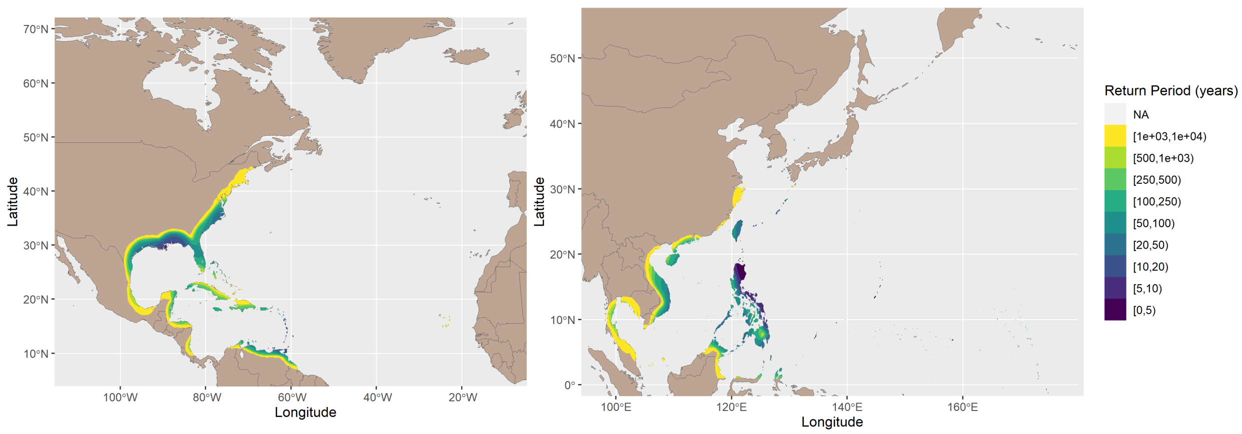

Figure 12: Average annual number of hits (expressed in return period) for Cat4 and above storms over the North Atlantic (left) and West Pacific (right)

of ENSO and other teleconnections on their global portfolios, which can in turn affect pricing, setting of reserves, and the diversification of tropical cyclone risk. The approach presented here also lays the required foundations for physical risk assessments of TC impacts under projected climate scenarios as will soon be required by regulating and accounting bodies globally (Financial Stability Board, 2017; Bank of England, 2019).

The CESM Large Ensemble has proven to be an important tool to expand the short observational record of reliable tropical cyclone measurements. As such, it can improve our understanding of the effects of ENSO on tropical cyclones, and their interactions with the seasonal frequency, cyclogenesis and track locations, wind speeds and radii. By calibrating the model and post-processing the outputs to past observations, it allows a faithful representation of key dynamics of tropical cyclones while leaving enough room to replicate the large spatial and temporal variability inherent to tropical cyclones. By directly connecting the components of tropical cyclones to the CESM Large Ensemble, the modeling framework therefore provides the appropriate foundations to assess the impacts of climate change on each of the tropical cyclone components. We leave such analysis for future research.

Data Availability Statement

The International Best Track Archive for Climate Stewardship (IBTrACS) dataset is available at: `https://www.ncei.noaa.gov/products/international-best-track-archive` (Knapp et al., 2018). The CESM Large Ensemble dataset is available at `https://www.earthsystemgrid.org/` and the authors acknowledge CESM Large Ensemble Community Project and supercomputing resources provided by NSF/CISL/Yellowstone (Kay et al., 2015). The ETOPO1 Global Relief Model was accessed at `https://www.ngdc.noaa.gov/mgg/global/relief/` (Amante & Eakins, 2009; NGDC, 2009).

The Supporting Information is available on Zenodo at `https://doi.org/10.5281/zenodo.7832839` and consists of 1) supporting figures and 2) supporting data (Carozza et al., 2023). The supporting figures are two HTML files that interactively display the figures for all basins. The supporting data contains event sets, catalogs, and an example analysis using the catalogs.

Acknowledgments

This work was supported by Mitacs through the Mitacs Accelerate program. This work was partially funded by AXA XL, the property & casualty and specialty risk division of AXA. We acknowledge the support of the Fonds de recherche du Québec – Nature et technologies (FRQNT), [funding reference number 119908]. Cette recherche a été financée par le Fonds de recherche du Québec – Nature et technologies (FRQNT), [numéro de référence 119908]. We acknowledge the support of the Natural Sciences and Engineering Research Council of Canada (NSERC), [funding reference number PDF-502939-2017]. Cette recherche a été financée par le Conseil de recherches en sciences naturelles et en génie du Canada (CRSNG), [numéro de référence PDF-502939-2017]. This work was also supported by a Marine Environmental Observation, Prediction and Response Network (MEOPAR) Postdoctoral Fellowship Award (PDF-13-2019).

The first two authors contributed equally to this work.

The authors declare that there is no conflict of interest regarding the publication of this article.

The authors would like to thank Tom Philp, Ioana Dima-West and Alec Vessey for their support and feedback in earlier stages of this work.

References

Amante, C., & Eakins, B. (2009). ETOPO1 1 arc-minute global relief model: Procedures, data sources and analysis. *NOAA Technical Memorandum NESDIS NGDC-24. National Geophysical Data Center, NOAA. [January 15, 2021].*. doi: https://doi.org/10.7289/V5C8276M

Aznar-Siguan, G., & Bresch, D. N. (2019). Climada v1: a global weather and climate risk assessment platform. *Geoscientific Model Development*, *12*(7), 3085–3097.

Bank of England. (2019). *The 2021 biennial exploratory scenario on the financial risks from climate change.* Bank of England.

Baudouin, J.-P., Caron, L.-P., & Boudreault, M. (2018, July). Impact of reanalysis boundary conditions on downscaled atlantic hurricane activity. *Climate Dynamics*, *52*(5-6), 3709–3727. Retrieved from `https://doi.org/10.1007/s00382-018-4352-7` doi: 10.1007/s00382-018-4352-7

Bell, R., Hodges, K., Vidale, P. L., Strachan, J., & Roberts, M. (2014, August). Simulation of the global ENSO–tropical cyclone teleconnection by a high-resolution coupled general circulation model. *Journal of Climate*, *27*(17), 6404–6422. Retrieved from `https://doi.org/10.1175/jcli-d-13-00559.1` doi: 10.1175/jcli-d-13-00559.1

Bister, M., & Emanuel, K. (2002). Low frequency variability of tropical cyclone potential intensity 1. interannual to interdecadal variability. *Journal of Geophysical Research*, *107*(D24). Retrieved from `https://doi.org/10.1029/2001jd000776` doi: 10.1029/2001jd000776

Bloemendaal, N., de Moel, H., Muis, S., Haigh, I. D., & C.J.H. Aerts, J. (2020, November 10). Estimation of global tropical cyclone wind speed probabilities using the storm dataset. *Scientific Data*, *7*, 1–11. doi: 10.1038/s41597-020-00720-x

Bloemendaal, N., de Moel, H., Martinez, A. B., Muis, S., Haigh, I. D., van der Wiel, K., . . . others (2022). A globally consistent local-scale assessment of future tropical cyclone risk. *Science advances*, *8*(17), eabm8438.

Bloemendaal, N., Haigh, I. D., de Moel, H., Muis, S., Haarsma, R. J., & Aerts, J. C. J. H. (2020, February). Generation of a global synthetic tropical cyclone hazard dataset using STORM. *Scientific Data*, *7*(1). Retrieved from `https://doi.org/10.1038/s41597-020-0381-2` doi: 10.1038/s41597-020-0381-2

Bove, M. C., O'Brien, J. J., Eisner, J. B., Landsea, C. W., & Niu, X. (1998, November). Effect of el niño on u.s. landfalling hurricanes, revisited. *Bulletin of the American Meteorological Society*, *79*(11), 2477–2482. Retrieved from `https://doi.org/10.1175/1520-0477(1998)079<2477:eoenoo>2.0.co;2` doi: 10.1175/1520-0477(1998)079⟨2477:eoenoo⟩2.0.co;2

Caron, L.-P., Jones, C. G., & Winger, K. (2011). Impact of resolution and downscaling technique in simulating recent atlantic tropical cylone activity. *Climate dynamics*, *37*, 869–892.

Carozza, D. A., Boudreault, M., Grenier, M., & Caron, L.-P. (2023, May). *A global hybrid tropical cyclone risk model based upon statistical and coupled climate models - supporting figures and data.* Zenodo. Retrieved from `https://doi.org/10.5281/zenodo.7832839` doi: 10.5281/zenodo.7832839

Chan, K. T. F., & Chan, J. C. L. (2015). Global climatology of tropical cyclone size as inferred from quikscat data. *International Journal of Climatology*, *35*(15), 4843-4848. Retrieved from `https://rmets.onlinelibrary.wiley.com/doi/abs/10.1002/joc.4307` doi: https://doi.org/10.1002/joc.4307

Chavas, D. R., & Emanuel, K. (2014, April). Equilibrium tropical cyclone size in an idealized state of axisymmetric radiative-convective equilibrium. *Journal of the Atmospheric Sciences*, *71*(5), 1663–1680. Retrieved from `https://doi.org/10.1175/jas-d-13-0155.1` doi: 10.1175/jas-d-13-0155.1

CRED. (2021). *Disaster year in review 2020: Global trends and perspectives* (No. 62). Center for Research on the Epidemiology of Disasters. Retrieved from `https://cred.be/sites/default/files/CredCrunch62.pdf`

Dean, L., Emanuel, K., & Chavas, D. R. (2009, July). On the size distribution of atlantic tropical cyclones. *Geophysical Research Letters*, *36*(14). Retrieved from `https://doi.org/10.1029/2009gl039051` doi: 10.1029/2009gl039051

Demaria, M., & Kaplan, J. (1994, September). Sea surface temperature and the maximum intensity of atlantic tropical cyclones. *Journal of Climate*, *7*(9), 1324–1334. Retrieved from `https://doi.org/10.1175/1520-0442(1994)007<1324:sstatm>2.0.co;2` doi: 10.1175/1520-0442(1994)007⟨1324:sstatm⟩2.0.co;2

Easterling, D. R., Meehl, G. A., Parmesan, C., Changnon, S. A., Karl, T. R., & Mearns, L. O. (2000, September). Climate extremes: Observations, modeling, and impacts. *Science*, *289*(5487), 2068–2074. Retrieved from `https://doi.org/10.1126/science.289.5487.2068` doi: 10.1126/science.289.5487.2068

Emanuel, K. (2011). Global warming effects on u.s. hurricane damage. *Weather, Climate, and Society*, *3*(4), 261 - 268. Retrieved from `https://journals.ametsoc.org/view/journals/wcas/3/4/wcas-d-11-00007_1.xml` doi: https://doi.org/10.1175/WCAS-D-11-00007.1

Emanuel, K. (2013). Downscaling cmip5 climate models shows increased tropical cyclone activity over the 21st century. *Proceedings of the National Academy of Sciences*, *110*(30), 12219–12224.

Emanuel, K. (2015, October). Effect of upper-ocean evolution on projected trends in tropical cyclone activity. *Journal of Climate*, *28*(20), 8165–8170. Retrieved from https://doi.org/10.1175/jcli-d-15-0401.1 doi: 10.1175/jcli-d-15-0401.1

Emanuel, K. (2017, May). A fast intensity simulator for tropical cyclone risk analysis. *Natural Hazards*, *88*(2), 779–796. Retrieved from https://doi.org/10.1007/s11069-017-2890-7 doi: 10.1007/s11069-017-2890-7

Emanuel, K., DesAutels, C., Holloway, C., & Korty, R. (2004, April). Environmental control of tropical cyclone intensity. *Journal of the Atmospheric Sciences*, *61*(7), 843–858. Retrieved from https://doi.org/10.1175/1520-0469(2004)061<0843:ecotci>2.0.co;2 doi: 10.1175/1520-0469(2004)061⟨0843:ecotci⟩2.0.co;2

Emanuel, K., & Jagger, T. (2010, May). On estimating hurricane return periods. *Journal of Applied Meteorology and Climatology*, *49*(5), 837–844. Retrieved from https://doi.org/10.1175/2009jamc2236.1 doi: 10.1175/2009jamc2236.1

Emanuel, K., Ravela, S., Vivant, E., & Risi, C. (2006, March). A statistical deterministic approach to hurricane risk assessment. *Bulletin of the American Meteorological Society*, *87*(3), 299–314. Retrieved from https://doi.org/10.1175/bams-87-3-299 doi: 10.1175/bams-87-3-299

Emanuel, K., Sundararajan, R., & Williams, J. (2008). Hurricanes and global warming: Results from downscaling ipcc ar4 simulations. *Bulletin of the American Meteorological Society*, *89*(3), 347–368.

Emanuel, K., & Zhang, F. (2017, July). The role of inner-core moisture in tropical cyclone predictability and practical forecast skill. *Journal of the Atmospheric Sciences*, *74*(7), 2315–2324. Retrieved from https://doi.org/10.1175/jas-d-17-0008.1 doi: https://doi.org/10.1175/jas-d-17-0008.1

Fiedler, T., Pitman, A. J., Mackenzie, K., Wood, N., Jakob, C., & Perkins-Kirkpatrick, S. E. (2021, February). Business risk and the emergence of climate analytics. *Nature Climate Change*, *11*(2), 87–94. Retrieved from https://doi.org/10.1038/s41558-020-00984-6 doi: 10.1038/s41558-020-00984-6

Financial Stability Board. (2017). *Final report: Recommendations of the task force on climate-related financial disclosures.* Task Force on Climate-related Financial Disclosures.

François, B., Vrac, M., Cannon, A. J., Robin, Y., & Allard, D. (2020). Multivariate bias corrections of climate simulations: which benefits for which losses? *Earth System Dynamics*, *11*(2), 537–562. Retrieved from https://esd.copernicus.org/articles/11/537/2020/ doi: 10.5194/esd-11-537-2020

Goldenberg, S. B., & Shapiro, L. J. (1996). Physical mechanisms for the association of el niño and west african rainfall with atlantic major hurricane activity. *Journal of Climate*, *9*(6), 1169 - 1187. Retrieved from https://journals.ametsoc.org/view/journals/clim/9/6/1520-0442_1996_009_1169_pmftao_2_0_co_2.xml doi: https://doi.org/10.1175/1520-0442(1996)009⟨1169:PMFTAO⟩2.0.CO;2

Holland, G. (2008). A revised hurricane pressure–wind model. *Monthly Weather Review*, *136*(9), 3432–3445.

James, M., & Mason, L. (2005). Synthetic tropical cyclone database. *Journal of waterway, port, coastal, and ocean engineering*, *131*(4), 181–192.

Kalnay, E., Kanamitsu, M., Kistler, R., Collins, W., Deaven, D., Gandin, L., ... Joseph, D. (1996, March). The NCEP/NCAR 40-year reanalysis project. *Bulletin of the American Meteorological Society*, *77*(3), 437–471. Retrieved from https://doi.org/10.1175/1520-0477(1996)077<0437:tnyrp>2.0.co;2 doi: 10.1175/1520-0477(1996)077⟨0437:tnyrp⟩2.0.co;2

Kaplan, J., & DeMaria, M. (1995). A simple empirical model for predicting the decay of tropical cyclone winds after landfall. *Journal of Applied Meteorology and Climatology*, *34*(11), 2499–2512.

Kara, A. B., Rochford, P. A., & Hurlburt, H. E. (2000, July). An optimal definition for ocean mixed layer depth. *Journal of Geophysical Research: Oceans*, *105*(C7), 16803–16821. Retrieved from https://doi.org/10.1029/2000jc900072 doi: 10.1029/2000jc900072

Kay, J. E., Deser, C., Phillips, A., Mai, A., Hannay, C., Strand, G., ... Vertenstein, M. (2015, August). The community earth system model (CESM) large ensemble project: A community resource for studying climate change in the presence of internal climate variability. *Bulletin of the American Meteorological Society*, *96*(8), 1333–1349. Retrieved from https://doi.org/10.1175/bams-d-13-00255.1 doi: 10.1175/bams-d-13-00255.1

Kilroy, G., Smith, R. K., & Montgomery, M. T. (2016, January). Why do model tropical cyclones grow progressively in size and decay in intensity after reaching maturity? *Journal of the Atmospheric Sciences*, *73*(2), 487–503. Retrieved from https://doi.org/10.1175/jas-d-15-0157.1 doi: 10.1175/jas-d-15-0157.1

Knapp, K. R., Diamond, H. J., Kossin, J. P., Kruk, M. C., & Schreck, C. J. (2018). *International best track archive for climate, stewardship (ibtracs) project, version 4. [since 1980, all basins] [accessed june 27, 2021].* *NCEI* https://doi.org/10.25921/82ty-9e16. doi: https://doi.org/10.25921/82ty-9e16

Knapp, K. R., Kruk, M. C., Levinson, D. H., Diamond, H. J., & Neumann, C. J. (2010). The international best track archive for climate stewardship (ibtracs): Unifying tropical cyclone data. *Bulletin of the American Meteorological Society*, *91*(3), 363 - 376. doi: https://doi.org/10.1175/2009BAMS2755.1

Knutson, T., Camargo, S. J., Chan, J. C. L., Emanuel, K., Ho, C.-H., Kossin, J., ... Wu, L. (2020, March). Tropical cyclones and climate change assessment: Part II: Projected response to anthropogenic warming. *Bulletin of the American Meteorological Society*, *101*(3), E303–E322. Retrieved from https://doi.org/10.1175/bams-d-18-0194.1 doi: 10.1175/bams-d-18-0194.1

Kreussler, P., Caron, L.-P., Wild, S., Loosveldt Tomas, S., Chauvin, F., Moine, M.-P., ... others (2021). Tropical cyclone integrated kinetic energy in an ensemble of highresmip simulations. *Geophysical Research Letters*, *48*(5), e2020GL090963.

Lee, C.-Y., Camargo, S. J., Sobel, A. H., & Tippett, M. K. (2020). Statistical–dynamical downscaling projections of tropical cyclone activity in a warming climate: Two diverging genesis scenarios. *Journal of Climate*, *33*(11), 4815–4834.

Lee, C.-Y., Tippett, M. K., Camargo, S. J., & Sobel, A. H. (2015). Probabilistic multiple linear regression modeling for tropical cyclone intensity. *Monthly Weather Review*, *143*(3), 933–954.

Lee, C.-Y., Tippett, M. K., Sobel, A. H., & Camargo, S. J. (2016). Autoregressive modeling for tropical cyclone intensity climatology. *Journal of Climate*, *29*(21), 7815–7830.

Lee, C.-Y., Tippett, M. K., Sobel, A. H., & Camargo, S. J. (2018, January). An environmentally forced tropical cyclone hazard model. *Journal of Advances in Modeling Earth Systems*, *10*(1), 223–241. Retrieved from https://doi.org/10.1002/2017ms001186 doi: 10.1002/2017ms001186

Lin, I.-I., Camargo, S. J., Patricola, C. M., Boucharel, J., Chand, S., Klotzbach, P., ... Jin, F.-F. (2020, October). *ENSO and tropical cyclones.* Wiley. Retrieved from https://doi.org/10.1002/9781119548164.ch17 doi: 10.1002/9781119548164.ch17

Meiler, S., Vogt, T., Bloemendaal, N., Ciullo, A., Lee, C.-Y., Camargo, S., ... Bresch, D. (2022, March). Intercomparison of regional loss estimates from global synthetic tropical cyclone models. Retrieved from https://doi.org/10.21203/rs.3.rs-1429968/v1 doi: 10.21203/rs.3.rs-1429968/v1

Mitchell-Wallace, K., Jones, M., Hillier, J., & Foote, M. (2017). *Natural catastrophe* *risk management and modelling: A practitioner's guide.* John Wiley & Sons.

Moreno-Chamarro, E., Caron, L.-P., Loosveldt Tomas, S., Vegas-Regidor, J., Gutjahr, O., Moine, M.-P., … Vidale, P. L. (2022). Impact of increased resolution on long-standing biases in highresmip-primavera climate models. *Geoscientific Model Development*, *15*(1), 269–289. Retrieved from `https://gmd.copernicus.org/articles/15/269/2022/` doi: 10.5194/gmd-15-269-2022

Nederhoff, K., Hoek, J., Leijnse, T., van Ormondt, M., Caires, S., & Giardino, A. (2021). Simulating synthetic tropical cyclone tracks for statistically reliable wind and pressure estimations. *Natural Hazards and Earth System Sciences*, *21*(3), 861–878. Retrieved from `https://nhess.copernicus.org/articles/21/861/2021/` doi: 10.5194/nhess-21-861-2021

NGDC. (2009). *ETOPO1 1 arc-minute global relief model. [Accessed January 15, 2021]. NCEI* `https://doi.org/10.7289/V5C8276M`.

Roberts, M. J., Camp, J., Seddon, J., Vidale, P. L., Hodges, K., Vannière, B., … Wu, L. (2020, July). Projected future changes in tropical cyclones using the CMIP6 HighResMIP multimodel ensemble. *Geophysical Research Letters*, *47*(14). Retrieved from `https://doi.org/10.1029/2020gl088662` doi: 10.1029/2020gl088662

Schade, L. R., & Emanuel, K. (1999, February). The ocean's effect on the intensity of tropical cyclones: Results from a simple coupled atmosphere–ocean model. *Journal of the Atmospheric Sciences*, *56*(4), 642–651. Retrieved from `https://doi.org/10.1175/1520-0469(1999)056<0642:toseot>2.0.co;2` doi: https://doi.org/10.1175/1520-0469(1999)056⟨0642:toseot⟩2.0.co;2

Seneviratne, S., Zhang, X., Adnan, M., Badi, W., Dereczynski, C., Luca, A. D., … Zhou, B. (2021). Weather and climate extreme events in a changing climate. *Climate Change 2021: The Physical Science Basis*, 1513–1766. Retrieved from `https://www.ipcc.ch/report/ar6/wg1/downloads/report/IPCC_AR6_WGI_Chapter11.pdf` doi: 10.1017/9781009157896.013

Strachan, J., Vidale, P. L., Hodges, K., Roberts, M., & Demory, M.-E. (2013). Investigating global tropical cyclone activity with a hierarchy of agcms: The role of model resolution. *Journal of Climate*, *26*(1), 133–152.

UNDRR, C. (2020). *Human cost of disasters: An overview of the last 20 years 2000-2019.* United Nations Office for Disaster Risk Reduction. Retrieved from `https://www.undrr.org/media/48008/download`

UNEP. (2019). *Insuring the climate transition: Enhancing the insurance industry's assessment of climate change futures.* United Nations Environment Programme. Retrieved from `https://www.unepfi.org/psi/wp-content/uploads/2021/01/PSI-TCFD-final-report.pdf`

Vickery, P. J., Skerlj, P. F., & Twisdale, L. A. (2000, October). Simulation of hurricane risk in the u.s. using empirical track model. *Journal of Structural Engineering*, *126*(10), 1222–1237. Retrieved from `https://doi.org/10.1061/(asce)0733-9445(2000)126:10(1222)` doi: 10.1061/(asce)0733-9445(2000)126:10(1222)

Wagner, R. G. (1996, July). Decadal-scale trends in mechanisms controlling meridional sea surface temperature gradients in the tropical atlantic. *Journal of Geophysical Research: Oceans*, *101*(C7), 16683–16694. Retrieved from `https://doi.org/10.1029/96jc01214` doi: 10.1029/96jc01214

Warszawski, L., Frieler, K., Huber, V., Piontek, F., Serdeczny, O., & Schewe, J. (2013, December). The inter-sectoral impact model intercomparison project (ISI–MIP): Project framework. *Proceedings of the National Academy of Sciences*, *111*(9), 3228–3232. Retrieved from `https://doi.org/10.1073/pnas.1312330110` doi: 10.1073/pnas.1312330110

Willoughby, H. E., Darling, R. W. R., & Rahn, M. E. (2006). Parametric representation of the primary hurricane vortex. part ii: A new family of sectionally continuous profiles. *Monthly Weather Review*, *134*(4), 1102 - 1120. Retrieved from https://journals.ametsoc.org/view/journals/mwre/134/4/mwr3106.1.xml doi: https://doi.org/10.1175/MWR3106.1